Note: A very simple circuit for piezo actuator pseudo-tracking for continuous-wave cavity ring-down spectroscopy

T. Földes[a)]
Laboratoire de Chimie quantique et Photophysique, Université libre de Bruxelles, Bruxelles, Belgium

(Received 13 November 2012; accepted 16 December 2012; published online 7 January 2013)

A very simple circuit for pseudo-tracking of the piezo actuator for continuous-wave cavity ring-down spectroscopy (cw-CRDS) is presented. The circuit is based on an ordinary positive-edge trigger D-type flip flop integrated circuit, has a low parts count, and can be easily assembled using only off the shelf components. The circuit can be straightforwardly incorporated into most cw-CRDS setups and, thanks to the increased ring-down event rate, higher sensitivity or lower data acquisition time can be achieved. © *2013 American Institute of Physics*. [http://dx.doi.org/10.1063/1.4774044]

Cavity ring-down spectroscopy (CRDS) is a highly sensitive direct absorption spectroscopic technique developed by O'Keefe and Deacon[1] in 1988 and later advanced by Romanini[2] (permitting the use of diode lasers). In this technique, the sensitivity gains are achieved by trapping a laser pulse in a high finesse optical cavity containing the sample of interest. The light intensity exiting the cavity is recorded and from the time necessary for the intensity to decrease to 1/e of the initial value, the absorption coefficient α is directly derived. Because of its simplicity, ability to measure the absorption on an absolute scale, high sensitivity, and independence from power fluctuations of the laser (because of the analysis of time characteristics of the signal, rather than amplitude), as well as its speed and compatibility with small sample volumes, this technique is widely used for various applications, including breath diagnostics,[3] explosives detection,[4] food industry applications,[5] and atmospheric field measurements.[6]

In the most common and practically most sensitive arrangement,[7] a tunable narrow bandwidth continuous wave laser is used. One of the cavity mirrors is mounted on a piezoelectric element (PZT). By applying a triangular voltage ramp to the PZT, the cavity length is modulated by more than $\sim\lambda/2$ (where λ is the wavelength of the laser). This ensures that resonance events can regularly occur (see Figure 1) at any set wavelength of the laser. When resonance is achieved, a rapid increase of the light intensity exiting the cavity can be detected. A threshold circuit is used to detect this intensity rise and using an optical switch, the incoming laser beam is deflected/turned off for a set period (laser off) and a ring-down decay can be observed.

As an optical switch, usually an acousto-optic modulator (AOM) is used.[7–9] The first order diffracted beam is injected into the optical cavity and by turning off the AOM, the diffraction is rapidly extinguished. The AOM hence acts as a fast optical switch with a large on/off contrast and reasonably short response time.[9] Alternative approaches include direct electronic switching of the laser,[10] rapidly sweeping the cavity or the wavelength of the laser out of resonance,[11] or using an electronically switched semiconductor optical amplifier.[12] When sweeping the cavity length with a periodic triangular voltage ramp slightly more than $\sim\lambda/2$, one expects resonances to occur (for a set wavelength of the laser) at the same PZT voltage in a mechanically perfectly stable cavity and at twice the cavity length sweep rate. In practice, resonances occur at a different rate, since some resonance events may not produce sufficient intensity to be detected by the threshold circuit or every second resonance event might not occur close to the cavity sweep turning point (a ring-down event should occur during the laser off period). Increasing the ring-down rate by increasing the sweep rate is limited by the compromise between the sweep rate and intracavity power buildup with particularities depending on the laser linewidth (on the time scale of the cavity buildup), cavity length, and the ring-down time (for details see Refs. 13 and 14). Usually, sweep rates up to few hundred hertz are used. To increase the ring-down rate, cavity resonance tracking can be effectively used. In this approach, the cavity length is swept less than $\sim\lambda/2$ around the region where resonance occurs, allowing to increase the frequency of passages through resonance while keeping constant the duration of passages through resonance. This can be achieved by different methods. Romanini *et al.*[15] used an analogue tracking circuit based on a phase-locked-loop (PLL), which detects the phase shift between the dither signal and the resonance. The same method was later used in Ref. 16. In Ref. 17, a software based tracking algorithm was used. In Ref. 18, a microcontroller based tracking unit is described. The disadvantage of these techniques is that they require considerable hardware resources, in the case of the software algorithm at least a spare analog-to-digital converter (ADC) and digital-to-analog converter (DAC) channel. The additional disadvantage of the PLL approach is the relatively long time necessary for re-locking (typically 1 s[15]).

The presented tracking circuit (Figure 2) is based on an ordinary positive-edge trigger D-type flip-flop integrated circuit (e.g., 74HC74), has a low parts count, and can be easily assembled using the most common off the shelf components. It is a simple and robust alternative to the existing tracking techniques.

The scheme is based on simply changing the ramp direction after a set period after a resonance event occurs (Figure 3). The tracking circuit generates the ramp signal by integrating the output signal of the flip-flop integrated circuit

a)Electronic mail: tfoldes@ulb.ac.be.

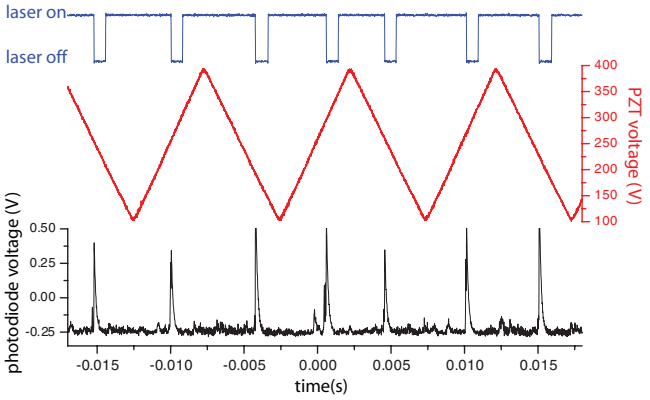

FIG. 1. An oscilloscope single-shot acquisition showing the photodiode signal, voltage applied to the PZT used to sweep the cavity length and the laser on/off logical signal in the most common cw-CRDS configuration (without tracking).

(IC). The flip-flop IC changes states at the positive edge of the input signal, and can be fed (in the simplest configuration) directly by the ordinary logical signal generated for the optical switch. Also, if the voltage ramp reaches a pre-set highest or lowest voltage, a comparator generates a set or reset signal on the flip-flop IC to change the direction of the ramp. This ensures that the circuit will generate a periodic triangular voltage ramp if there is no input signal from the threshold circuit. The slope of the ramp can be set by the RC constant of the integrator and can be adjusted with a potentiometer added in series with the input resistor (R in Figure 2).

Higher performance of the system can be achieved by generating a derived "ramp direction change" logical signal from the signal for the optical switch, so that the ramp direction changes at an arbitrarily settable period after resonance events occur (usually shorter than the laser off period, see Figure 4). This signal can be easily generated using, for example, a retriggerable monostable multivibrator (e.g., 74LS123) in the basic datasheet circuit connection with a remote trimmer to set the pulse width. This allows tuning the tracking circuit with respect to the actual mechanical stability of the resonator by simply maximizing the number of ring-down events.

In this work, the tracking circuit was incorporated into the so-called *Fantasio+* setup, described in detail in

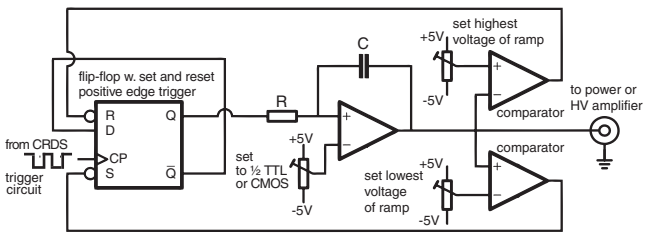

FIG. 2. Scheme of the tracking circuit. The voltage ramp is produced by integrating the output of the flip-flop IC. A change in the direction of the ramp is triggered by the rising-edge of the input signal and by the comparators defining the lowest and highest voltage of the ramp. The input signal can be directly the logical signal for triggering the optical switch. *D* stands for data, *CP* for clock, *S* for set, and *R* for reset inputs of the flip-flop IC, with *Q* and $\bar{Q}$ being its complementary outputs. HV stands for high voltage.

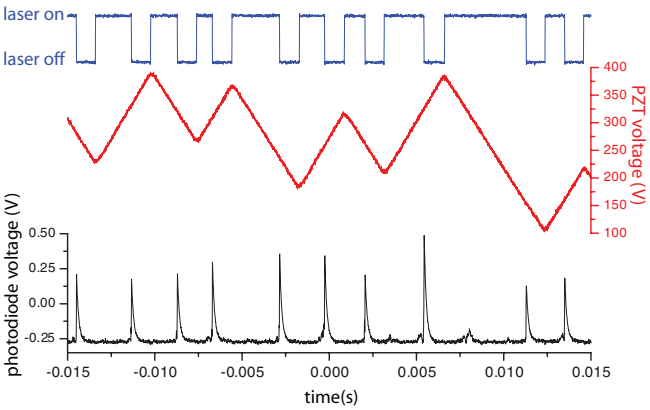

FIG. 3. An oscilloscope single-shot acquisition showing the performance of the tracking circuit incorporated into a cw-CRDS setup in the simplest configuration: the logical signal generated for the optical switch is directly used to trigger the flip-flop IC, hence changing the direction of the ramp after every laser off period.

Ref. 19. In this setup, a continuous-wave cavity ring-down spectroscopy (cw-CRDS) was coupled to a supersonic expansion and the mechanical stability of the ring-down cavity was compromised both by mechanical noise of the pumping system of the supersonic expansion (two large turbomolecular pumps backed by an Alcatel ADS 860 HII group) and by the non-monolithic arrangement of the cavity ring-down cell (the mirror holders were inserted into two stainless steel tubes welded perpendicularly to a large cylindrical expansion cell, forming a 54 cm long cavity). Previously, the PZT had been driven by an audio amplifier IC coupled to a step-up transformer allowing only very limited adjustment. In the presented configuration, the tracking circuit was connected to a low cost original equipment manufacturer (OEM) high voltage amplifier (Viking Industrial Products VP7206-48H805). By adjusting the reference voltages of the 2 comparators in the tracking circuit the highest and lowest voltage and by adjusting the RC constant of the integrator, the frequency of the triangular ramp (slope of the waveform) could be conveniently tuned. The pulse width of the "ramp direction change" sig-

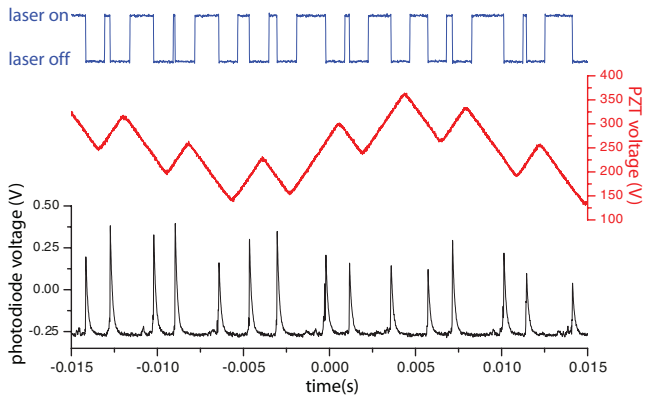

FIG. 4. An oscilloscope single-shot acquisition showing the performance of the tracking circuit with the "ramp direction change" triggering signal derived from the logical signal generated for the optical switch. It was set so that the rising edge of this signal occurred approximately in the middle of the laser off period and could be adjusted to achieve the highest repetition rate with the given stability of the ring-down cavity.

nal derived from the logical signal of the optical switch was adjusted to achieve the highest number of ring-down events per second while the gas injection and pumping was fully running. Using this approach, we generally could achieve a better than 50% increase in the ring-down rate, up to 700 ring-down events per second with the tracking on, as compared to 400 events with the tracking off. We used a 16 bit, 1.5 MHz analog-to-digital converter to sample the ring-down decays and employed a weighted least squares fit of an exponential decay with the offset level as a free parameter. Despite the findings in Ref. 20, we did not observe decreasing noise when increasing the sampling (and laser off) period above 1 ms with an average ring-down time of 130 μs. This 1 ms laser off period limited the maximum ring-down event rate to a theoretical 1 kHz. We were generally able to achieve noise equivalent absorption (NEA) on the order of $\alpha_{\min} \approx 5 \times 10^{-10}$ $\mathrm{cm}^{-1}/\mathrm{Hz}^{1/2}$.

In contrast to previously published tracking schemes for cw-CRDS, the presented circuit can be easily constructed even on a stripboard. Its performance can be readily optimized with regard to the actual mechanical stability of the cavity by simply maximizing the number of ring-down events by changing the pulse width of the "ramp direction change" triggering signal. The circuit generates a periodic triangular voltage ramp when the laser off logical signal is disconnected so that the cavity can be aligned in the conventional manner. The circuit can be straightforwardly incorporated into most cw-CRDS setups, by simply replacing a function generator and thanks to the increased ring-down event rate, higher sensitivity or lower data acquisition time can be achieved.

I thank for the idea of using a flip-flop integrated circuit instead of a microcontroller my brother, Pali (‡). I thank B. Denègre for the PCB work. I thank for assistance the team around the Fantasio setup: M. Herman, K. Didriche, C. Lauzin and acknowledge the work of P. Macko, who originally put together the CRDS around the Fantasio setup. Financial support from the Belgian Federal Science Policy Office (Contract No. SD/CS/07A, Advanced Exploitation of Ground-Based Measurements for Atmospheric Chemistry and Climate applications–II) is gratefully acknowledged.

[1] A. O'Keefe and D. A. G. Deacon, Rev. Sci. Instrum. **59**, 2544 (1988).
[2] D. Romanini, A. A. Kachanov, N. Sadeghi, and F. Stoeckel, Chem. Phys. Lett. **264**, 316 (1997).
[3] M. Mürtz, Opt. Photonics News **16**, 30 (2005).
[4] M. W. Todd, R. A. Provencal, T. G. Owano, B. A. Paldus, A. Kachanov, K. L. Vodopyanov, M. Hunter, S. L. Coy, J. I. Steinfeld, and J. T. Arnold, App. Phys. B **75**, 367 (2002).
[5] E. Wahl, S. Tan, S. Koulikov, B. Kharlamov, C. Rella, E. Crosson, D. Biswell, and B. Paldus, Opt. Express **14**, 1673 (2006).
[6] K. von Bobrutzki, C. F. Braban, D. Famulari, S. K. Jones, T. Blackall, T. E. L. Smith, M. Blom, H. Coe, M. Gallagher, M. Ghalaieny, M. R. McGillen, and C. J. Percival, Atmos. Meas. Tech. Discuss. **2**, 1783 (2009).
[7] S. Kassi, A. Campargue, K. Pachucki, and J. Komasa, J. Chem. Phys. **136**, 184309 (2012).
[8] T. Földes, P. Čermák, M. Macko, P. Veis, and P. Macko, Chem. Phys. Lett. **467**, 233 (2009).
[9] K. Didriche, T. Földes, C. Lauzin, D. Golebiowski, J. Liévin, and M. Herman, "Experimental 2CH excitation in acetylene-containing van der Waals complexes," Mol. Phys. **110**, 2781 (2012).
[10] T. Földes, P. Čermák, J. Rakovský, M. Macko, J. Krištof, P. Veis, and P. Macko, Electron. Lett. **46**(7), 523 (2010).
[11] B. J. Orr and Y. He, Chem. Phys. Lett. **512**, 1 (2011).
[12] Y. Tang, S. L. Yang, and K. K. Lehmann, Rev. Sci. Instrum. **83**, 043115 (2012).
[13] J. Morville, D. Romanini, M. Chenevier, and A. Kachanov, App. Opt. **41**, 6980 (2002).
[14] J. Morville, D. Romanini, A. A. Kachanov, and M. Chenevier, App. Phys. B **78**, 465 (2004).
[15] D. Romanini, A. A. Kachanov, and F. Stoeckel, Chem. Phys. Lett. **270**, 538 (1997).
[16] P. Macko, G. Báno, P. Hlavenka, R. Plasil, V. Poterya, A. Pysanenko, O. Votava, R. Johnsen, and J. Glosík, Int. J. Mass. Spectrom. **233**, 299 (2004).
[17] J. W. Hahn, Y. S. Yoo, J. Y. Lee, J. W. Kim, and H.-W. Lee, Appl. Opt. **38**, 1859 (1999).
[18] O. Votava, M. Mašát, A. E. Parker, C. Jain, and C. Fittschen, Rev. Sci. Instrum. **83**, 043110 (2012).
[19] K. Didriche, C. Lauzin, T. Földes, X. de Ghellinck D'Elseghem Vaernewijck, and M. Herman, Mol. Phys. **108**, 2155 (2010).
[20] K. K. Lehmann, G. Berden, and R. Engeln, "An introduction to cavity ring-down spectroscopy," in *Cavity Ring-Down Spectroscopy: Techniques and Applications*, edited by G. Berden and R. Engeln (Wiley, Chichester, 2010).

Journal of Quantitative Spectroscopy & Radiative Transfer 160 (2015) 36–49

Contents lists available at ScienceDirect

Journal of Quantitative Spectroscopy & Radiative Transfer

journal homepage: www.elsevier.com/locate/jqsrt

Retrieval of ethane from ground-based FTIR solar spectra using improved spectroscopy: Recent burden increase above Jungfraujoch

B. Franco [a,*], W. Bader [a], G.C. Toon [b], C. Bray [c], A. Perrin [d], E.V. Fischer [e], K. Sudo [f,g], C.D. Boone [h], B. Bovy [a], B. Lejeune [a], C. Servais [a], E. Mahieu [a]

[a] Institute of Astrophysics and Geophysics, University of Liège, B-4000 Liège (Sart-Tilman), Belgium
[b] Jet Propulsion Laboratory, California Institute of Technology, Pasadena, CA 91109, USA
[c] CEA, DEN, DPC, F-91191 Gif-sur-Yvette, France
[d] Laboratoire Interuniversitaire des Systèmes Atmosphériques (LISA-UMR7583) CNRS, Universités Paris Est Créteil and Paris 7 Diderot (IPSL), F-94010 Créteil cedex, France
[e] Department of Atmospheric Science, Colorado State University, Fort Collins, CO, USA
[f] Graduate School of Environmental Studies, Nagoya University, Nagoya, Japan
[g] Department of Environmental Geochemical Cycle Research, Japan Agency for Marine-Earth Science and Technology, Yokohama, Japan
[h] Department of Chemistry, University of Waterloo, Ontario, Canada

ARTICLE INFO

Article history:
Received 11 December 2014
Received in revised form
12 March 2015
Accepted 13 March 2015
Available online 20 March 2015

Keywords:
Ethane
FTIR
Jungfraujoch
Pseudo-lines
Trend
Shale gas

ABSTRACT

An improved spectroscopy is used to implement and optimize the retrieval strategy of ethane (C_2H_6) from ground-based Fourier Transform Infrared (FTIR) solar spectra recorded at the high-altitude station of Jungfraujoch (Swiss Alps, 46.5°N, 8.0°E, 3580 m a.s.l.). The improved spectroscopic parameters include C_2H_6 pseudo-lines in the 2720–3100 cm^{-1} range and updated line parameters for methyl chloride and ozone. These improved spectroscopic parameters allow for substantial reduction of the fitting residuals as well as enhanced information content. They also contribute to limiting oscillations responsible for ungeophysical negative mixing ratio profiles. This strategy has been successfully applied to the Jungfraujoch solar spectra available from 1994 onwards. The resulting time series is compared with C_2H_6 total columns simulated by the state-of-the-art chemical transport model GEOS-Chem. Despite very consistent seasonal cycles between both data sets, a negative systematic bias relative to the FTIR observations suggests that C_2H_6 emissions are underestimated in the current inventories implemented in GEOS-Chem. Finally, C_2H_6 trends are derived from the FTIR time series, revealing a statistically-significant sharp increase of the C_2H_6 burden in the remote atmosphere above Jungfraujoch since 2009. Evaluating cause of this change in the C_2H_6 burden, which may be related to the recent massive growth of shale gas exploitation in North America, is of primary importance for atmospheric composition and air quality in the Northern Hemisphere.

1. Introduction

Ethane (C_2H_6) is the most abundant non-methane hydrocarbon in the Earth's atmosphere with a lifetime of approximately 2 months [1]. On a global scale, the main

* Corresponding author. Tel.: +32 4 366 97 85.
E-mail address: bruno.franco@ulg.ac.be (B. Franco).

http://dx.doi.org/10.1016/j.jqsrt.2015.03.017
0022-4073/

sources of C_2H_6 are leakage from the production, transport of natural gas loss (62%), biofuel consumption (20%) and biomass burning (18%), mainly located in the Northern Hemisphere [1–3]. Biogenic and oceanic sources are generally very small [1]. The main sink of C_2H_6 in the troposphere is oxidation via reaction with hydroxyl radicals (OH), while in the stratosphere reaction with chlorine atoms dominates [4].

Ethane has a large impact on tropospheric composition and impacts the distribution of ozone (O_3) through several pathways, making it a compound of great interest as a sensitive indicator of tropospheric pollution and transport [5]. By acting as a major sink for tropospheric OH, the abundance of C_2H_6 impacts the lifetime of methane (CH_4). Thus C_2H_6 is an indirect greenhouse gas with a net global warming potential of 5.5 (100-year horizon; [6]). Similarly, C_2H_6 influences the atmospheric content of carbon monoxide (CO; [4]). Ethane also has a significant impact on air quality as it is an important source of peroxyacetyl nitrate (PAN), a thermally unstable reservoir for nitrogen oxide radicals (NO_x; [1,7]). By providing the main NO_x source in many regions of the atmosphere, PAN has a major effect on the production and loss of O_3.

Atmospheric C_2H_6 abundances can be measured using various techniques. Previous measurements of C_2H_6 include Fourier Transform InfraRed (FTIR) spectrometer observations by the balloon-borne Jet Propulsion Laboratory MkIV Interferometer [8], aircraft air samples collected during the NASA's Global Tropospheric Experiment Field Missions Pacific Exploratory Mission (e.g., PEM-West A; [9] and TRACE-A; [10,11]), solar occultations recorded by the Atmospheric Chemistry Experiment – Fourier Transform Spectrometer (ACE-FTS; [12]), ground-based measurements by gas chromatograph (e.g., [13–15]) and finally limb-scans performed by the Michelson Interferometer for Passive Atmospheric Sounding (MIPAS) onboard the European ENVIronmental SATellite (ENVISAT; [16]). Analysis of these data records has significantly increased our understanding of the long range transport of C_2H_6.

Ethane has also been measured by ground-based FTIR technique at several latitudes in both hemispheres, covering different time periods (e.g., [5,17–25]). Nevertheless, strong latitudinal, seasonal and local fluctuations on small spatial and temporal scales make C_2H_6 secular trend determination difficult from the existing observations. Indeed, its concentration in the atmosphere is largely influenced by strong vertical mixing and dilution with background air during transport from emission sources.

In this paper, we present a 20-year long-term time series of C_2H_6 derived from ground-based high-resolution infrared solar spectra recorded with a Bruker 120HR FTIR spectrometer operated under clear sky conditions at the high-altitude International Scientific Station of the Jungfraujoch (referred to below as ISSJ; Swiss Alps, 46.5°N, 8.0°E, 3580 m a.s.l.; [26]). Such a long-term time series in the remote atmosphere allows for air quality monitoring and provides a valuable tool for model and satellite validation. The solar spectra used here have been recorded within the framework of the Network for Detection of Atmospheric Composition Change monitoring activities (NDACC; see http://www.ndacc.org).

This work furthers the C_2H_6 dataset previously published in [19] and [27] for the ISSJ station and it presents an improved retrieval strategy in terms of reduced residuals and enhanced information content, combining three spectral domains for the first time at ISSJ. A careful selection of the available spectroscopic datasets is performed in order to minimize the fitting residuals. A thorough discussion of the retrieval strategy and data characterization (information content and error budget) is presented here along with trend analysis and preliminary comparison with the three-dimensional state-of-the-art global chemical transport model (CTM) GEOS-Chem.

This paper is organized as follows. A detailed description of the optimized retrieval strategy is given in Section 2. Section 3 reports the characterization of the FTIR geophysical products and provides a detailed error budget. Supporting model simulations are described in Section 4. Section 5 presents a preliminary comparison between FTIR and GEOS-Chem seasonal cycles of the C_2H_6 burden above Jungfraujoch as well as the entire 1994–2014 time series of daily-mean total columns and corresponding trends. Section 6 concludes this study with a short summary and discussions of the results, identifying avenues for future work.

2. FTIR data set

2.1. Instrumental setup

All the spectra analyzed here have been recorded at ISSJ, located in the Swiss Alps at 3580 m altitude on the saddle between the Jungfrau (4158 m a.s.l.) and the Mönch (4107 m a.s.l.) summits. This station offers excellent conditions to perform solar observations, particularly in the infrared, because of weak local pollution (no major industries within 20 km) and very high dryness thanks to the high-altitude and the presence of the Aletsch Glacier. Indeed, the amount of water vapor (H_2O), a strong interference in the infrared, is at least 20 times lower than at the sea level. Due to these factors, the ISSJ station allows for investigating the atmospheric background conditions over central Europe and the mixing of air masses from planetary boundary layer and free troposphere (e.g., [28,29]).

Here we use observations performed with a commercial Bruker IFS120HR instrument [26]. This spectrometer, affiliated to the NDACC network since 1991, is equipped with HgCdTe and InSb cooled detectors covering the 650–4500 cm^{-1} region of the electromagnetic spectrum.

The Bruker observational database investigated in the present study consists of more than 11,500 spectra recorded between September 1994 and August 2014 with an optical filter covering the 2400–3100 cm^{-1} range encompassing the perpendicular ν_7 fundamental stretching band of C_2H_6. Spectral resolutions, defined as the reciprocal of twice the maximum optical path difference, alternate between 0.004 and 0.006 cm^{-1}. The signal-to-noise (S/N) ratio varies between 300 and 4500 (average spectra resulting from several successive individual Bruker scans, when solar zenith angles vary slowly). The optimization of

the retrieval strategy has been based on a subset of about 600 spectra during 2003.

2.2. Retrieval strategy

The C_2H_6 column retrievals and profile inversions have been performed using the SFIT-2 v3.91 fitting algorithm. This retrieval code has been specifically developed to derive mixing ratio profiles of atmospheric species from ground-based FTIR spectra [17]. It is based on the semi-empirical implementation of the Optimal Estimation Method (OEM) developed as in [30]. Vertical profiles are derived from simultaneous fits to one or more spectral intervals of at least one solar spectrum with a multilayer, line-by-line calculation that assumes a Voigt line shape [31].

For the first time at ISSJ, C_2H_6 retrievals have been carried out using three micro-windows simultaneously (see Table 1). The first micro-window (MW1) is centered on the well-known strong and sharp $^pQ_3$ sub-branch of the perpendicular ν_7 fundamental stretching band [32] and extends from 2976.660 to 2977.059 cm^{-1}. This $^pQ_3$-MW1 is the only one taken into account previously for the Jungfraujoch station [19,27] and at many other FTIR sites (e.g., [21–23,33]). The second micro-window (MW2) includes the $^pQ_1$ sub-branch around 2983.3 cm^{-1}, as suggested in [34] and used in [24] in combination with MW1, and extends from 2983.200 to 2983.500 cm^{-1}. Finally, a third micro-window (MW3) encompasses the $^rQ_0$ C_2H_6 sub-branch around 2986.7 cm^{-1}, extending from 2986.450 to 2986.850 cm^{-1}. The MW3 has only been fitted at dry high-latitude sites [25,35] because of strong H_2O interferences. Within these micro-windows, the major interfering species whose vertical profiles are scaled during the retrieval process are CH_4, H_2O, O_3 and methyl chloride (CH_3Cl).

The model atmosphere adopted above the altitude of the ISSJ station consists of a 39-layer scheme extending from 3.58 km up to 100 km with progressively increasing thicknesses. The pressure–temperature profiles are provided by the National Centers for Environmental Prediction (NCEP, Washington DC, USA, http://www.ncep.noaa.gov/) while the solar line compilation supplied by [36] has been assumed for the non-telluric absorptions.

The C_2H_6 a priori mixing ratio profile corresponds to a mean of a 2007–2009 CHASER (Chemical AGCM for Study of atmospheric Environment and Radiative forcing; [37]) simulation (Fig. 1a; see Section 4.1). A priori profiles for all interfering molecules are based on the 1980–2020 simulation of the WACCM model (version 6 of WACCM profiles; the Whole Atmosphere Community Climate Model; e.g., [38]) for the ISSJ station.

In a usual OEM, the covariance matrix should reflect the natural variability of the target gas profile [39]. It is specified for each layer as a percentage of the a priori profile and an ad hoc correlation length, which is interpreted as a correlation between layers decaying along a Gaussian. For C_2H_6, we have adopted the relative standard deviation profile derived from the CHASER results (Fig. 1b) as the diagonal values of the covariance matrix and a Gaussian inter-layer correlation with a half-width length of 4 km for extra diagonal elements of the covariance matrix.

It is worth noting that this C_2H_6 retrieval strategy has been optimized in such a way to limit the fraction of retrieved profiles presenting negative mixing ratios. By setting up an inter-layer correlation of 4 km and the S/N ratio for inversion at 300, the retrieved information content at Jungfraujoch is slightly constrained deliberately but the retrieval process is stabilized and strong oscillations in the lower levels of the retrieved profiles are avoided. This way, less than 9% of solar spectra have been rejected because of ungeophysical retrieved mixing ratio values. Moreover, statistics have shown that there is no correlation between the seasonality and the fraction of rejected solar spectra. Hence we ensure here homogeneous data coverage and sampling throughout the entire time series (see Section 5.2).

Table 1
List of the micro-windows used for the FTIR retrieval of C_2H_6 at Jungfraujoch and the interfering species taken into account. Simple scaling of the corresponding vertical profiles of the interfering species is allowed throughout the iterative retrieval process.

Micro-windows (cm^{-1})	Interfering species
2976.660–2977.059	H_2O, O_3, CH_3Cl, CH_4
2983.200–2983.500	H_2O, O_3, CH_3Cl, CH_4
2986.450–2986.850	H_2O, O_3, CH_3Cl, CH_4

2.3. Spectroscopy

Ethane has a complicated spectrum with 12 interacting normal vibration modes, which makes it difficult to accurately predict the spectrum. Therefore, it is essential to take a closer look at the spectroscopic parameters. First C_2H_6 line parameters go back to the work of [40] with the assignment of C_2H_6 transitions but no ^pQ-branches were included. In 1987, to support the Atmospheric Trace Molecule Spectroscopy (ATMOS) Experiment, an empirical linelist for the 9 strongest ^pQ-branches of C_2H_6 covering the 2973–3001 cm^{-1} region was developed [41]. Pacific North West National Laboratory (PNNL, Washington, USA, http://nwir.pnl.gov) measured C_2H_6 cross-sections from 700 to 6500 cm^{-1} at a 0.1 cm^{-1} resolution while a quantum mechanically based linelist for the $^pQ_3$ branch at 2976 cm^{-1} was developed [32] and included in the HITRAN 2004 database [42]. The latest HITRAN C_2H_6 update (July 2007) contains Pine and Rinsland $^pQ_3$ branch as well as Brown's empirical linelist for the 8 other ^pQ-branches but still lacks information for weaker absorptions features.

Quantum-mechanical analysis of the C_2H_6 spectrum remains very difficult and is still lacking, except for the $^pQ_3$ branch. The current state of C_2H_6 parameters in HITRAN 2004 and HITRAN 2008 [43] is rather unsatisfactory in the 3 μm region for all spectral features other than the $^pQ_3$ branch. A new set of C_2H_6 cross-sections was therefore developed [44], based on new high resolution IR spectra recorded with and without additional synthetic air at the Rutherford Appleton Laboratory Molecular Spectroscopy Facility (RAL, UK, http://www.stfc.ac.uk/ralspace/)

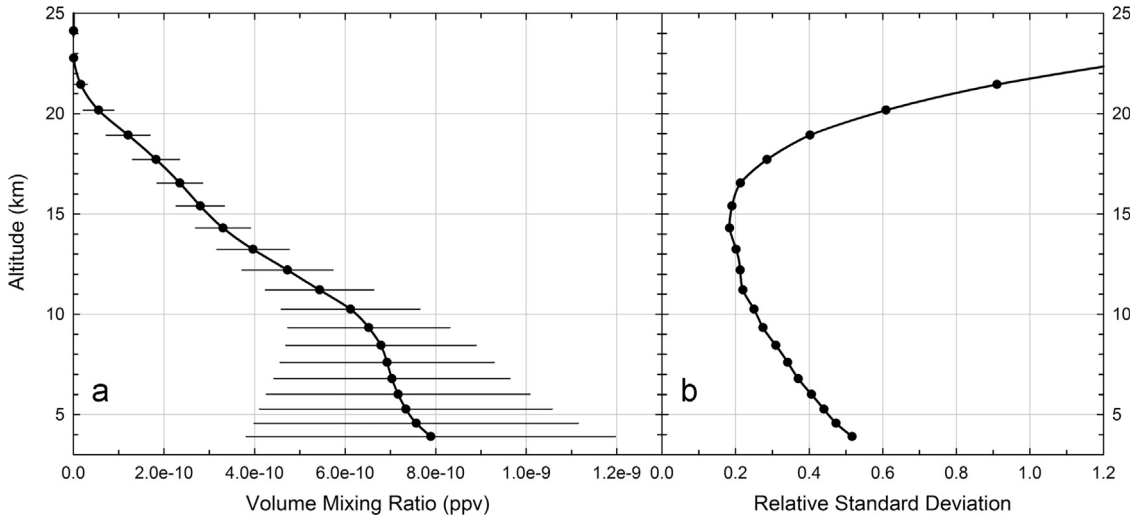

Fig. 1. (a) C_2H_6 a priori profile with 1-σ standard deviation derived from a 2007–2009 CHASER simulation used for the FTIR retrievals at Jungfraujoch. (b) Averaged relative standard deviation of C_2H_6 VMR derived from the same CHASER simulation and used as diagonal elements of the covariance matrix for the FTIR retrievals.

using a high resolution FTIR spectrometer. These cross sections for C_2H_6 have been measured in the 3 μm spectral region and calibrated in intensity by using low resolution spectra from the PNNL IR database as a reference. Finally, Lattanzi et al. [45] published a linelist including an improved representation of P- and R-branch lines of C_2H_6. However, based on the quality of fits to Harrison's lab spectra, it has been evaluated that the Q-branch features which we use for our retrieval strategy are poorly represented compared to HITRAN 2008, (evaluation of this linelist can be found at http://mark4sun.jpl.nasa.gov/report/Evaluation_of_Lattanzi_C2H6_linelist.pdf).

In 2011, an empirical pseudo-line-list (PLL) was fitted to Harrison's C_2H_6 lab spectra (the PLL and description can be found at http://mark4sun.jpl.nasa.gov/pseudo.html). The PLL generally provides a convenient and accurate way of interpolating/extrapolating in temperature and pressure to conditions not covered by lab measurements (Harrison's measurements in the case of this study for C_2H_6). In the present work, these pseudo-lines have been combined and tested with three versions of HITRAN (i.e. 2004, 2008 and 2012; [42,43,46]).

As the 2950–3020 cm^{-1} region encompasses absorption features from many atmospheric gases, the related spectroscopic parameters need to be as complete and accurate as possible in order to best simulate the atmospheric spectra. To this end, in addition to the C_2H_6 PLL, two updates have been included in our linelist. The first one consists of an update for three O_3 lines (encompassed in MW1) provided by P. Chelin (Laboratoire de Physique Moléculaire pour l'Atmosphère et l'Astrophysique, Paris, France, Personal Communication, 2004) in the framework of the UFTIR (Time series of Upper Free Troposphere observations from an European ground-based FTIR network) project. The second update concerns the CH_3Cl line positions and line intensities for the ν_1, ν_4 and $3\nu_6$ CH_3Cl bands in the 3.4 μm region (see [47,48]). Fourier transform spectra have been recorded at high resolution at the Laboratoire de Dynamique, Interactions et Réactivité in France. Measurements of line positions and line intensities have been performed for both isotopologues $^{12}CH_3$ ^{35}Cl and $^{12}CH_3$ ^{37}Cl in the ν_1, ν_4, $3\nu_6$ bands and line intensities have been compared to the recent integrated intensities from PNNL.

Table 2 summarizes the residuals (relative to observations) and mean retrieved columns associated with the use of the HITRAN 2004 (including the August 2006 updates; e.g., [49]), 2008 and 2012 compilations with the different spectroscopic improvements mentioned above. Note that the CH_3Cl update tested here is already part of the original HITRAN 2012 release. These tests have been performed on a subset of 229 representative solar spectra from the year 2003. Fig. 2 displays mean observed and calculated spectra as well as residuals, and illustrates the improvement of residuals brought by each update compared to the initial HITRAN 2008 database. By comparing residuals for each micro-window, we can evaluate the major contributions brought by the C_2H_6 PLL and O_3 updates (Fig. 2b) compared to the original HITRAN 2008 parameters (Fig. 2a). Finally, Fig. 2c shows a refinement of residuals on the edges of MW1 and MW3 due to the use of the CH_3Cl update. From Table 2 it appears that HITRAN 2008 along with the three updates minimizes the residuals in all micro-windows and hence is currently the best spectroscopic database to employ for ISSJ solar spectra. It is worth noting that the increased residuals observed with the HITRAN 2012 compilation compared to the set up using HITRAN 2008, especially in MW2 (see Table 2), are due to changes in H_2O parameters, more particularly in temperature and pressure-dependency parameters of the H_2O feature at 2983.316 cm^{-1}.

3. Data characterization and error budget

3.1. Characterization of the FTIR retrievals

The averaging kernel matrix (**A**) is resulted by the inversion process of FTIR solar spectra and characterizes

Table 2
Root mean square (RMS) residuals of the calculated spectra relative to observations (in %) for each micro-window when fitting a representative subset of 229 solar spectra from the year 2003 and using different combinations of spectroscopic parameters (see first column). These residuals are displayed in Fig. 2 for the HITRAN 2008 compilation and updates. Note that HITRAN 2004 includes the August 2006 updates and that the CH_3Cl update tested here is already part of the original HITRAN 2012 release. The averages of the resulting column values ($\times 10^{16}$ molec cm^{-2}) are listed in the last column. A typical and representative standard deviation of 25% is associated with these mean columns.

Spectroscopic parameters	RMS (%)			Mean column ($\times 10^{16}$ molec cm^{-2})
	MW1	MW2	MW3	
HITRAN 2004	0.2118	0.2974	0.5213	1.08
HITRAN 2004 + C_2H_6 PLL	0.1905	0.2283	0.1626	1.00
HITRAN 2004 + C_2H_6 PLL + O_3	0.1406	0.2283	0.1648	0.99
HITRAN 2004 + C_2H_6 PLL + O_3 + CH_3Cl	0.1158	0.2357	0.1410	1.01
HITRAN 2008	0.4705	0.1772	0.5200	1.03
HITRAN 2008 + C_2H_6 PLL	0.1329	0.1332	0.1627	0.97
HITRAN 2008 + C_2H_6 PLL + O_3	0.1316	0.1331	0.1623	0.98
HITRAN 2008 + C_2H_6 PLL + O_3 + CH_3Cl	0.1067	0.1179	0.1379	0.99
HITRAN 2012 + C_2H_6 PLL + O_3	0.1230	0.2151	0.1657	0.96

the information content of the retrievals. It describes how the retrieved concentration and vertical distribution of an absorber in the atmosphere are related to the true profile (x_t) and also provides the contribution of the a priori (x_a) to the retrieved profile (x_r) according to Eq. (1).

$$x_r = x_a + \mathbf{A}(x_t - x_a) \quad (1)$$

Fig. 3 displays the mean averaging kernels for each vertical layer (Fig. 3b; expressed in molec cm^{-2} / molec cm^{-2}) and calculated on the basis of the 2008–2010 individual retrieved profiles, as well as the leading eigenvalues and eigenvectors (Fig. 3a). The vertical sensitivity of our retrieval strategy is illustrated by the total column averaging kernel drawn in black dashed line in Fig. 3b (here with values divided by 10 for visibility purpose). It indicates very good sensitivity to the true state of the atmosphere below ~13 km altitude, with 99% of the information content independent from the a priori profile ($\boldsymbol{x_a}$) and mainly provided by the first eigenvector. The second and third eigenvectors and their associated eigenvalues indicate that the sensitivity of the retrievals extends in the lower stratosphere up to ~20 km, with some additional vertical resolution.

With a mean degree of freedom for signal (DOFS) of 2.11 ± 0.27 (1-σ confidence interval calculated over all 2008–2010 fitted spectra) and the two leading eigenvalues equal to 0.99 and 0.86, two independent pieces of information may be deduced from the averaging kernels. A first partial column is derived in the lower troposphere (from the ISSJ elevation up to ~8.5 km altitude) and a second one spanning the 8.5–22 km altitude range is identified in the upper troposphere – lower stratosphere. The sensitivity of our retrieval strategy is slightly diminishing for altitudes above ~13 km, but a large part of the information content (at least 60%) is still provided by the measurements at the 22 km level. Although independent partial columns are available from the retrieval process at ISSJ, we will only consider total columns of C_2H_6 in this study.

When compared with other recent works using pseudo-lines to retrieve C_2H_6 amounts, the content of information obtained from our retrievals is consistent with results from e.g., [25] at Eureka, Canada (80.0°N, 86.4°W, 610 m a.s.l.; DOFS = 2.00 ± 0.20) who also employed the three micro-windows, and represents a significant improvement compared to previous works carried out at ISSJ, with typical DOFS of about 1.5 when using the $^pQ_3$ feature alone. The simultaneous use of the three non-contiguous micro-windows allows for a significant gain in retrieved information content compared to three non-simultaneous retrievals which would be subsequently averaged. The DOFS obtained from the individual use of each micro-window is 1.51 ± 0.24, 1.86 ± 0.25 and 1.70 ± 0.23 for MW1, MW2 and MW3, respectively.

3.2. Error budget

Table 3 summarizes the major sources of uncertainty that may affect the C_2H_6 columns retrieved from the ISSJ solar spectra, as well as estimates of their respective contribution to either systematic or random component of the error budget. The total errors are the square root of the sum of the squares of each of the contributing uncertainty sources. Most of the error contributions (excepting when specified below) have been calculated on the basis of all solar spectra from year 2003 according to the sensitivity tests listed in the last column of Table 3. The C_2H_6 retrieval is also characterized at ISSJ by an assumed variability of 29.2% and a daily relative standard deviation (calculated here for the days with at least three observations) equal to 4.0%.

The major contribution to the systematic component of the error budget comes from uncertainties on the C_2H_6 spectroscopy. An error of 4% on the line intensity from the original spectra measurements has been reported in [44]. In addition, the uncertainty induced by the conversion of C_2H_6 cross-sections into pseudo-lines is estimated at 4% (see [52]), including the random error in the pseudo-line spectroscopic parameters and the systematic error due to an imperfect representation of the physics by the pseudo-lines. We have combined the 4% from [44] in quadrature with the 4% from the conversion into pseudo-lines, giving a conservative uncertainty of 5.6% on the C_2H_6 absorption. When assuming this uncertainty during the inversion

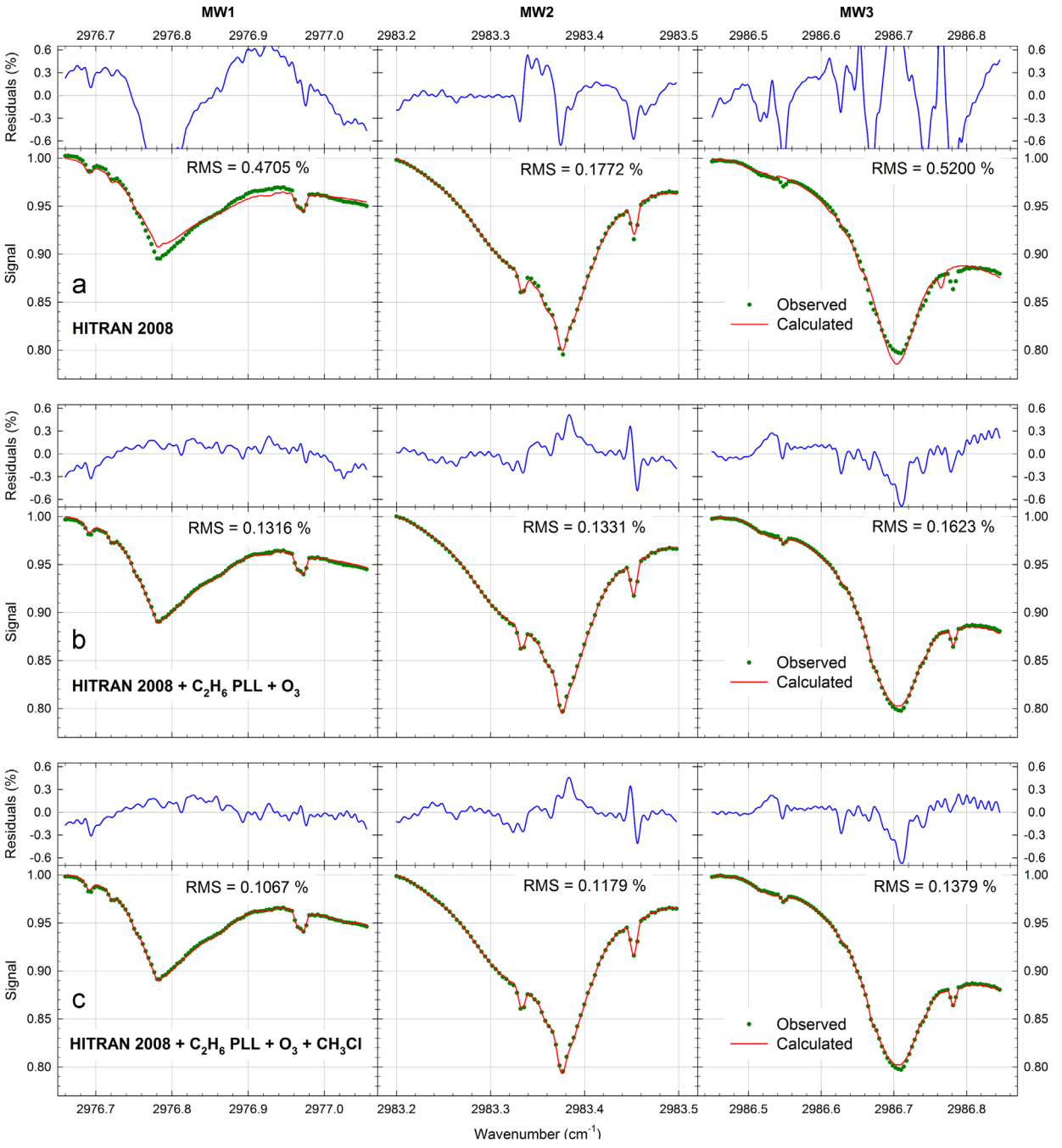

Fig. 2. Mean observed (green dots) and calculated (red lines) spectra and associated residuals (obs. – calc.; blue lines) for a representative subset of 229 spectral fits within the three micro-windows used for the C_2H_6 retrieval at ISSJ. Spectroscopic compilations used here are (a) the original HITRAN 2008 database, (b) HITRAN 2008 combined with the C_2H_6 PLL as well as O_3 update and (c) HITRAN 2008 combined with C_2H_6, O_3 and updated CH_3Cl lines. Note the improvements brought by the different updates on the residuals, whose mean values are also provided in Table 2. (For interpretation of the references to color in this figure caption, the reader is referred to the web version of this paper.)

process, the retrieved C_2H_6 columns are affected by systematic anomalies of 5.6%.

Retrieved column biases due to line intensity uncertainties related to the interfering species have been gauged independently by assuming the maximum errors quoted in the HITRAN 2008 (for H_2O, CH_4 and O_3) and HITRAN 2012 (for the CH_3Cl updated line parameters, included in this official release) databases during the fitting process. The column anomalies corresponding to each interfering gas have been combined in quadrature and contribute for 0.9% to the systematic component of the error budget.

Other contributions to the total systematic error are minor. The total columns are retrieved from high quality solar spectra using the SFIT algorithm within uncertainties

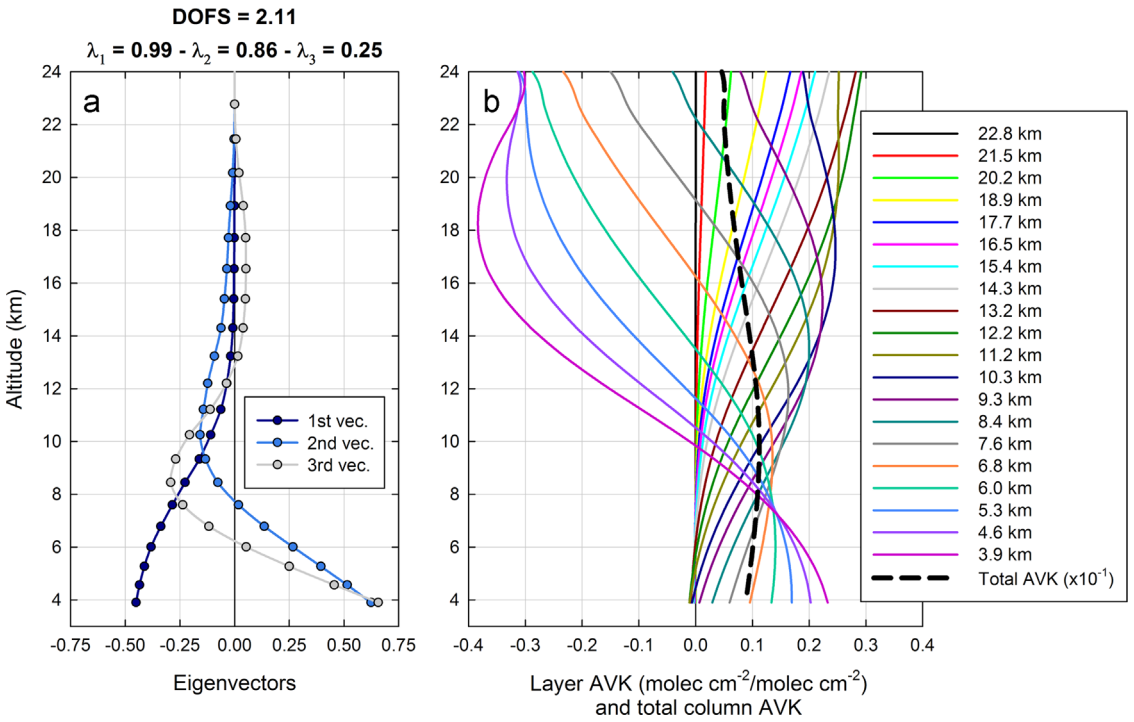

Fig. 3. (a) First eigenvectors and associated eigenvalues, and (b) individual averaging kernels for each layer between the 3.6 and 24.0 km altitude range and total column averaging kernel (thick dashed line; divided here by 10 for visibility purpose) characterizing the FTIR retrievals of C_2H_6 at ISSJ. The information content has been established on the basis of all the individual retrieved profiles throughout the 2008–2010 time span. The averaging kernels from 2008–2010 are used in Section 5.1 to smooth GEOS-Chem profiles in comparison with the FTIR products. Moreover, tests have shown that the DOFS, eigenvectors and averaging kernels calculated on the basis of other years provide consistent results in terms of information content.

Table 3
Error budget of the C_2H_6 retrievals at ISSJ, including the impact of systematic and random uncertainties on total columns retrieved from all individual solar spectra recorded during the year 2003, according to specifics given in the last column. The contributions of measurement noise, smoothing and model parameters have been estimated on the basis of a representative subset of solar spectra following the formalism of [50].

Error source	Error (%)	Comments
Assumed variability	29.2	
Relative standard deviation	4.0	For the days with at least 3 observations
Systematic errors		
C_2H_6 spectroscopy and conversion into pseudo-lines	5.6	$\pm$5.6% uncertainty on line intensity
Line intensity of interfering gases	0.9	HITRAN 2008 uncertainties (up to 10% for H_2O, 20% for O_3, 30% for CH_4 and 20% for CH_3Cl)
ILS	0.1	$\pm$10% misalignment and instrument bias
Forward model	1.0	Retrieval algorithm-related
C_2H_6 a priori profile	1.2	C_2H_6 a priori profiles derived from GEOS-Chem and WACCM
Total Systematic Error	5.9	
Random errors		
Temperature profiles	1.3	NCEP profile uncertainty (see text)
H_2O a priori profile	0.1	Changes by a factor of 2 in H_2O a priori slope
Solar Zenith Angle (SZA)	0.8	$\pm$0.2° bias
Measurement noise	1.6	
Smoothing	1.1	
Model parameters	0.2	
Total Random Error	2.4	

estimated at $\pm$1% (see [53]). The impact of an assumed instrumental misalignment of $\pm$10% at the maximum path difference on the retrieved columns is almost negligible (0.1%). Finally, the impact of the selection of the a priori C_2H_6 state on the retrieved columns is estimated by adopting other realistic C_2H_6 mixing ratio profiles simulated by the GEOS-Chem and WACCM models as a priori, which leads to small divergences by up to 1.2%.

As random errors, we have assumed a 0.2° error in the solar pointing and have adopted the temperature-profile uncertainties quoted by NCEP (±1.5 °C between the ground and 20 km altitude, ±2.0 °C for the 20–30 km altitude range, and from ±5 °C at 35 km up to ±9 °C at the stratopause). The corresponding biases on the retrieved C_2H_6 columns amount to 0.8 and 1.3%, respectively. As in [54], we have also made the tropospheric slope of the H_2O a priori profile vary by a factor of 2; such perturbations only induce 0.1% bias in the C_2H_6 columns, highlighting the independence of the C_2H_6 retrieval to the tropospheric water vapor content for a dry high-altitude site.

According to the formalism of [50] and such as detailed in Section 2.2.2 in [51], we have computed the gain and sensitivity matrices of a subset of solar spectra representative of the ISSJ dataset in terms of S/N ratio, DOFS, solar zenith angle, residuals, etc., eventually providing the respective contributions of measurement noise (1.6%), smoothing (1.1%) and forward model parameters (0.2%) to the total random error.

The estimated total systematic and random errors affecting our retrieved C_2H_6 columns amount to 5.9 and 2.4%, respectively. The latter represents a significant improvement compared to [19], where only the 2976–2977 cm^{-1} micro-window with the $^pQ_3$ branch for inversion of the ISSJ solar spectra is used and where the random component of the error budget is estimated in a similar way at 6.6% (and also found 5.9% of total bias for the systematic component).

4. Supporting model simulations

4.1. CHASER

The CHASER model [37,55], developed mainly in the Nagoya University and the Japan Agency for Marine-Earth Science and Technology (JAMSTEC), is a chemistry coupled climate model, simulating atmospheric chemistry and aerosols in cooperation with the aerosol component model SPRINTARS (Spectral Radiation-Transport Model for Aerosol Species; [56]). It has also been developed in the framework of the Model for Interdisciplinary Research on Climate-Earth System Model, MIROC-ESM-CHEM [57]. CHASER simulates detailed chemistry in the troposphere and stratosphere with an on-line aerosol simulation including production of particulate nitrate and secondary organic aerosols.

For this study, the model's horizontal resolution is selected to be 2.8° × 2.8° with 36 vertical layers extending from the surface up to about 50 km altitude. As the overall model structure, CHASER is fully coupled with the climate model core MIROC, permitting atmospheric constituents (both gases and aerosols) to interact radiatively and hydrologically with meteorological fields in the model. For replicating the past meteorological conditions in the model, this study employs a nudged chemical transport model version of CHASER in which wind fields and temperatures calculated by the MIROC's AGCM are relaxed to meteorological reanalysis data. In this study, the NCEP final reanalysis data set is used as a nudging constraint with the HadISST data set (Hadley Centre Sea Ice and Sea Surface Temperature) for distributions of sea surface temperatures and sea ice. Chemistry component of CHASER considers the chemical cycle of O_x–NO_x–HO_x–CH_4–CO with oxidation of Non-Methane Volatile Organic Compounds (NMVOCs), halogen chemistry and NH_x–SO_x–NO_3 system simulating 96 chemical species with 287 chemical reactions. In the model, NMVOCs include C_2H_6, C_2H_4, propane (C_3H_8), C_3H_6, C_4H_{10}, acetone, methanol and biogenic NMVOCs (isoprene, terpenes).

Anthropogenic emissions (for NO_x, CO, CH_4, NMVOCs, NH_3, SO_2, black carbon and organic carbon) are specified using the EDGAR-HTAP2 (Emission Database for Global Atmospheric Research, targeted for 2008: http://edgar.jrc.ec.europa.eu/) and fire emissions are based on the MACC's reanalysis data (Monitoring Atmospheric Composition & Change; https://gmes-atmosphere.eu/about/project_structure/input_data/d_fire/) for individual years/months. For biogenic NMVOC emissions, we employ calculation by the land ecosystem/trace gas emission model VISIT (Vegetation Integrative SImulator for Trace gases; [58]).

4.2. GEOS-Chem

GEOS-Chem (version 9-01-03: http://acmg.seas.harvard.edu/geos/doc/archive/man.v9-01-03/index.html) is a global 3-D CTM capable of simulating global trace gas and aerosol distributions. GEOS-Chem is driven by assimilated meteorological fields from the Goddard Earth Observing System version 5 (GEOS-5) of the NASA Global Modeling Assimilation Office (GMAO). The GEOS-5 meteorology data have a temporal frequency of 6 h (3 h for mixing depths and surface properties) and are at a native horizontal resolution of 0.5° × 0.667° with 72 hybrid pressure-σ levels describing the atmosphere from the surface up to 0.01 hPa. In the framework of this study, the GEOS-5 fields are degraded for model input to a 2° × 2.5° horizontal resolution and 47 vertical levels by collapsing levels above ~80 hPa. The chemical mechanism applied here is the standard full chemistry GEOS-Chem simulation, including detailed O_3–NO_x–Volatile Organic Compound (VOC) – aerosol coupled chemistry (see [59,60] for full description) with updates by [61].

Ethane is emitted from anthropogenic and pyrogenic sources in GEOS-Chem. The RETRO (REanalysis of the TROpospheric chemical composition) emission inventory [62] is the global default for anthropogenic NMVOC emissions aside from C_2H_6 and C_3H_8. Ethane and C_3H_8 emissions in RETRO are low compared to the GEOS-Chem inventories from [3], which are unbiased relative to the pre-2004 observations presented as in [3]. Thus we used the C_2H_6 and C_3H_8 emission inventories from [3]. Ethane emissions from biomass burning are from the Global Fire Emissions Database (GFED3) monthly biomass burning emissions [63].

The GEOS-Chem model output presented here covers the period July 2005–May 2013, for which the GEOS-5 meteorological fields are available. We have used a one-year run for spin-up from July 2004 to June 2005, restarted several times for chemical initialization. The model outputs consist of C_2H_6 mixing ratio profiles at a 3-h time

frequency, saved at the closest $2^\circ \times 2.5^\circ$ pixel of the ISSJ station. To account for the vertical resolution and sensitivity of the FTIR retrievals, the individual concentration profiles simulated by GEOS-Chem are interpolated onto the vertical grid of FTIR. They are then averaged into daily profiles and eventually smoothed by applying the FTIR averaging kernels **A** (see Eq. (1)) according to the formalism of [39]. The averaging kernels used to convolve the model outputs are seasonal averages over March–May, June–August, September–November and December–February obtained from the 2008–2010 individual FTIR retrievals. The following comparison between FTIR and smoothed GEOS-Chem data involves the days with observations available within the July 2005–May 2013 time period only (i.e. 915 days of observations).

5. Ethane time series

In this section, we first present a preliminary comparison between C_2H_6 FTIR total columns and simulations by the GEOS-Chem model by illustrating the seasonal cycle of C_2H_6 at ISSJ. We have taken into account the vertical resolution and specific sensitivity of the FTIR retrievals before comparison with the model data. We then report the entire 1994–2014 time series of daily-mean total columns and corresponding trends.

5.1. Seasonal cycle

The seasonal cycle of C_2H_6 abundances above ISSJ is illustrated in Fig. 4, which displays on a 1-year time base the monthly means of FTIR total columns and associated 1-σ standard deviation as error bars. The running mean of the FTIR daily average data (not shown here), computed using a 2-month integration length and a 15-day time step, is drawn in solid blue line. The shaded area corresponds to the 1-σ standard deviation around the running mean. The FTIR data subset used in Fig. 4 spans the July 2005–May 2013 time period in order to coincide with the GEOS-Chem simulation. A similar running mean and standard deviation have also been calculated on the basis of the daily-averaged total columns simulated by GEOS-Chem (after smoothing by the FTIR averaging kernels). These are represented by the red curve and by the shaded area in Fig. 4, respectively.

The seasonal cycle of C_2H_6 apparent in the FTIR total column data and model output are in good agreement, characterized by a maximum in March–April and a minimum in August–September. Since fossil fuel production is the main source of C_2H_6 emissions [3] and does not present a particular seasonal cycle during the year [64], the strong seasonal cycle of C_2H_6 burden is primarily driven by the photochemical oxidation rate by OH radicals, which is enhanced during summer [65,66]. At mid and high latitudes, C_2H_6 accumulates during wintertime and peaks in late winter due to its relatively long lifetime and slow exchange with lower latitudes [19]. Consistent values of seasonal amplitude, i.e. the difference between the maximum and minimum running means divided by the annual average over the whole time period, are associated with these seasonal modulations: 50.4% and 57.3% for FTIR and GEOS-Chem, respectively. A direct comparison between the daily-mean C_2H_6 total columns derived from the CTM and ground-based observations is presented in Fig. 5 and shows a correlation R of 0.77.

However, it appears clearly on Figs. 4 and 5 that the C_2H_6 burden simulated by GEOS-Chem is systematically lower than the FTIR measurements. Over the mid-2005–mid-2013 time period, the daily-averaged modeled C_2H_6 columns present a systematic bias of $-26.7 \pm 16.5\%$ relative to the FTIR daily means, and the two data sets cannot be reconciled by accounting for the systematic errors affecting the observations (see Table 3). The systematic bias is hypothesized to be driven by an underestimation of

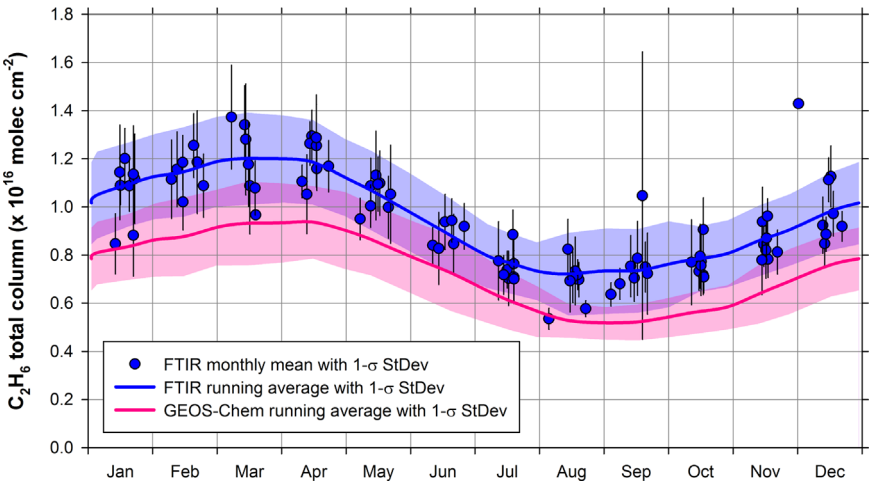

Fig. 4. Monthly-averaged total columns of C_2H_6 and associated 1-σ standard deviation bars displayed on a 1-year time base, from the FTIR retrievals performed above ISSJ between July 2005 and May 2013. The blue curve and shaded area show on a 1-year time base the running mean fit to the daily-averaged columns (with a 2-month wide integration time and a 15-day time step) and the associated 1-σ standard deviation, respectively. The red line and shaded area represent corresponding information, but deduced from the smoothed GEOS-Chem output. Note that the 1-σ standard deviations around the running mean are calculated on the basis of the daily-averaged columns and hence include interannual fluctuations as well as variability of the monthly mean. (For interpretation of the references to color in this figure caption, the reader is referred to the web version of this paper.)

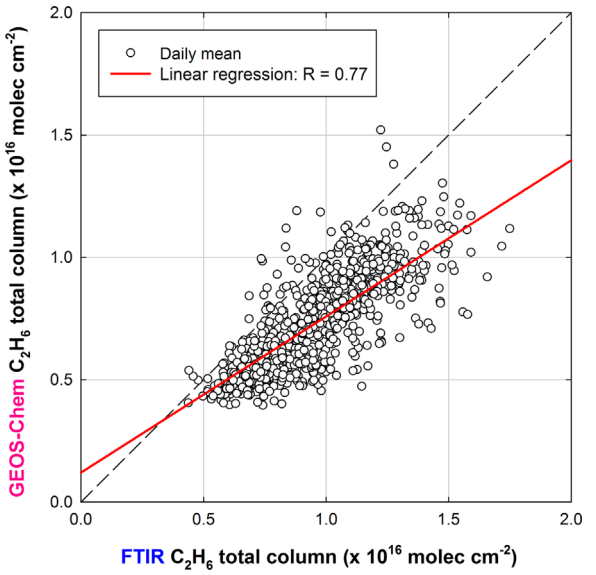

Fig. 5. FTIR daily-averaged total columns of C_2H_6 versus daily-averaged C_2H_6 abundances derived from smoothed GEOS-Chem profiles over the July 2005–May 2013 time span. The straight red line corresponds to the linear regression (with *R* as the correlation coefficient) between both data sets. (For interpretation of the references to color in this figure caption, the reader is referred to the web version of this paper.)

the C_2H_6 emissions used by the model that were developed only considering data collected prior to 2004. Incorporating updated and more accurate emission inventories into GEOS-Chem is the focus of ongoing work and is beyond the scope of this paper.

The retrieved columns of C_2H_6 at ISSJ are consistent with ground-based FTIR measurements from other stations in terms of amounts and seasonal cycle, taking into account the latitude and elevation of the ISSJ station (see [5,20–25,67]). At high-altitude stations such as ISSJ, lower burden and seasonal amplitude are generally observed due to high concentrations of C_2H_6 in the lowest tropospheric layers [23]. For instance, monthly-mean columns ranging between 1.76 ± 0.40 and $3.36 \pm 0.30 \times 10^{16}$ molec cm^{-2} and a corresponding seasonal amplitude of 63% were obtained from ground-based FTIR solar spectra recorded over 1995–2000 at two Northern Hemisphere mid-latitude (44°N) stations located almost at the sea level in Japan [21]. The amplitude of the seasonal cycle is generally larger at high-latitude sites because of the enhanced fossil fuel emissions [67] and very weak oxidation rate by OH radicals in winter, allowing C_2H_6 to accumulate substantially during this season. At Eureka, [25] retrieved monthly-mean C_2H_6 columns between 1.2 and 2.85×10^{16} molec cm^{-2} from FTIR observations for 2007–2011, and the amplitude of the seasonal cycle was 93%.

5.2. Long-term trend

Fig. 6 presents the long-term time series of daily-averaged C_2H_6 total columns (in molec cm^{-2}) retrieved from the ISSJ solar spectra for the September 1994–August 2014 time period, which consists of 11,859 measurements spread over 2224 days of observation. The error bars associated with these daily means correspond to the 1-σ standard deviation of the measurements within each day. This FTIR database homogeneously covers the investigated time span. We have used the statistical bootstrap resampling tool developed as in [22] to fit the whole daily time series in order to determine the C_2H_6 long-term linear trend (as well as the associated uncertainty) and the seasonal modulation. This bootstrap method combines a linear function and a 3rd order Fourier series taking into account the intra-annual variability of the data set.

Moreover, a running mean of the daily average data with a 3-year wide integration time and a 6-month step has revealed a minimum in the time series between the end of 2008 and the beginning of 2009. Therefore we have fitted both 1994–2008 and 2009–2014 time periods separately with the bootstrap tool that has returned two statistically-significant trends of C_2H_6 total columns at the 2-σ confidence level: $-9.56 \pm 1.91 \times 10^{13}$ molec cm^{-2} $year^{-1}$ and $4.35 \pm 0.81 \times 10^{14}$ molec cm^{-2} $year^{-1}$, respectively. Then we have used both 1995.0 and 2009.0 columns modeled by the bootstrap tool as references in order to calculate the relative annual trends.

Analysis of the 1994–2008 time span reveals a regular decrease of the C_2H_6 amounts above ISSJ by $-0.92 \pm 0.18\%$ $year^{-1}$ relative to 1995.0. This negative trend is consistent with measurements and corresponding trends of atmospheric C_2H_6 burden presented in [66,68], both studies attributed the decline of global C_2H_6 emissions from the mid-1980s to reduced fugitive emissions from fossil fuel sources in Northern Hemisphere rather than a decrease in biomass burning and biofuel use (the other major sources of C_2H_6). These fugitive emissions mainly include natural gas loss due to evaporation, venting and flaring as well as equipment leaks during the production and processing of natural gas and oil. Consistent trends derived from FTIR solar spectra have already been reported at ISSJ by previous studies, but over shorter time periods: $-2.70 \pm 0.30\%$ $year^{-1}$ over 1985–1995 [27], $-1.20 \pm 0.65\%$ $year^{-1}$ over 1995–1999 [19], $-1.05 \pm 0.35\%$ $year^{-1}$ over 1995–2004 [22] and $-1.51 \pm 0.23\%$ $year^{-1}$ over 1996–2006 [23]. Global C_2H_6 emissions did not decline as rapidly between 2000 and 2010 period compared to the 1980s and 1990s [66,68], and this is consistent with our reported negative trend, which is smaller than reported in previous ISSJ studies.

Conversely, for the 2009–2014 time period, the bootstrap tool reveals a strong positive trend of C_2H_6 total columns of $4.90 \pm 0.91\%$ $year^{-1}$ relative to 2009.0 above ISSJ. We have also applied the bootstrap tool to the 3.58–8.88 and 8.88–22.10 km partial columns of C_2H_6 above ISSJ (see Section 3.1) and have found very similar positive trends relative to 2009.0, suggesting a vertically-homogeneous increase of C_2H_6 throughout the troposphere (and lower stratosphere). To our knowledge, this recent increase of the C_2H_6 burden in the background atmosphere has not been reported and its origin is still unidentified.

A hypothetical source may be enhanced fugitive emissions of C_2H_6 linked to the recent growth in the exploitation of shale gas and tight oil reservoirs. The growth has been especially massive in North America. Indeed, positive

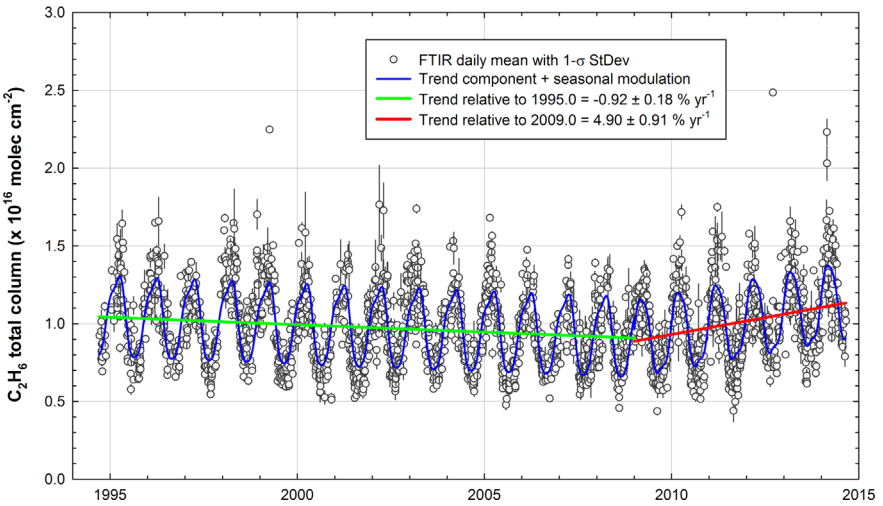

Fig. 6. FTIR time series of daily-averaged C_2H_6 total columns and associated 1-σ standard deviation bars above ISSJ from September 1994 to August 2014. The functions fitted to all available daily means (including seasonal modulation and trend component) and calculated by the bootstrap resampling tool of [22] over the 1994–2008 and 2009–2014 time periods are drawn in blue curve. The green and red solid lines correspond to the trend components of these fitting functions. (For interpretation of the references to color in this figure caption, the reader is referred to the web version of this paper.)

anomalies of CH_4 related to the oil and gas industries have been recently detected from space over regions of North America where the drilling productivity began to grow rapidly after 2009 (see [69]). This hypothesis is supported by measurements derived from 1986 solar occultation observations performed over North America (16°–88°N and 173°–50°W) between 2004 and the middle of 2013 by the ACE-FTS instrument [70]. We employed the version 3.5 ACE-FTS data [71], which includes an improved retrieval strategy for C_2H_6, within the 8–16 km altitude range. Applying the bootstrap tool to the ACE-FTS partial columns over the 2004–2008 and 2009–2013 time periods, we have calculated statistically-significant trends (at the 2-σ level) of -1.75 ± 1.30 and $9.4 \pm 3.2\%\,\text{year}^{-1}$ relative to 2004.0 and 2009.0, respectively, which are consistent with the FTIR trends when accounting for the associated uncertainty ranges. Trends derived from 906 ACE-FTS measurements between 10° and 40°S do not reveal any recent increase of the C_2H_6 burden. Instead these data show a statistically significant decrease ($-1.62 \pm 1.08\%\,\text{year}^{-1}$) over the 2004 to mid-2013 time period. This suggests that the observed increase of C_2H_6 is limited to the Northern Hemisphere.

It is worth noting that the GEOS-Chem CTM does not reproduce this recent increase in the abundance of C_2H_6 above ISSJ, suggesting emission inventories for C_2H_6 and other light alkanes may not be properly accounting for the enhanced fugitive emissions from recent natural gas and oil production.

6. Discussions and conclusions

In this study, we have developed and optimized a new strategy based on an improved spectroscopy to retrieve C_2H_6 total and partial columns from ground-based FTIR solar spectra recorded at the dry and high-altitude ISSJ. The selected spectroscopic parameters accounted for in the three micro-windows include C_2H_6 pseudo-lines based on cross-section laboratory spectra as well as updated line features for O_3 and CH_3Cl. Such an improved spectroscopy has yielded substantially reduced fitting residuals, enhanced information content (with a mean DOFS of 2.11 ± 0.27 for the whole data set) and less solar spectra discarded because of ungeophysical mixing ratio profiles.

We have applied this strategy to the long-term FTIR time series available at ISSJ (spanning 1994–2014) and compared the retrieved total columns to C_2H_6 columns simulated by the GEOS-Chem CTM, taking into account the vertical sensitivity of the retrievals by convolving the modeled profiles with the FTIR averaging kernels. The observations and the model present consistent seasonal cycles, but GEOS-Chem under-predicts the observed C_2H_6 burden throughout the seasonal cycle. This suggests an underestimation of C_2H_6 emissions in the model and points to the need for improved inventories for further GEOS-Chem simulations and sensitivity tests.

Finally, we have presented the 20-year ISSJ time series of C_2H_6 column abundance. Using a bootstrap resampling tool, we have calculated a statistically-significant negative trend in C_2H_6 total columns until 2009, consistent with prior studies and with our understanding of global C_2H_6 emissions. However, the ISSJ time series has also revealed a strong positive trend in C_2H_6 over the last 6 years of the record, from 2009 onwards. Such a recent increase in the remote atmosphere is still unreported and, because of the involvement of C_2H_6 in the global VOC–HO_x–NO_x chemistry responsible for generating or destroying tropospheric O_3, investigating both its cause and its impact on air quality should be a high priority for the atmospheric chemistry community.

This C_2H_6 increase extends beyond previous positive short-term anomalies already observed in the Northern Hemisphere, which occur every 3–5 years and are generally associated with variability in biomass burning emissions [66,72]. The seasonal cycle of C_2H_6 above ISSJ is primarily driven by the photochemical cycle of its main

sink (OH radicals). We argue that it is unlikely that the recent increase can be attributed to sharp fluctuations of OH concentration in the atmosphere because the global OH levels have not exhibited large interannual variability since the end of the 20th century [73]. Indeed, neither CO nor other species that have oxidation by OH as their major removal pathway such as hydrogen cyanide (HCN) and acetylene (C_2H_2), do not present an upturn in their retrieved columns above ISSJ over the last years. However, CH_4, which is closely linked to C_2H_6 [66,72], has also presented globally a renewed rise after 2006 [74]. We hypothesize that the observed recent increase in C_2H_6 above ISSJ could represent a change in C_2H_6 throughout the Northern Hemisphere and may be the product of a large increase in fugitive emissions related to the recent upturn in the development of North American shale gas and tight oil reservoirs.

The lifetime of C_2H_6 is approximately 2 months, and this makes C_2H_6 influenced by vertical mixing and long-range transport. Ethane is therefore a convenient tracer of anthropogenic activity for remote sensing [65]. Measurements of C_2H_6 in the remote troposphere can also be used to identify air masses that have originated in regions with significant oil and gas production [66]. Air masses impacted by intense episodes of biomass burning have already been detected in the retrieved C_2H_6 columns at ISSJ, associated with severe tropical emissions from Asia during the strong El Niño event of 1997–1998 [19]. Our future work will focus on combining an analysis of C_2H_6 measurements from ground-based FTIR solar spectra and observations from ACE-FTS with dedicated GEOS-Chem simulations with updated inventories. The goal will be to identify the cause of the recent increase in C_2H_6 and evaluate the magnitude of emissions required to produce the observed changes.

Acknowledgments

The University of Liège contribution to the present work has mainly been supported by the AGACC-II project of the Science for Sustainable Development (SSD) program of the Belgian Science Policy Office (BELSPO, Brussels). Additional support was provided by MeteoSwiss (Global Atmospheric Watch), the Fédération Wallonie–Bruxelles and the F.R.S. – FNRS. We thank the International Foundation High Altitude Research Stations Jungfraujoch and Gornergrat (HFSJG, Bern). E. Mahieu is Research Associate with F.R.S. – FNRS. We are grateful to the many colleagues who have contributed to FTIR data acquisition at the Jungfraujoch station. We thank Jeremy Harrison and colleagues for their high quality lab measurements of C_2H_6. Part of this work was performed at the Jet Propulsion Laboratory, California Institute of Technology, under contract with NASA. Agnès Perrin would like to thank for financial support the French program LEFE-CHAT (Les Enveloppes Fluides et l'Environnement – Chimie Atmosphérique) of INSU (Institut des Sciences de l'Univers) from CNRS. Funding for Emily V. Fischer was provided by the U.S. National Oceanographic and Atmospheric Administration through award number NA14OAR4310148. This research was partly supported by the Global Environment Research Fund (S-7/12) by the Ministry of the Environment (MOE), Japan, and the Research Program on Climate Change Adaptation (RECCA) by the Ministry of Education, Culture, Sports, Science and Technology (MEXT), Japan. Funding for the Atmospheric Chemistry Experiment comes from the Canadian Space Agency.

References

[1] Rudolph J. The tropospheric distribution and budget of ethane. J Geophys Res 1995;100(D6):11369–81. http://dx.doi.org/10.1029/95JD00693.
[2] Logan JA, Prather MJ, Wofsy SC, McElroy MB. Tropospheric chemistry: a global perspective. J Geophys Res 1981;86(C8):7210–54, http://dx.doi.org/10.1029/JC086iC08p07210.
[3] Xiao Y, Logan JA, Jacob DJ, Hudman RC, Yantosca R, Blake DR. Global budget of ethane and regional constraints on US sources. J Geophys Res 2008;113(D21306). http://dx.doi.org/10.1029/2007JD009415.
[4] Aikin AC, Herman JR, Maier EJ, McQuillan CJ. Atmospheric chemistry of ethane and ethylene. J Geophys Res 1982;87(C4):3105–18, http://dx.doi.org/10.1029/JC087iC04p03105.
[5] Rinsland CP. Multiyear infrared solar spectroscopic measurements of HCN, CO, C_2H_6, and C_2H_2 tropospheric columns above Lauder, New Zealand (45°S latitude). J Geophys Res 2002;107(D14). http://dx.doi.org/10.1029/2001JD001150.
[6] Collins WJ, Derwent RG, Johnson CE, Stevenson DS. The oxidation of organic compounds in the troposphere and their global warming potentials. Clim Change 2002;52:453–79. http://dx.doi.org/10.1023/A:1014221225434.
[7] Fischer EV, Jacob DJ, Yantosca RM, Sulprizio MP, Millet DB, Mao J, et al. Atmospheric peroxyacetyl nitrate (PAN): a global budget and source attribution. Atmos Chem Phys 2014;14:2679–98, http://dx.doi.org/10.5194/acp-14-2679-2014.
[8] Toon GC. The JPL MkIV interferometer. Optics Photonics News 1991;2(10):19–21. http://dx.doi.org/10.1364/OPN.2.10.000019.
[9] Blake DR, Chen TY, Smith Jr. TW, Wang CJL, Wingenter OW, Blake NJ, et al. Three-dimensional distribution of nonmethane hydrocarbons and halocarbons over the northwestern Pacific during the 1991 Pacific Exploratory Mission (PEM-West A). J Geophys Res 1996;101(D1):1763–78. http://dx.doi.org/10.1029/95JD02707.
[10] Fishman J, Hoell JM, Bendura RD, McNeal RJ, Kirchhoff VWJH. NASA GTE TRACE A experiment (September–October 1992): overview. J Geophys Res 1996;101(D19):23865–79. http://dx.doi.org/10.1029/96JD00123.
[11] Chatfield RB, Vastano JA, Li L, Sachse GW, Connors VS. The Great African Plume from biomass burning: generalizations from a three-dimensional study of TRACE A carbon monoxide. J Geophys Res 1998;103(D21):28059–77. http://dx.doi.org/10.1029/97JD03363.
[12] Rinsland CP, Dufour G, Boone CD, Bernath PF, Chiou L. Atmospheric Chemistry Experiment (ACE) measurements of elevated Southern Hemisphere upper tropospheric CO, C_2H_6, HCN, and C_2H_2 mixing ratios from biomass burning emissions and long-range transport. Geophys Res Lett 2005;32(20). http://dx.doi.org/10.1029/2005GL024214.
[13] Browell EV, Hair JW, Butler CF, Grant WB, DeYoung RJ, et al. Ozone, aerosol, potential vorticity, and trace gas trends observed at high-latitudes over North America from February to May 2000. J Geophys Res 2003;108(D4):8369. http://dx.doi.org/10.1029/2001JD001390.
[14] Swanson AL, Blake NJ, Atlas E, Flocke F, Blake DR, Rowland FS. Seasonal variations of C_2–C_4 nonmethane hydrocarbons and C_1–C_4 alkyl nitrates at the Summit research station in Greenland. J Geophys Res 2003;108(D2):4064. http://dx.doi.org/10.1029/2001JD001445.
[15] Wingenter OW, Sive BC, Blake NJ, Blake DR, Rowland FS. Atomic chlorine concentrations derived from ethane and hydroxyl measurements over the equatorial Pacific Ocean: implication for dimethyl sulfide and bromine monoxide. J Geophys Res 2005;110(D20308). http://dx.doi.org/10.1029/2005JD005875.
[16] Glatthor N, von Clarmann T, Stiller GP, Funke B, Koukouli ME, Fischer H, et al. Large-scale upper tropospheric pollution observed by MIPAS HCN and C_2H_6 global distributions. Atmos Chem Phys 2009;9:9619–34. http://dx.doi.org/10.5194/acp-9-9619-2009.
[17] Rinsland CP, Jones NB, Connor BJ, Logan JA, Pougatchev NS, Goldman A, et al. Northern and southern hemisphere ground-based infrared spectroscopic measurements of tropospheric carbon monoxide and

ethane. J Geophys Res 1998;103(D21):28197–217. http://dx.doi.org/10.1029/98JD02515.
[18] Rinsland CP, Goldman A, Murcray FJ, Stephen TM, Pougatchev NS, Fishman J, et al. Infrared solar spectroscopic measurements of free tropospheric CO, C_2H_6, and HCN above Mauna Loa, Hawaii: seasonal variations and evidence for enhanced emissions from the Southeast Asian tropical fires of 1997–1998. J Geophys Res 1999;104(D15): 18667–80. http://dx.doi.org/10.1029/1999JD900366.
[19] Rinsland CP, Mahieu E, Zander R, Demoulin P, Forrer J, Buchmann B. Free tropospheric CO, C_2H_6, and HCN above central Europe: recent measurements from the Jungfraujoch station including the detection of elevated columns during 1998. J Geophys Res 2000;105(D19): 24235–49. http://dx.doi.org/10.1029/2000JD900371.
[20] Rinsland CP, Meier A, Griffith DWT, Chiou LS. Ground-based measurements of tropospheric CO, C_2H_6, and HCN from Australia at 34°S latitude during 1997–1998. J Geophys Res 2001;106(D18): 20913–24. http://dx.doi.org/10.1029/2000JD000318.
[21] Zhao Y, Strong K, Kondo Y, Koike M, Matsumi Y, Irie H, et al. Spectroscopic measurements of tropospheric CO, C_2H_6, C_2H_2, and HCN in northern Japan. J Geophys Res 2002;107(D18):4343, http://dx.doi.org/10.1029/2001JD000748.
[22] Gardiner T, Forbes A, de Mazière M, Vigouroux C, Mahieu E, Demoulin P, et al. Trend analysis of greenhouse gases over Europe measured by a network of ground-based remote FTIR instruments. Atmos Chem Phys 2008;86719–27. doi:http://dx.doi.org/10.5194/acp-8-6719-2008.
[23] Angelbratt J, Mellqvist J, Simpson D, Jonso JE, Blumenstock T, Borsdorff T, et al. Carbon monoxide (CO) and ethane (C_2H_6) trends from ground-based solar FTIR measurements at six European stations, comparison and sensitivity analysis with the EMEP model. Atmos Chem Phys 2011;11:9253–69. http://dx.doi.org/10.5194/acp-11-9253-2011.
[24] Vigouroux C, Stavrakou T, Whaley C, Dils B, Duflot V, Hermans C, et al. FTIR time-series of biomass burning products (HCN, C_2H_6, C_2H_2, CH_3OH, and HCOOH) at Reunion Island (21°S, 55°E) and comparisons with model data. Atmos Chem Phys 2012;12: 10367–85. http://dx.doi.org/10.5194/acp-12-10367-2012.
[25] Viatte C, Strong K, Walker KA, Drummond JR. Five years of CO, HCN, C_2H_6, C_2H_2, CH_3OH, HCOOH and H_2CO total columns measured in the Canadian high Arctic. Atmos Meas Tech 2014;7:1547–70, http://dx.doi.org/10.5194/amt-7-1547-2014.
[26] Zander R, Mahieu E, Demoulin P, Duchatelet P, Roland G, Servais C, et al. Our changing atmosphere: evidence based on long-term infrared solar observations at the Jungfraujoch since 1950. Sci Total Environ 2008;391 (2–3):184–95. http://dx.doi.org/10.1016/j.scitotenv.2007.10.018.
[27] Mahieu E, Zander R, Delbouille L, Demoulin P, Roland G, Servais C. Observed trends in total vertical column abundances of atmospheric gases from IR solar spectra recorded at the Jungfraujoch. J Atmos Chem 1997;28:227–43. http://dx.doi.org/10.1023/A:1005854-926740.
[28] Zellweger C, Forrer J, Hofer P, Nyeki S, Schwarzenbach B, Weingartner E, et al. Partitioning of reactive nitrogen (NO_y) and dependence on meteorological conditions in the lower free troposphere. Atmos Chem Phys 2003;3:779–96. http://dx.doi.org/10.5194/acp-3-779-2003.
[29] Reimann S, Schaub D, Stemmler K, Folini D, Hill M, Hofer P, et al. Halogenated greenhouse gases at the Swiss High Alpine Site of Jungfraujoch (3580 m asl): continuous measurements and their use for regional European source allocation. J Geophys Res 2004;109 (D05307). http://dx.doi.org/10.1029/2003JD003923.
[30] Rodgers CD. Characterization and error analysis of profiles retrieved from remote sounding measurements. J Geophys Res 1990;95(D5): 5587–95. http://dx.doi.org/10.1029/JD095iD05p05587.
[31] Drayson SR. Rapid computation of the Voigt profile. J Quant Spectrosc Radiat Transf 1976;16:611–4. http://dx.doi.org/10.1016/0022-4073(76)90029-7.
[32] Pine AS, Rinsland CP. The role of torsional hot bands in modeling atmospheric ethane. J Quant Spectrosc Radiat Transf 1999;62: 445–58. http://dx.doi.org/10.1016/S0022-4073(98)00114-9.
[33] Paton-Walsh C, Deutscher NM, Griffith DWT, Forgan BW, Wilson SR, Jones NB, Edwards DP. Trace gas emissions from savanna fires in northern Australia. J Geophys Res 2010;115(D16314). http://dx.doi.org/10.1029/2009JD013309.
[34] Meier A, Toon GC, Rinsland CP, Goldman A, Hase F. spectroscopic atlas of atmospheric microwindows in the middle infra-red. Kiruna, Sweden: IRF Institutet för Rymdfysik; 2004.
[35] Notholt J, Toon GC, Lehmann R, Sen B, Blavier J-F. Comparison of Arctic and Antarctic trace gas column abundances from ground-based Fourier transform infrared spectrometry. J Geophys Res 1997;102(D11):12863–9. http://dx.doi.org/10.1029/97JD00358.
[36] Hase F, Demoulin P, Sauval AJ, Toon GC, Bernath PF, Goldman A, et al. An empirical line-by-line model for the infrared solar transmittance spectrum from 700 to 5000 cm^{-1}. J Quant Spectrosc Radiat Transf 2006;102:450–63. http://dx.doi.org/10.1016/j.jqsrt.2006.02.026.
[37] Sudo K, Takahashi M, Kurokawa J, Akimoto H. Chaser: a global chemical model of the troposphere, 1. Model description. J Geophys Res 2002;107(D17):4339. http://dx.doi.org/10.1029/2001JD001113.
[38] Chang L, Palo S, Hagan M, Richter J, Garcia R, Riggin D, Fritts D. Structure of the migrating diurnal tide in the Whole Atmosphere Community Climate Model (WACCM). Adv Space Res 2008;41: 1398–407. http://dx.doi.org/10.1016/j.asr.2007.03.035.
[39] Rodgers CD, Connor BJ. Intercomparison of remote sounding instruments. J Geophys Res 2003;108(D3):4116. http://dx.doi.org/10.1029/2002JD002299.
[40] Pine AS, Lafferty WJ. Torsional splittings and assignments of the Doppler-limited spectrum of ethane in the CH stretching region. J Res Natl Bur Stand 1981;87(3):237–56.
[41] Brown LR, Farmer CB, Rinsland CP, Toth RA. Molecular line parameters for the atmospheric trace molecule spectroscopy experiment. Appl Opt 1987;26(23):5154–82.
[42] Rothman LS, et al. The HITRAN 2004 molecular spectroscopic database. J Quant Spectrosc Radiat Transf 2005;96:139–204, http://dx.doi.org/10.1016/j.jqsrt.2004.10.008.
[43] Rothman LS, et al. The HITRAN 2008 molecular spectroscopic database. J Quant Spectrosc Radiat Transf 2009;110:533–72, http://dx.doi.org/10.1016/j.jqsrt.2009.02.013.
[44] Harrison JJ, Allen NDC, Bernath PF. Infrared absorption cross sections for ethane (C_2H_6) in the 3 μm region. J Quant Spectrosc Radiat Transf 2010;111:357–63. http://dx.doi.org/10.1016/j.jqsrt.2009.09.010.
[45] Lattanzi F, di Lauro C, Vander Auwera F. Toward the understanding of the high resolution infrared spectrum of C_2H_6 near 3.3 μm. J Mol Spec 2011;267(1–2):71–9. http://dx.doi.org/10.1016/j.jms.2011.02.003.
[46] Rothman LS, et al. The HITRAN 2012 molecular spectroscopic database. J Quant Spectrosc Radiat Transf 2013;130:4–50, http://dx.doi.org/10.1016/j.jqsrt.2013.07.002.
[47] Bray C, Perrin A, Jacquemart D, Lacome N. The ν_1, ν_4 and $3\nu_6$ bands of methyl chloride in the 3.4−μm region: line positions and intensities. J Quant Spectrosc Radiat Transf 2011;112:2446–62. http://dx.doi.org/10.1016/j.jqsrt.2011.06.018.
[48] Bray C, Jacquemart D, Buldyreva J, Lacome N, Perrin A. N_2-broadening coefficients of methyl chloride at room temperature. J Quant Spectrosc Radiat Transf 2012;113:1102–12. http://dx.doi.org/10.1016/j.jqsrt.2012.01.028.
[49] Esposito F, Grieco G, Masiello G, Pavese G, Restieri R, Serio C, Cuomo V. Intercomparison of line-parameter spectroscopic databases using downwelling spectral radiance. Q J R Meteorol Soc 2007;133:191–202. http://dx.doi.org/10.1002/qj.131.
[50] Rodgers C. Inverse methods for atmospheric sounding, vol. 2 of Series on Atmospheric, Oceanic and Planetary Physics 2000.
[51] Vigouroux C, Hendrick F, Stavrakou T, Dils B, De Smedt I, Hermans C, et al. Ground-based FTIR and MAX-DOAS observations of formaldehyde at Réunion Island and comparisons with satellite and model data. Atmos Chem Phys 2009;9:9523–44. http://dx.doi.org/10.5194/acp-9-9523-2009.
[52] Rinsland CP, Mahieu E, Demoulin P, Zander R, Servais C, Hartmann J-M. Decrease of the carbon tetrachloride (CCl_4) loading above Jungfraujoch, based on high resolution infrared solar spectra recorded between 1999 and 2011. J Quant Spectrosc Radiat Transf 2012;113:1322–9, http://dx.doi.org/10.1016/j.jqsrt.2012.02.016.
[53] Hase F, Hannigan JW, Coffey MT, Goldman A, Höpfner M, Jones NB, et al. Intercomparison of retrieval codes used for the analysis of high-resolution: ground-based FTIR measurements. J Quant Spectrosc Radiat Transf 2004;87:25–52. http://dx.doi.org/10.1016/j.jqsrt.2003.12.008.
[54] Franco B, Hendrick F, Van Roozendael M, Müller J-F, Stavrakou T, Marais EA, et al. Retrievals of formaldehyde from ground-based FTIR and MAX-DOAS observations at the Jungfraujoch station and comparisons with GEOS-Chem and IMAGES model simulations. Atmos Meas Tech Discuss 2014;7:10715–70. http://dx.doi.org/10.5194/amtd-7-10715-2014.
[55] Sudo K, Akimoto H. Global source attribution of tropospheric ozone: long-range transport from various source regions. J Geophys Res 2007;112(D12302). http://dx.doi.org/10.1029/2006JD007992.
[56] Takemura T, Nozawa T, Emori S, Nakajima TY, Nakajima T. Simulation of climate response to aerosol direct and indirect effects with aerosol transport-radiation model. J Geophys Res 2005;110 (D02202). http://dx.doi.org/10.1029/2004JD005029.

[57] Watanabe S, Hajima T, Sudo K, Nagashima T, Takemura T, Okajima H, et al. MIROC-ESM 2010: model description and basic results of CMIP5-20c3m experiments. Geosci Model Dev 2011;4:845–72, http://dx.doi.org/10.5194/gmd-4-845-2011.

[58] Ito A. Evaluation of the impacts of defoliation by tropical cyclones on a Japanese forest's carbon budget using flux data and a process-based model. J Geophys Res 2010;115(G04013). http://dx.doi.org/10.1029/2010JG001314.

[59] Bey I, Jacob DJ, Yantosca RM, Logan JA, Field BD, Fiore AM, et al. Global modeling of tropospheric chemistry with assimilated meteorology: model description and evaluation. J Geophys Res 2001;106(D19):23073–95. http://dx.doi.org/10.1029/2001JD000807.

[60] Park RJ, Jacob DJ, Field BD, Yantosca RM, Chin M. Natural and transboundary pollution influences on sulfate-nitrate-ammonium aerosols in the United States: implications for policy. J Geophys Res 2004;109(D15204). http://dx.doi.org/10.1029/2003JD004473.

[61] Mao J, Jacob DJ, Evans MJ, Olson JR, Ren X, Brune WH, et al. Chemistry of hydrogen oxide radicals (HO_x) in the Arctic troposphere in spring. Atmos Chem Phys 2010;10:5823–38. http://dx.doi.org/10.5194/acp-10-5823-2010.

[62] Van het Bolscher M, Pereira J, Spessa A, Dalsoren S, van Nojie T, Szopa S. REanalysis of the TROpospheric chemical composition over the past 40 years. Hamburg, Germany: Max Plank Institute for Meteorology; 2008.

[63] Van der Werf GR, Randerson JT, Giglio L, Collatz GJ, Mu M, Kasibhatla PS, et al. Global fire emissions and the contribution of deforestation, savanna, forest, agricultural, and peat fires 1997–2009. Atmos Chem Phys 2010;10:11707–35. http://dx.doi.org/10.5194/acp-10-11707-2010.

[64] Pozzer A, Pollmann J, Taraborrelli D, Jöckel P, Helmig D, Tans P, et al. Observed and simulated global distribution and budget of atmospheric C_2–C_5 alkanes. Atmos Chem Phys 2010;10:4403–22, http://dx.doi.org/10.5194/acp-10-4403-2010.

[65] Ehhalt DH, Schmidt U, Zander R, Demoulin P, Rinsland CP. Seasonal cycle and secular trend of the total and tropospheric column abundance of ethane above the Jungfraujoch. J Geophys Res 1991;96(D3):4985–94. http://dx.doi.org/10.1029/90JD02229.

[66] Simpson IJ, Sulbaek Andersen MP, Meinardi S, Bruhwiler L, Blake NJ, Helmig D, et al. Long-term decline of global atmospheric ethane concentrations and implications for methane. Nature 2012;488:490–4. http://dx.doi.org/10.1038/nature11342.

[67] Zeng G, Wood SW, Morgenstern O, Jones NB, Robinson J, Smale D. Trends and variations in CO, C_2H_6, and HCN in the Southern Hemisphere point to the declining anthropogenic emissions of CO and C_2H_6. Atmos Chem Phys 2012;12:7543–55. http://dx.doi.org/10.5194/acp-12-7543-2012.

[68] Aydin M, Verhulst KR, Saltzman ES, Battle MO, Montzka SA, Blake DR, et al. Recent decreases in fossil-fuel emissions of ethane and methane derived from firn air. Nature 2011;476:198–201, http://dx.doi.org/10.1038/nature10352.

[69] Schneising O, Burrows JP, Dickerson RR, Buchwitz M, Reuter M, Bovensmann H. Remote sensing of fugitive methane emissions from oil and gas production in North American tight geologic formations: remote sensing of fugitive methane emissions from oil and gas production. Earth's Future 2014;2:548–58. http://dx.doi.org/10.1002/2014EF000265.

[70] Bernath PF, McElroy CT, Abrams MC, Boone CD, Butler M, et al. Atmospheric chemistry experiment ACE: mission overview. Geophys Res Lett 2005;32(L15S01). http://dx.doi.org/10.1029/2005GL022386.

[71] Boone CD, Walker KA, Bernath PF. Version 3 retrievals for the atmospheric chemistry experiment fourier transform spectrometer (ACE-FTS), The atmospheric chemistry experiment ACE at 10: a solar occultation anthology. Hampton, Virginia: A. Deepak Publishing; 2013.

[72] Simpson IJ, Rowland FS, Meinardi S, Blake DR. Influence of biomass burning during recent fluctuations in the slow growth of global tropospheric methane. Geophys Res Lett 2006;33(L22808). http://dx.doi.org/10.1029/2006GL027330.

[73] Montzka SA, Krol M, Dlugokencky E, Hall B, Jockel P, Lelieveld J. Small interannual variability of global atmospheric hydroxyl. Science 2011;331:67–9. http://dx.doi.org/10.1126/science.1197640.

[74] Kirschke S, Bousquet P, Ciais P, Saunois M, Canadell JG, et al. Three decades of global methane sources and sinks. Nat Geosci 2013;6:813–23. http://dx.doi.org/10.1038/ngeo1955.

Atmos. Meas. Tech., 8, 1733–1756, 2015
www.atmos-meas-tech.net/8/1733/2015/
doi:10.5194/amt-8-1733-2015

Atmospheric Measurement Techniques
Open Access

Retrievals of formaldehyde from ground-based FTIR and MAX-DOAS observations at the Jungfraujoch station and comparisons with GEOS-Chem and IMAGES model simulations

B. Franco[1], F. Hendrick[2], M. Van Roozendael[2], J.-F. Müller[2], T. Stavrakou[2], E. A. Marais[3], B. Bovy[1], W. Bader[1], C. Fayt[2], C. Hermans[2], B. Lejeune[1], G. Pinardi[2], C. Servais[1], and E. Mahieu[1]

[1]Institute of Astrophysics and Geophysics of the University of Liège, Liège, Belgium
[2]Belgian Institute for Space Aeronomy (BIRA-IASB), Brussels, Belgium
[3]School of Engineering and Applied Sciences, Harvard University, Cambridge, MA, USA

Correspondence to: B. Franco (bruno.franco@ulg.ac.be)

Received: 5 September 2014 – Published in Atmos. Meas. Tech. Discuss.: 23 October 2014
Revised: 25 March 2015 – Accepted: 27 March 2015 – Published: 15 April 2015

Abstract. As an ubiquitous product of the oxidation of many volatile organic compounds (VOCs), formaldehyde (HCHO) plays a key role as a short-lived and reactive intermediate in the atmospheric photo-oxidation pathways leading to the formation of tropospheric ozone and secondary organic aerosols. In this study, HCHO profiles have been successfully retrieved from ground-based Fourier transform infrared (FTIR) solar spectra and UV-visible Multi-AXis Differential Optical Absorption Spectroscopy (MAX-DOAS) scans recorded during the July 2010–December 2012 time period at the Jungfraujoch station (Swiss Alps, 46.5° N, 8.0° E, 3580 m a.s.l.). Analysis of the retrieved products has revealed different vertical sensitivity between both remote sensing techniques. Furthermore, HCHO amounts simulated by two state-of-the-art chemical transport models (CTMs), GEOS-Chem and IMAGES v2, have been compared to FTIR total columns and MAX-DOAS 3.6–8 km partial columns, accounting for the respective vertical resolution of each ground-based instrument. Using the CTM outputs as the intermediate, FTIR and MAX-DOAS retrievals have shown consistent seasonal modulations of HCHO throughout the investigated period, characterized by summertime maximum and wintertime minimum. Such comparisons have also highlighted that FTIR and MAX-DOAS provide complementary products for the HCHO retrieval above the Jungfraujoch station. Finally, tests have revealed that the updated IR parameters from the HITRAN 2012 database have a cumulative effect and significantly decrease the retrieved HCHO columns with respect to the use of the HITRAN 2008 compilation.

1 Introduction

Formaldehyde (HCHO) is the most abundant organic carbonyl compound in the remote troposphere (Hak et al., 2005, and references therein). Being predominantly a high-yield product of oxidation by hydroxyl radicals (OH) of most of the primary volatile organic compounds (VOCs) emitted either naturally or by human activities, HCHO is ubiquitous throughout the atmosphere. It is also directly emitted in a small fraction from biogenic (e.g., vegetation), pyrogenic (mainly biomass burning) and anthropogenic (e.g., industrial emissions) sources (e.g., Carlier et al., 1986; Lee et al., 1997; Hak et al., 2005; Herndon et al., 2005; Fu et al., 2007; De Smedt et al., 2010). Long-lived VOCs such as methane (CH_4) contribute to the background levels of HCHO. However, the spatial variability of HCHO concentration is primarily associated with the oxidation of reactive non-methane VOCs of biogenic (e.g., isoprene) or anthropogenic (e.g., butane) origin. At low nitric oxide (NO) concentrations, intermediate compounds such as methyl hydroperoxide (CH_3OOH) are formed which are partly removed by deposition, thereby reducing HCHO formation.

Formaldehyde has a very short midday lifetime on the order of a few hours (Logan et al., 1981; Possanzini et al.,

2002). Its main removal pathways take place by photolysis and oxidation by OH radicals, with both loss processes yielding carbon monoxide (CO) and hydroperoxyl radicals (HO_2), so that HCHO affects the global CO budget and the oxidative capacity of the atmosphere. Losses of HCHO by dry and wet deposition near the surface are generally less significant (Atkinson, 2000). Moreover, HCHO is an important intermediate in the VOC–HO_x (hydrogen oxides)–NO_x (nitrogen oxides) chemistry (Houweling et al., 1998; Hak et al., 2005; Kanakidou et al., 2005), making it a key component in the global catalytic cycle responsible for generating or destroying tropospheric ozone (O_3), depending on the NO_x levels (Fried et al., 1997; Lee et al., 1998; Tan et al., 2001).

Recently, total FTIR (Fourier transform infrared) and partial UV-visible MAX-DOAS (Multi-AXis Differential Optical Absorption Spectroscopy) columns of HCHO derived from ground-based remote sensing measurements have been used to evaluate HCHO observations obtained from SCIAMACHY (SCanning Imaging Absorption spectroMeter for Atmospheric CHartographY), GOME (Global Ozone Monitoring Experiment) and ACE-FTS (Atmospheric Chemistry Experiment Fourier transform spectrometer) space-based sensors (e.g., Wittrock et al., 2006; Jones et al., 2009; Vigouroux et al., 2009; Viatte et al., 2014). Such studies reported an overall consistency between satellite HCHO observations and ground-based FTIR and MAX-DOAS measurements at a number of sites influenced by biomass burning (Wittrock et al., 2006; Jones et al., 2009; Vigouroux et al., 2009) or urban sources of pollution (Wittrock et al., 2006). In addition, Vigouroux et al. (2009) successfully compared FTIR and MAX-DOAS observations, HCHO columns from SCIAMACHY nadir satellite and simulations by the global CTM (chemistry transport model) IMAGES v2 (Intermediate Model of Annual and Global Evolution of Species) at Reunion Island (20.9° S, 55.5° E).

In this study, we report parallel HCHO measurements performed at the high-altitude research station of Jungfraujoch (Swiss Alps), part of the NDACC (Network for the Detection of Atmospheric Climate Change; see http://www.ndacc.org), using both ground-based high-resolution FTIR and MAX-DOAS instruments. This work presents the first intercomparison of ground-based FTIR and MAX-DOAS HCHO observations carried out at a high-altitude, dry and weakly polluted site (Zander et al., 2008). The Jungfraujoch station contrasts with, e.g., the sea-level Reunion Island site where HCHO total columns are influenced by large precursor emissions originating from biogenic and pyrogenic sources in southern Africa and Madagascar (Vigouroux et al., 2009). The combination of elevation, weakly polluted conditions and the strong vertical gradient of HCHO concentration in the lower troposphere contributes to reducing the solar infrared absorption of HCHO at the Jungfraujoch station and makes it very challenging to retrieve.

FTIR and MAX-DOAS measurements are not directly comparable given their respective vertical resolution and sensitivity, but with this work we show that both techniques are essentially complementary for HCHO retrieval above Jungfraujoch. Therefore we use two state-of-the art three-dimensional global CTMs, GEOS-Chem (v9-01-03; Bey et al., 2001) and IMAGES v2 (Stavrakou et al., 2013), for intercomparing FTIR total columns and MAX-DOAS partial columns of HCHO over the entire July 2010–December 2012 time period. The HCHO columns and concentrations simulated by the CTMs are compared successively to the ground-based data sets, taking into account the vertical sensitivity of each remote sensing instrument by applying their respective averaging kernels.

This work also aims at implementing and validating an optimized FTIR retrieval strategy for HCHO above Jungfraujoch as a preparation for further studies. Indeed, it is worth mentioning that FTIR solar spectra exploitable for the retrieval of HCHO are actually available at the Jungfraujoch station since the beginning of 1988. Using the FTIR retrieval strategy implemented and validated in the present study, all these solar spectra spanning the 1988–2014 time period are currently being processed in an ongoing work in order to produce long-term record of HCHO and investigate its interannual variability above Jungfraujoch. Finally, ground-based HCHO measurements are increasingly required to validate satellite observations such as SCIAMACHY, GOME, ACE-FTS and TROPOMI (TROPOspheric Monitoring Instrument).

The measurement site, instrumental setups, investigated data sets and ground-based retrieval strategies for the Jungfraujoch station are described in Sect. 2. A short description of the GEOS-Chem and IMAGES models as well as of the simulations performed in the framework of this study is also given in Sect. 2. Section 3 presents the characterization of the FTIR and MAX-DOAS geophysical products, including a detailed error budget for each ground-based data set. Section 4 reports the results of the HCHO retrievals above Jungfraujoch as well as the comparisons between FTIR and MAX-DOAS columns and model simulations. Concluding remarks and perspectives are included in Sect. 5.

2 Instrumental setup and data sets

2.1 Measurement site

The high-alpine international scientific station of Jungfraujoch (referred to below as ISSJ, 46.5° N, 8.0° E, 3580 m a.s.l.; Zander et al., 2008), is located on a mountain saddle between the two summits Jungfrau (4158 m a.s.l.) and Mönch (4099 m a.s.l.) on the northern edge of the Swiss Alps. Due to its particular topographical position representing a strong barrier for synoptic-scale air flow, the ISSJ is mainly influenced by northwesterly winds, advecting air masses to the ISSJ from the Swiss plateau, and southeasterly flows from the inner Alpine region and the south of the Alps (e.g., the Po Valley, Italy). Because of its altitude, the ISSJ is essen-

tially located in the free troposphere in winter (from November to January) and is influenced by advective weather types (Collaud Coen et al., 2011). During the rest of the year, frequent injections of air masses from the planetary boundary layer (PBL) occur, especially in summer where convective weather types have a greater occurrence (Collaud Coen et al., 2011). Therefore the ISSJ often allows investigation of the atmospheric background conditions over central Europe as well as studying the mixing of PBL and free tropospheric air masses (e.g., Zellweger et al., 2003; Reimann et al., 2004).

As glaciers and barren rocks cover the main area in the closest vicinity of the ISSJ, contamination due to local HCHO precursor emissions is generally negligible. However, analyses of backward trajectories for background conditions indicated that the air masses at Jungfraujoch have a large contribution of biogenic and anthropogenic emissions from western central Europe, i.e., northern Italy, southern France and southern and eastern Germany (Legreid et al., 2008). They also revealed that the influence of long-range intercontinental transport is discernible, clearly separated from the influence of the European PBL (Henne et al., 2005; Balzani Lööv et al., 2008). Influences from large biogenic and anthropogenic emission sources generally originate from the nearby valleys, such as the Rhône Valley to the south of Jungfraujoch or the Po Valley in northern Italy, and from cities at the foothill of the Alps. These pollutant emissions might be transported to Jungfraujoch by air advection in the upper PBL, thermally driven convection, front passage and efficient tropospheric venting of PBL air masses from deep Alpine valleys, especially during summertime (Lugauer et al., 2000; Henne et al., 2004, 2005; Li et al., 2005). The constituents lifted to the ISSJ are then transported horizontally by the synoptic flow over the Alpine region.

2.2 FTIR observations and retrieval strategy

The FTIR data set investigated in this work has been derived from solar spectra recorded under clear-sky conditions at ISSJ with a high spectral resolution commercial Bruker IFS 120 HR spectrometer equipped with indium antimonide and mercury cadmium telluride cooled detectors (we refer to Zander et al., 2008, for further details). It consists of a subset of 1500 spectra (representing 326 days of observations) recorded during the July 2010–December 2012 period with an optical filter covering the 2400–3310 cm^{-1} spectral domain and maximizing the signal-to-noise (S/N) ratio. This data set has been limited such as to coincide with the observational time of the MAX-DOAS instrument (see following Sect. 2.3). It is characterized by a typical spectral resolution (defined here as the inverse of twice the maximum optical path difference) alternating between 0.003 and 0.005 cm^{-1} and by S/N ratios ranging from about 550 to 3100, the highest values being reached for averages of consecutive individual spectra.

All FTIR solar observations have been fitted with the SFIT-2 v3.91 algorithm (Rinsland et al., 1998) based on the optimal estimation formalism of Rodgers (2000). This code performs the derivation of vertical mixing ratio profiles and corresponding column abundances of most of the FTIR target gases and allows the characterization of the vertical information content of the measurement. The model atmosphere above the ISSJ is discretized in a 39-layer scheme of progressively increasing thicknesses (until 100 km altitude), using physical pressure and temperature information derived on a daily basis from midday pressure–temperature profiles provided by the National Centers for Environmental Prediction (NCEP, http://www.ncep.noaa.gov). Spectroscopic line parameters from the HITRAN 2008 official release (Rothman et al., 2009) are assumed in the spectral fitting process, including the additional line strength updates for HCHO from Perrin et al. (2009).

The a priori vertical concentration profile for HCHO, as well as for all interfering species in the retrieval process, originates from averaged volume mixing ratio (VMR) profiles derived from WACCM v6 (Whole Atmosphere Community Climate Model; see e.g., Chang et al., 2008) simulations above ISSJ over the 1980–2020 period. This a priori VMR profile for HCHO (see Fig. S1 in the Supplement) presents a good consistency with the zonal average of individual HCHO profiles derived from nearly 2000 occultation observations performed between 36.5 and 56.5° N and over the 2004–2012 period by the ACE-FTS instrument version 3.5 (Bernath et al., 2005; Dufour et al., 2009a) within the entire altitude range accessible by ACE-FTS (i.e., from approximately 6 to 40 km for HCHO). The concentration of the simulated HCHO profiles shows a strong gradient in the troposphere, with maximum values of approximately 0.3 ppbv at the ISSJ altitude (3580 m), rapidly decreasing to a minimum of 10 pptv in the upper troposphere and the lower stratosphere. These values are in good agreement with in situ observations (e.g., Harder et al., 1997) and airborne measurements (e.g., Fried et al., 2003, 2008; Stickler et al., 2006) carried out in the background continental boundary layer at mid-latitudes in the Northern Hemisphere.

Solar absorption by HCHO in the infrared domain results in very broad spectral features of very weak intensities, especially at ISSJ (generally less than 1 % of the total signal under normal background conditions) because of the station elevation and dominant non-polluted air masses. The FTIR retrieval strategy implemented in this study is based on the method developed by Vigouroux et al. (2009) for the HCHO retrieval at Reunion Island, who used six microwindows encompassing the 2760–2860 cm^{-1} spectral domain. The selection of these fitting spectral intervals is discussed in Vigouroux et al. (2009). In the present work, we use four of these microwindows (see Table 1), discarding two due to the presence of systematic residuals or of very strong interferences blinding the weak HCHO absorption. A typical example of FTIR fit for HCHO at Jungfraujoch is presented in

Table 1. List of the microwindows used for the FTIR retrieval of HCHO and the interfering species. The 2765 and 2855 cm^{-1} microwindows are used in a first run to pre-fit HCHO, HDO and O_3 by simple scaling. The scaled profiles of these three compounds are then used as a priori profiles in the retrievals of HCHO.

Microwindows (cm^{-1})	Interfering species
2763.425–2763.600	HDO, CH_4, O_3, N_2O, CO_2
2765.725–2765.975	HDO, CH_4, O_3, N_2O, CO_2
2778.200–2778.590	HDO, CH_4, O_3, N_2O, CO_2
2855.650–2856.400	HDO, CH_4, O_3, N_2O, H_2O

Fig. 1, as well as the simulated HCHO absorption in these four microwindows. The same example of FTIR fit, but using the same six microwindows as Vigouroux et al. (2009), is illustrated in Fig. S2 in the Supplement. The interfering species are CH_4 producing the background absorption in every interval, multiple lines of O_3 and individual features of N_2O, CO_2, HDO and H_2O. The 2763 and 2765 cm^{-1} microwindows are mainly characterized by relatively weak interfering absorptions, the larger HCHO absorption occurring in the 2778 cm^{-1} microwindow. The last interval presents small absorptions of HCHO at approximately 2856.2 cm^{-1} but encompasses two large features of HDO and solar absorption very helpful in reducing the correlation between HCHO signals and both HDO and solar absorptions in the other microwindows.

Instead of a Tikhonov type L1 regularization as used by Vigouroux et al. (2009) for the HCHO retrieval process, we have opted for an optimal estimation method (OEM; Rodgers, 2000) accounting for the geophysical conditions of the target species. As the covariance matrix should represent the natural variability of HCHO for each atmospheric layer, we have determined the value of each diagonal element (i.e., a percentage of the a priori profile) by investigating the variability profile of HCHO on the basis of the solar occultation observations from ACE-FTS v3.5 and simulations of the WACCM model. The averaged relative standard deviations (RSD) of HCHO VMR from ACE-FTS and WACCM present very consistent vertical shapes above ISSJ, indicating a maximum of variability at 10 km altitude. However, the entire WACCM profile has to be multiplied by a constant factor of approximately 2.5 to approach the values derived from the ACE-FTS observations. Such a difference between the RSD ensembles can be explained by the fact that the model probably underestimates the atmospheric natural variability of HCHO and that the measurement noise inherent to the ACE-FTS observations presumably induces excessive RSD values. However, adoption of a variability profile derived from ACE-FTS RSD values was found to lead to strong oscillations in the retrieved tropospheric profiles. Such oscillations are responsible for unphysical negative VMR values of HCHO. Consequently, the diagonal elements of the covariance matrix have been adjusted to obtain a compromise between stability and information content. Through several tests we have determined an adequate factor of 1.5 to multiply the RSD profile from WACCM and have adopted these values as diagonal elements of the covariance matrix. The HCHO variability (see Fig. S1) at the ISSJ altitude amounts to 65 %, slightly decreases to 55 % at 6 km altitude and reaches its maximum (approximately 100 %) at 10–11 km before rapidly decreasing with the elevation. Given the strong gradient of HCHO concentration in the troposphere, we have used a Gaussian inter-layer correlation with a half-width length of 3 km for the off-diagonal elements of the covariance matrix. Finally, a S/N ratio of 600 for inversion is set in all fitting sequences, consistent with the noise level of most of the analyzed solar spectra.

In the present study, the fitting process of an individual FTIR solar spectrum to retrieve HCHO at ISSJ consists of two successive steps. In the first one, which is a pre-fitting step, the a priori VMR profiles of HCHO, HDO and O_3 provided by the WACCM model are independently scaled in the 2765.725–2765.975 and 2855.650–2856.400 cm^{-1} microwindows only (without taking into account the other interfering compounds in these microwindows), using a single parameter for each scaled species. These spectrum-specific scaled profiles are then used as a priori for HCHO, HDO and O_3 in the HCHO retrieval process by the OEM (i.e., the second step) involving the four microwindows and all the interfering species listed in Table 1. During this second step, the vertical distribution of each interfering species is independently varied over their entire altitude spans. The pre-fit (i.e., scaling) of the HCHO a priori in the first step helps to avoid strong oscillations during the retrieval process by the OEM in the second step and the related unphysical profiles that may be produced.

2.3 MAX-DOAS observations and retrieval strategy

The ground-based passive MAX-DOAS technique has already been applied to the HCHO detection (e.g., Heckel et al., 2005; Irie et al., 2011; Wagner et al., 2011; Pinardi et al., 2013), revealing a good consistency with HCHO observations from SCIAMACHY nadir viewing satellite (Wittrock et al., 2006), LP (long-path) DOAS instrument (Pikelnaya et al., 2007), PTR-MS (proton transfer reaction mass spectrometry) data (Inomata et al., 2008) and during the airborne INTEX-B (INtercontinental chemical Transport Experiment) campaign (Fried et al., 2011).

A MAX-DOAS spectrometer designed and assembled at the Belgian Institute for Space Aeronomy has been operating at ISSJ since July 2010. A detailed explanation of the instrument is provided in Clémer et al. (2010), Hendrick et al. (2014) and Wang et al. (2014). In brief, it is a dual-channel system composed of two grating spectrometers covering the UV (300–390 nm) and visible (400–580 nm here instead of 400–720 nm for our instrument operating in China; see the

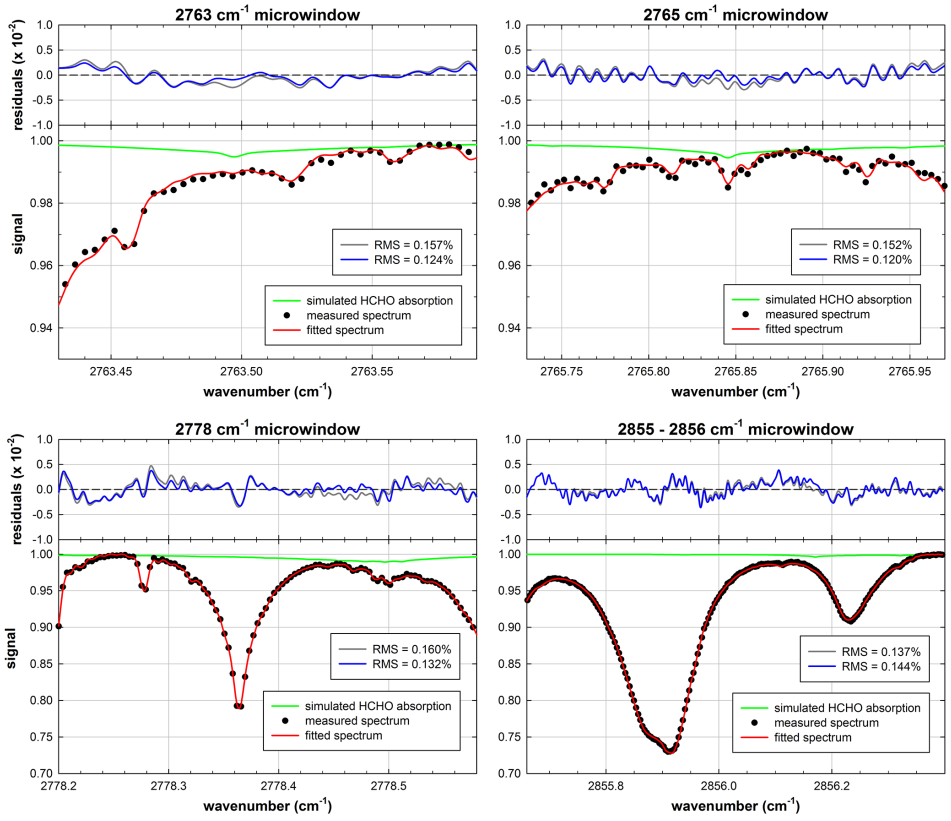

Figure 1. Typical example of HCHO FTIR spectral fits at ISSJ: 22 August 2010, 06:40 UTC, with a SZA of 80°. The related residuals when fitting HCHO absorption and assuming no HCHO absorption are in blue and grey curves, respectively. This solar spectrum is characterized by a S/N ratio of 1656 and produced a DOFS equal to 1.02 and HCHO total column of 1.26×10^{15} molec cm^{-2} (compared to a S/N ratio of 1627, a DOFS of 1.05 and HCHO total column of 1.56×10^{15} molec cm^{-2} averaged over the whole FTIR July 2010–December 2012 data set). The solid green line corresponds the HCHO solar absorption simulated at the ISSJ for the same date and SZA. Note that this FTIR fit corresponds to the same date as the DOAS fit example in Fig. 2. This figure can be compared to Fig. S2, representing the same HCHO FTIR spectral fits but using the six microwindows from Vigouroux et al. (2009).

three references here above) wavelength ranges and connected to cooled CCD detectors. The instrumental function is close to a Gaussian with a full width at half maximum of 0.4 and 0.5 nm in the UV and visible, respectively. The optical head is mounted on a commercial sun tracker (INTRA, Brusag) and is linked to the spectrometers through optical fibers. The instrument is pointing towards the city of Bern (northwest direction) and a full MAX-DOAS scan consists of the following elevation angles: −10, −8, −6, −4, −2, 0, 1, 3, 4, 5, 8, 10, 15, 30 and 90° (zenith). The negative elevations, i.e., when the instrument points downwards the valley, as well as azimuthal scans performed around local noon were not used in the present study.

The data set investigated here covers the July 2010–December 2012 time period. The retrieval of HCHO vertical profiles and corresponding column amounts is performed in two steps: (1) DOAS spectral fitting providing the so-called differential slant column densities (DSCDs) and (2) application of an OEM-based profiling method on the HCHO DSCDs to retrieve vertical profiles. These two steps are described below.

2.3.1 DOAS analysis

Measured scattered-sunlight spectra are analyzed using the QDOAS spectral fitting software suite (http://uv-vis.aeronomie.be/software/QDOAS/). The principle of the DOAS technique is to separate high-frequency molecular absorption features from a broadband component accounting for scattering and instrumental effects (Platt and Stutz, 2008). The DOAS spectral fitting yields DSCDs, which are expressed in molec cm^{-2} and correspond to the concentration of a given absorber integrated along the effective light path relative to the amount of the same absorber in a measured reference spectrum. In the case of MAX-DOAS, the zenith spectrum of each scan is often taken as reference in order to remove the stratospheric contribution in off-axis measurements (Hönniger et al., 2004).

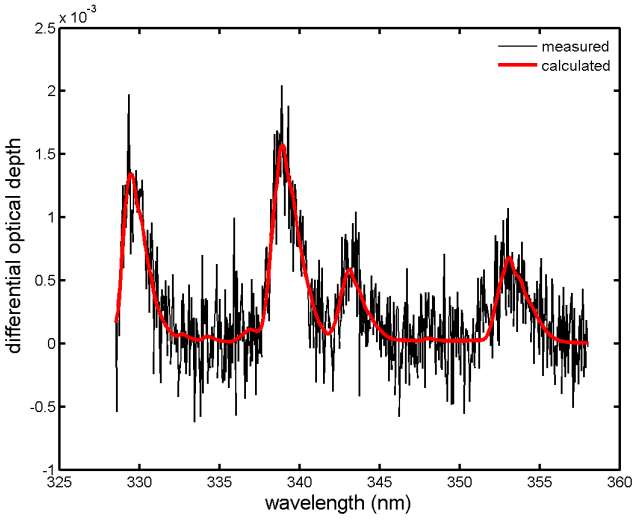

Figure 2. Example of HCHO DOAS fit at ISSJ. It corresponds to 22 August 2010 (the same date as the FTIR fit example presented in Fig. 1) at 16:30 UTC and 0° elevation.

HCHO DSCDs are retrieved in the 328.5–358.0 nm wavelength range. Compared to previously published HCHO DOAS settings (Vigouroux et al., 2009; Pinardi et al., 2013), the fitting interval is extended here towards the UV for minimizing the HCHO/BrO correlation. The zenith spectrum of each scan is used as reference, leading to a reduction of the interference by O_3 and of the impact of possible instrumental degradation. ISSJ, being a remote station, has low HCHO content and as a result these two settings are found to significantly improve the DOAS fit. The following spectral signatures are taken into account: HCHO at 293 K (Meller and Moortgat, 2000), NO_2 at 298 K (Vandaele et al., 1998), O_3 at 223 K and 243 K (Bogumil et al., 2003) plus additional correction terms according to Puķīte et al. (2010), O_4 (Thalman and Volkamer, 2013), BrO at 223 K (Fleischmann et al., 2004) and the Ring effect (Grainger and Ring, 1962; Chance and Spurr, 1997). A fifth-order polynomial is included to fit the broadband structure (Pinardi et al., 2013) and a linear correction for the intensity off-set is used. A typical example of a DOAS fit for HCHO at ISSJ is shown in Fig. 2 (for the same date as the FTIR fit example in Fig. 1).

2.3.2 Profile retrieval

HCHO vertical profiles are retrieved by applying the OEM-based profiling tool bePRO to the HCHO DSCDs. Since bePRO is already described in several papers (Clémer et al., 2010; Hendrick et al., 2014; Wang et al., 2014), only the main features are given here. This application uses a two-step approach for trace gas profile retrieval. First, aerosol extinction profiles are retrieved for each scan from measured O_4 DSCDs (Frieß et al., 2006; Clémer et al., 2010). This step is needed since aerosols significantly affect the effective light path through the atmosphere (Wagner et al., 2004) and therefore the optical density of trace gases. Secondly, HCHO vertical profiles are inverted from the measured HCHO DSCDs using the aerosol extinction profiles obtained in the first step as input for the calculation of the so-called weighting functions $\mathbf{K}$ which describe the relation between the measured DSCDs and vertical profiles. These are calculated using the LIDORT radiative transfer model (Spurr et al., 2008) as the forward model.

Other key parameters in the OEM are the a priori profile $\boldsymbol{x}_a$, its covariance matrix $\mathbf{S}_a$ and the measurement uncertainty covariance matrix $\mathbf{S}_\varepsilon$. For HCHO, the same a priori vertical profile as for FTIR is used, i.e., the HCHO profile derived from WACCM model simulations over the 1980–2020 time period above ISSJ. In the case of the a priori for aerosol retrieval, an extinction profile corresponding to rural conditions with a visibility of 70 km is selected from the LOWTRAN climatology (Shettle, 1989). Due to the absence of AERONET data at ISSJ, aerosol single scattering albedo and phase function at 340 nm are estimated off-line based on a first approximation on the aerosol size distribution and refractive index retrieved from AERONET data at Observatoire de Haute-Provence (44° N, 5.5° E, 600 m a.s.l.) station. $\mathbf{S}_\varepsilon$ and $\mathbf{S}_a$ matrices for both aerosols and HCHO are constructed as in Clémer et al. (2010; see also Hendrick et al., 2014; Wang et al., 2014). For $\mathbf{S}_a$, the diagonal element corresponding to the lowest layer, $\mathbf{S}_a(1,1)$, is set equal to the square of a scaling factor β times the maximum partial aerosol optical depth or vertical column density (VCD) of the profiles. Here $\beta = 0.6$ for HCHO and 0.4 for aerosol. The other diagonal elements decrease linearly with altitude down to $0.2 \times \mathbf{S}_a(1,1)$. The off-diagonal terms in $\mathbf{S}_a$ are set using Gaussian functions with a correlation length of 0.2 km for both HCHO and aerosol retrievals. $\mathbf{S}_\varepsilon$ is a diagonal matrix, with variances equal to the square of the DOAS fitting error. US Standard Atmosphere pressure and temperature profiles and a surface albedo of 0.2 are used and the following altitude grid is selected: 10 layers of 200 m thickness between 3.6 and 6 km and one layer of 2 km between 6 and 8 km.

Each retrieval is quality-checked based on the DOFS (degree of freedom for signal, which corresponds to trace of the averaging kernel matrix $\mathbf{A}$; see also Sect. 3.1) and the relative root mean square error (RMS) between measured and calculated DSCDs. This RMS corresponds to the standard RMS expressed in molec cm^{-2} divided by the mean DSCD of the scan. The following criteria have been chosen for the selection of good scans: DOFS > 1, RMS $< 30\,\%$ and no negative concentration/extinction coefficient values allowed. Since HCHO and aerosol contents are particularly low at ISSJ, their retrieval can be strongly affected by the presence of clouds. The cloud screening method developed by Gielen et al. (2014) and based on the measured color index (CI) at zenith has been therefore utilized as an additional selection criterion. This empirical parameter gives information about the color of the sky: from blue during clear skies

to white/grey when clouds or aerosols are present. Based on the comparison between measured and simulated CI, the following sky conditions can be defined for each MAX-DOAS scan: clear-sky, thin (white/light grey) clouds/polluted, thick (dark grey) clouds/heavily polluted and broken clouds. In the present study, MAX-DOAS scans corresponding to thick clouds or broken clouds are rejected since the quality of the aerosol and trace gas retrievals can be potentially strongly affected by these sky conditions.

2.4 GEOS-Chem simulations

The global GEOS-Chem CTM (version 9-01-03: http://acmg.seas.harvard.edu/geos/doc/archive/man.v9-01-03/index.html) is driven by NASA Global Modeling Assimilation Office GEOS-5 assimilated meteorological fields. The GEOS-5 data are at a native horizontal resolution of $0.5 \times 0.667°$ with 72 vertical levels at 6 h temporal frequency (3 h for surface variables and mixing depths). We use the GEOS-5 data at $2 \times 2.5°$ and 47 vertical levels, combining levels above ~ 80 hPa. GEOS-Chem includes detailed O_3–NO_x–VOC–aerosol coupled chemistry originally described by Bey et al. (2001) and Park et al. (2004) with updates by Mao et al. (2010). The model simulates the distributions of 95 species and chemistry of 22 precursor non-methane VOCs (NMVOCs). The isoprene oxidation mechanism is described in Mao et al. (2013).

Global biogenic emissions are obtained with the Model of Emissions of Gases and Aerosols from Nature (MEGAN) v2.0 (Guenther et al., 2006) and biomass burning emissions are from the Global Fire Emission Database (GFED) v3 (van der Werf et al., 2010). Over Europe, anthropogenic emissions of CO, NO_x, SO_x and NH_3 are provided by the European Monitoring and Evaluation Programme (EMEP; http://www.ceip.at/) regional inventory (Simpson et al., 2010) for the year 2010. GEOS-Chem uses the RETRO emission inventory (Schultz et al., 2007) for base year 2000 for all anthropogenic NMVOC emissions other than methyl ethyl ketone, acetaldehyde, propene and $>= C_4$ alkanes, which are provided by the EMEP inventory. These anthropogenic emissions are scaled to the years of interest using energy statistics (van Donkelaar et al., 2008). An offline simulation is used for anthropogenic ethane emissions (Xiao et al., 2008). Annual average CH_4 concentrations prescribed over four latitude bands (0–30°; 30–90°) are informed by CH_4 measurements from the NOAA Global Monitoring Division flask measurements.

We use GEOS-Chem results for the common observation period (July 2010–December 2012) after 1 year of spin-up for chemical initialization. The GEOS-Chem data set used in the present work consists of HCHO VMR profiles simulated at the closest pixel to the ISSJ and saved at a 3 h time step.

2.5 IMAGES simulations

IMAGES v2 is a global CTM simulating the distributions of 132 trace compounds at a resolution of $2 \times 2.5°$ and at 40 hybrid pressure–sigma levels between the Earth's surface and the lower stratosphere (Stavrakou et al., 2009a, b, 2013). The model includes the chemistry of 22 precursor NMVOCs. The isoprene oxidation mechanism follows the LIM0 scheme (Peeters and Müller, 2010) with revised reaction rates from the updated theoretical estimation of Peeters et al. (2014). Accounting for the isomerization of isoprene peroxy radicals reduces the yields of HCHO by about 10 % in most atmospheric conditions (Stavrakou et al., 2014).

Meteorological fields are obtained from ERA-Interim analyses of the European Center Medium-Range Weather Forecasts (ECMWF). The parameterizations for deep convection and turbulent mixing in the boundary layer use the ERA-Interim updraft mass fluxes and turbulent diffusion coefficients for heat. The model time step is taken equal to 4 h. As described in more detail in Stavrakou et al. (2009b), the effects of diurnal variations are accounted for through correction factors calculated from a detailed model run with a 20 min time step. This diurnal cycle simulation accounts for diurnal variation in the photolysis rates, meteorological parameters and emissions.

The model uses anthropogenic emissions of CO, NO_x, SO_x and NH_3 over Europe from EMEP for the year 2010 and anthropogenic emissions of NMVOCs from the RETRO inventory for the year 2000 (Schultz et al., 2007). It is worth noting that RETRO NMVOC emissions appear to be largely overestimated compared to EMEP estimates: for example, total emissions between 40 and 60° N and between 10° W and 60° E are 25.7 Tg in RETRO and only 10.3 Tg in EMEP for 2011. The seasonal variation of anthropogenic emissions is estimated as in Stavrakou et al. (2013). Diurnal and weekly profiles of CO, NO_x and VOC anthropogenic emissions for OECD countries are obtained from Jenkin et al. (2000). Biomass burning emissions are provided by GFED v3 (van der Werf et al., 2010). Isoprene biogenic emissions are obtained from the MEGAN–MOHYCAN inventory (Stavrakou et al., 2014), whereas methanol biogenic emissions are obtained from an inversion of emissions based on IASI (Infrared Atmospheric Sounding Interferometer) satellite data (Stavrakou et al., 2011). The calculation of inorganic species and aerosols is described in Stavrakou et al. (2013). Monthly latitude-dependent CH_4 concentration profiles constructed from NOAA Global Monitoring Division measurements are used to specify both the initial conditions and the surface boundary conditions for this compound in the model.

The IMAGES data set used in the present work consists of HCHO VMR profiles simulated at the closest pixel to the station and saved at a 4 h time step.

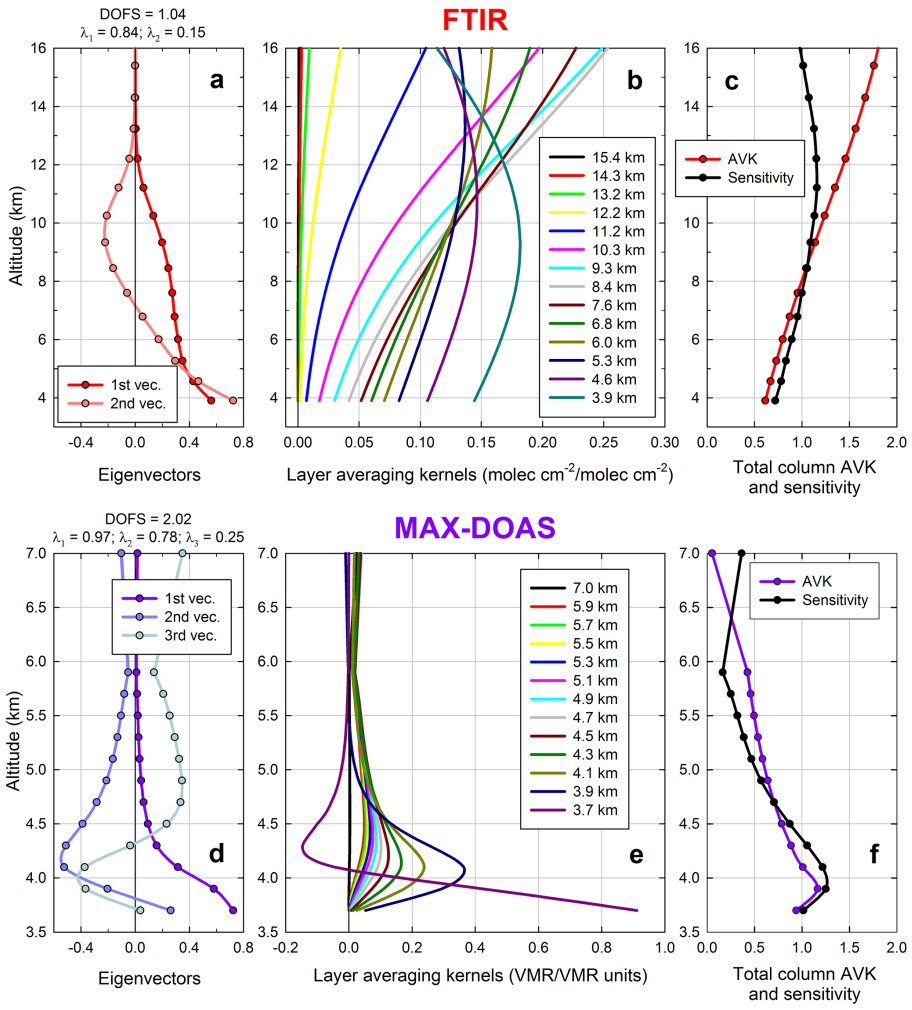

Figure 3. First eigenvectors and the associated eigenvalues (**a** and **d**), layer averaging kernels (**b** and **e**) and total column averaging kernel (AVK) and sensitivity profile (**c** and **f**) characterizing the FTIR (upper frames) and MAX-DOAS (lower frames) retrievals of HCHO above Jungfraujoch. Note that the layer averaging kernels are expressed in molec cm^{-2} (molec cm^{-2})$^{-1}$ for FTIR and in VMR/VMR units for MAX-DOAS. These information parameters have been calculated on the basis of all the individual profiles retrieved over the July 2010–December 2012 time period.

3 Characterization of remote sensing data and error budgets

3.1 Characterization of the FTIR and MAX-DOAS retrievals

In the ill-posed inversion problem determining the retrieved vertical distribution $\boldsymbol{x}_r$ of a target absorber along the vertical (z) in the atmosphere, $\boldsymbol{x}_a$ and $\boldsymbol{x}_t$ are the a priori and true vertical profiles of the target absorber, respectively, and $\mathbf{A}$ is the averaging kernel matrix (i.e., the product of the retrieval process) describing how the retrieved profile is related to $\boldsymbol{x}_a$ and $\boldsymbol{x}_t$ according to Eq. (1) and characterizing the information content of the retrievals.

$$\boldsymbol{x}_r(z) = \boldsymbol{x}_a + \mathbf{A}(\boldsymbol{x}_t - \boldsymbol{x}_a) \quad (1)$$

The typical layer averaging kernels in the troposphere, corresponding to the mean averaging kernels calculated on the basis of the 2010–2012 individual profiles and obtained from the FTIR and MAX-DOAS HCHO retrievals, are drawn in Fig. 3. They are expressed in molec cm^{-2} (molec cm^{-2})$^{-1}$ for FTIR (Fig. 3b) and in VMR/VMR units for MAX-DOAS (Fig. 3e). Corresponding eigenvectors and leading eigenvalues are represented in Fig. 3a and d for FTIR and MAX-DOAS, respectively.

Regarding FTIR, the mean DOFS is 1.04 with a 1σ standard deviation (SD) of 0.3 (including all measurements at different SZA). The DOFS value and the eigenvectors indicate that the FTIR averaging kernels are not vertically resolved and that the retrieved profiles are sensitive only to a change in the true profile $\boldsymbol{x}_t$ between the ISSJ elevation and 12 km altitude. Within this altitude range, the total col-

umn averaging kernel and the sensitivity profile (see Fig. 3c), indicating the fraction of the retrievals originating from the measurements rather than from the a priori information ($\boldsymbol{x}_a$), show values relatively close to 1.0, meaning that most of the information is coming from the measurements. The total column averaging kernel and the corresponding sensitivity profile displayed in Fig. 3c are consistent with those shown in Viatte et al. (2014). On average over all the individual FTIR retrieved profiles, the HCHO column below 12 km altitude represents 95.4 % of the total column.

In contrast to FTIR, two independent pieces of information in the troposphere (mean DOFS = 2.02) may be obtained from the MAX-DOAS measurements. According to the eigenvector decomposition (Fig. 3d), the averaging kernels (Fig. 3e) and the column averaging kernel and sensitivity (Fig. 3f), most of the information on the vertical distribution of HCHO contained in the measurements is located below 5.5 km altitude, with a maximum sensitivity in the lowest layers close to the ground. The first eigenvector is found to be mainly responsible for the strong sensitivity in the lowermost layer, with 97 % of the information content independent from the a priori profile ($\boldsymbol{x}_a$). The following eigenvectors mainly contribute to increasing the sensitivity of the retrievals at upper levels in the troposphere. Nevertheless, the contribution of the MAX-DOAS retrievals to the information content is rapidly decreasing with the elevation (e.g., this contribution is reduced to 50 % approximately at 5 km altitude). These results show that the concentration in the lowest layer (3.6–3.8 km) in addition to the 3.6–8 km partial column can be retrieved from the MAX-DOAS observations at ISSJ. However, the discussion will be mainly focused on the 3.6–8 km partial columns in the present study.

It can be concluded that the FTIR and MAX-DOAS retrievals have a different vertical resolution and sensitivity to the vertical distribution of HCHO, with the former being vertically unresolved and mainly sensitive in the free troposphere up to the tropopause and the latter characterizing the HCHO abundance in the lower vertical layers in the vicinity of the ISSJ. Therefore, direct comparisons of retrieved HCHO abundances from both techniques have little meaning, but ground-based FTIR and MAX-DOAS observations provide complementary information on the HCHO distribution in the atmosphere, more specifically in the lowermost troposphere (see Fig. S3). Nevertheless, we will use simulated HCHO distributions of two three-dimensional CTMs (GEOS-Chem and IMAGES) as intermediates to investigate the consistency between the retrieved HCHO columns (e.g., the seasonal cycle) above Jungfraujoch, taking into account the specific vertical resolution and sensitivity of both remote sensing techniques by applying their respective averaging kernels to smooth the CTM profiles of HCHO (Rodgers and Connor, 2003).

3.2 FTIR error budget

We present in Table 2 an error budget accounting for the major uncertainties that may affect the HCHO columns retrieved from individual FTIR solar spectra above the ISSJ. This error budget has been split into a systematic and a random component (14.2 and 21.3 %, respectively), with an assumed variability (i.e., diagonal of covariance) close to 50 %. For both components, the total uncertainty is the square root of the sum of the squares of the estimated contributions from the different error sources listed in Table 2. While most of the error terms have been dealt with using perturbation methods applied to all solar spectra recorded during the year 2011 (details are given in third column of Table 2), the contributions of measurements noise (14.7 %), smoothing (10.2 %) and forward model parameters (2.1 %) to the random component have been computed following the OEM formalism of Rodgers (2000), i.e., by calculating the gain and sensitivity matrices, on the basis of a representative subset of solar spectra.

The largest contribution to the total systematic error results from the spectroscopic uncertainties in line intensities (9.7 %) and air-broadening coefficients (8.0 %) for HCHO. We have accounted for an error of 10 % in the HCHO spectroscopic line strengths, commensurate with the work of Perrin et al. (2009) who reported uncertainties between 7 and 10 % for the HCHO features used in this study. The air-broadened half-width in the HITRAN 2008 database, unchanged since the first HITRAN releases (Rothman, 1981), is derived from the early work of Tejwani and Yeung (1977) and is equivalent to the 10 % uncertainty assumed here. The same error value was used by both Jones et al. (2009) and Vigouroux et al. (2009). Other contributions to the systematic component originate from the spectroscopy of the interfering species (5.2 %), calculated independently for each gas by applying the maximal uncertainties stated in the HITRAN 2008 compilation on the line intensities during the retrieval process.

In the present study, we have adopted the HITRAN 2008 database for all FTIR retrievals. We have also tested over the 2010–2012 time period the spectroscopic line parameters and air-broadening coefficients from the recent HITRAN 2012 database (Rothman et al., 2013), providing updated self- and N_2-broadening coefficients of HCHO, as well as their temperature dependence, on the basis of the work of Jacquemart et al. (2010). With respect to our HITRAN 2008 setup, the use of the full HITRAN 2012 compilation considerably decreases the HCHO retrieved columns by 49.0 ± 24.6 % over the 2010–2012 time period and induces the rejection of 21.2 % of all spectra due to negative VMR profiles (instead of 8.9 % initially). We have then gauged the impact of the HITRAN 2012 parameters for the main interfering species separately, adopting still HITRAN 2008 for all other absorbers. Compared to our initial setup (full HITRAN 2008), the use of the sole HCHO parameters have a limited impact on the

Table 2. Impact of major sources of systematic and random uncertainties on typical individual HCHO total column retrievals from FTIR solar spectra above the Jungfraujoch station. These uncertainties have been calculated on the basis of all individual solar spectra recorded during the year 2011 with the exception of the measurement noise, smoothing and model parameter contributions that have been estimated according to the OEM formalism of Rodgers (2000) on the basis of a representative subset of solar spectra.

Error source	Error (%)	Comments
Assumed variability	49.7	WACCM variability relaxed, commensurate with ACE-FTS variability down to 6 km
Systematic errors		
Line intensity HCHO	9.7	Assuming ±10 % uncertainties in HCHO line strengths
Air-broadening coefficient HCHO	8.0	Assuming ±10 % uncertainties in HCHO air-broadening coefficients
Line intensity interfering gases	5.2	Assuming the maximal HITRAN 2008 uncertainties
Instrumental line shape	2.5	±10 % misalignment and instruments bias
Forward model	1.0	Retrieval algorithm-related
HCHO a priori profile	3.0	Assuming HCHO a priori profiles derived from ACE-FTS, GEOS-Chem and IMAGES
Total systematic error	14.2	
Random errors		
Temperature profile	5.0	Assuming the NCEP profile uncertainty pattern (see text)
H_2O and HDO a priori profiles	10.1	Changes by a factor of 2 in a priori slope
SZA	0.7	Assuming ±0.1° bias
Measurement noise	14.7	
Smoothing	10.2	
Model parameters	2.1	
Total random error	21.3	

Table 3. Error budget on the retrieved HCHO vertical column density (VCD) for the MAX-DOAS measurements. The total uncertainty is calculated by adding the different error terms in Gaussian quadrature.

Error sources	Uncertainty on HCHO VCD (%)
Smoothing and noise errors	9.1
Uncertainty related to aerosols	6.3
Uncertainty related to the a priori	8.8
Uncertainty related to the albedo	1.0
Uncertainty on the HCHO cross sections	9.0
Total uncertainty	16.8

retrieved columns (-9.3 ± 5.6 %), while the use of HITRAN 2012 for CH_4 only induces a bias of -11.2 ± 5.0 % on the HCHO amounts. Finally, when assuming HITRAN 2012 for CO_2, the line positions and intensities of which have been modified compared to HITRAN 2008, the retrieved HCHO columns are affected by -26.9 ± 15.6 %. Although CO_2 is not the main interfering species in our microwindows, CO_2 lines overlap the HCHO features in the 2765 and 2778 cm^{-1} microwindows and largely influence the HCHO absorption. When assumed together, the updated parameters for HCHO, CH_4 and CO_2 have a cumulative effect and significantly decrease the retrieved HCHO columns.

For estimating the impact of a bias in the instrumental line shape, we have considered a misalignment of 10 % at the maximal path difference of the instrument, inducing a discrepancy of 2.5 % on the mean HCHO total column. According to comparisons between the SFIT and PROFFIT fitting algorithms, an algorithm-related error of maximum 1 % on the retrieved columns may arise (Hase et al., 2004). Finally, we have fitted the 2011 solar spectra by assuming successively HCHO a priori profiles derived from the ACE-FTS, GEOS-Chem and IMAGES data sets used in the present work, resulting in retrieved HCHO amounts diverging by up to 3.0 %.

Among the random errors, we adopted the uncertainties provided by NCEP for the temperature (i.e., 1.5 °C up to 20 km, 2 °C up to 30 km, 5 °C near 35 km and then progressively increasing up to 9 °C at 50 km), and we further assumed a 0.1 ° error in the solar pointing. Although HDO is accounted for during the first run in the retrieval process, there is a relatively strong dependence of the retrieved HCHO columns on the H_2O and HDO a priori profiles (10.1 %). This uncertainty has been estimated by making the slope of the tropospheric H_2O and HDO VMR profiles simulated by WACCM vary by a factor of 2. This latter corresponds approximately to the change of slope when taking the 2σ SD limits around the annually-averaged H_2O VMR profile retrieved above the ISSJ according to the method of Sussmann et al. (2009).

3.3 MAX-DOAS error budget

The error budget on the retrieved MAX-DOAS HCHO VCDs is estimated as in Hendrick et al. (2014) and Wang et al. (2014). The following error sources are taken into account: smoothing and measurement noise errors, uncertainties on the forward model parameters (mainly aerosol extinction, HCHO a priori profiles and albedo) and uncertainty on the HCHO cross sections. The error budget is summarized in Table 3. The combined smoothing and measurement noise errors reach 9.1 %. Regarding the uncertainty related to the aerosol profile retrieval, an error of 6.3 % is obtained on average on the retrieved HCHO VCD based on a sensitivity test approach using aerosol extinction profiles plus their corresponding error (i.e., the sum of smoothing and noise errors plus a 20 % error due to the uncertainty in the O_4 cross sections; see Wagner et al., 2009 and Clémer et al., 2010) as input and comparing the results to the standard HCHO retrievals. The impact of the a priori (8.8 %) is estimated by taking the mean HCHO profile derived from the IMAGES model output above ISSJ instead of the WACCM model output. In the case of the surface albedo, a value of 0.2 is used throughout the year while the Koelemeijer et al. (2003) climatology shows it can vary from 0.2 (winter) to 0.05 (summer) above the ISSJ area. The related impact on the HCHO VCD is small (1 %). The uncertainty of 9 % on the HCHO cross sections is taken from Pinardi et al. (2013).

4 Results

In this section, we present the daily-averaged HCHO products retrieved from the ground-based FTIR and MAX-DOAS observations recorded at ISSJ and their comparison to both GEOS-Chem and IMAGES models, taking into account the vertical resolution and specific sensitivity of each remote sensing technique. The individual concentration profiles of HCHO simulated by both CTMs throughout the July 2010–December 2012 time period have been interpolated onto the respective vertical grids of FTIR and MAX-DOAS (see Sect. 3.1), then daily averaged and finally smoothed by applying the specific averaging kernels **A** and a priori profiles from the FTIR and MAX-DOAS retrievals, according to the formalism of Rodgers and Connor (2003) and Eq. 1. The averaging kernels used for the smoothing of the CTM output profiles are the averaging kernels obtained from the individual retrieved profiles, seasonally-averaged over spring (from March to May), summer (from June to August), fall (from September to November) and winter (from December to February) throughout the entire investigated time period.

Further in this work, the comparisons between smoothed CTM outputs and ground-based retrieval products are carried out only for the days with observations available, i.e., 261 days for FTIR and 440 days for MAX-DOAS. Given the MAX-DOAS vertical sensitivity, only partial columns of HCHO simulated by the models between the 3.6 and 8 km altitude range are confronted by MAX-DOAS retrieval products, while the comparisons between CTM and FTIR data involve the total columns (representing approximately the tropospheric column). In order to show that the FTIR and MAX-DOAS measurements are complementary for HCHO measurements at Jungfraujoch, we have added to Figs. 4, 6 and 7, involving the FTIR and MAX-DOAS columns the HCHO concentration retrieved by MAX-DOAS for the 3.6–3.8 km near-surface layer, i.e., the first 200 m thick layer directly above the station, where the MAX-DOAS is highly sensitive (see Sect. 3.1).

4.1 Seasonal modulation of formaldehyde

The monthly mean HCHO abundances over the July 2010–December 2012 period and associated 1σ SD, displayed on a 1-year time base, are provided in Fig. 4, with the FTIR total columns (in red) and the MAX-DOAS 3.6–8 km partial columns (in purple) in Fig. 4a and b, respectively. The HCHO concentration for the 3.6–3.8 km layer according to MAX-DOAS is presented in Fig. 4c. The thick solid lines correspond to a running mean fit of the daily average data, with a 15-day step and a 2-month-wide integration time, while the shaded areas represent the 1σ SD around the running mean curve. The running mean fits and the associated 1σ SD of the GEOS-Chem (in blue) and IMAGES (in green) HCHO outputs smoothed by the FTIR (in Fig. 4a) and MAX-DOAS (in Fig. 4b and c) seasonal averaging kernels have been added to Fig. 4 as thick solid lines and thin curves, respectively.

According to Fig. 4, HCHO amounts retrieved from the ground-based FTIR and MAX-DOAS observations at the ISSJ present a clear and consistent seasonal cycle, characterized by a summertime maximum in July–August and a late winter minimum. The running mean total columns from FTIR observations range from 0.92 ± 0.30 to $2.19 \pm 0.72 \times 10^{15}$ molec cm^{-2}, representing a seasonal amplitude of 83 % (defined here as the difference between the maximum and the minimum running means, divided by the annual average over the investigated period), and the running means of partial columns from MAX-DOAS vary between 0.75 ± 0.19 and $1.43 \pm 0.45 \times 10^{15}$ molec cm^{-2}, representing a seasonal amplitude of 66 %, slightly weaker than in the FTIR results. It is worth noting that the seasonal amplitude calculated on the basis of the MAX-DOAS HCHO concentration within the 3.6–3.8 km altitude range equals ~ 130 %, highlighting the strong sensitivity of this instrument to the near-surface layer.

Ground-based FTIR HCHO observations have already been performed at NDACC sites located at different latitudes. Such FTIR measurements have shown a good overall agreement when compared with HCHO observed from space by GOME (Jones et al., 2009), ACE-FTS (Viatte et al., 2014) and SCIAMACHY (Vigouroux et al., 2009). However, it appears firstly that differences in altitude affect the direct comparisons between these ground-based sites and the

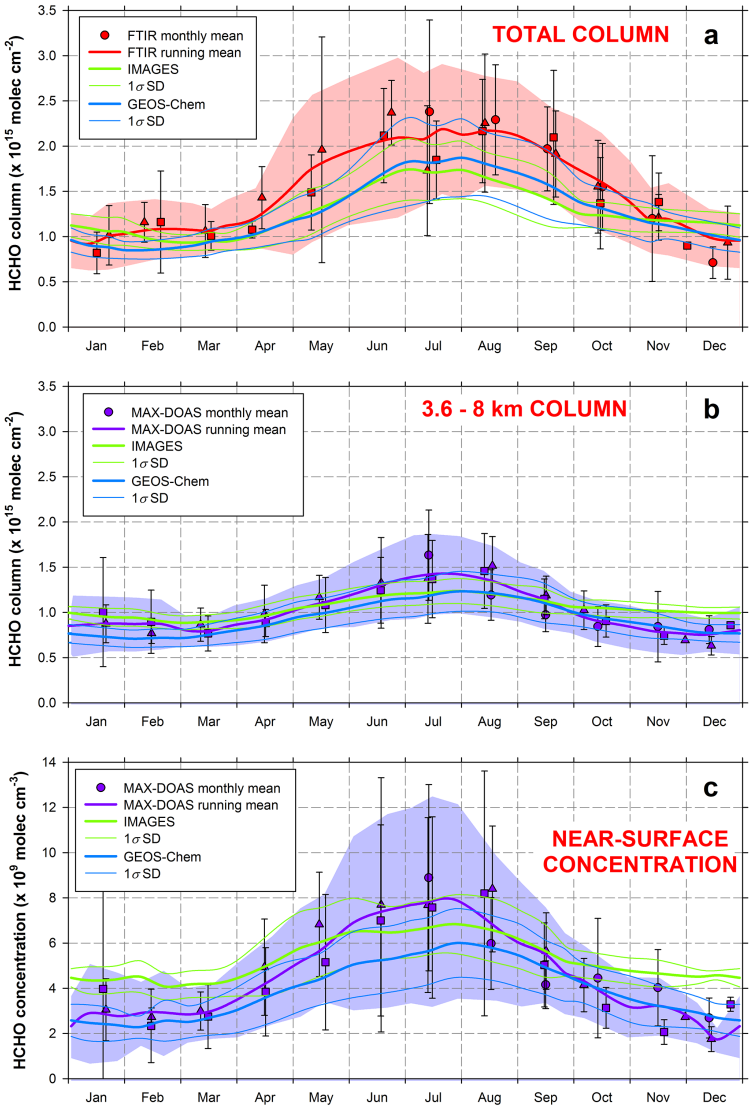

Figure 4. Monthly-mean column abundances of HCHO and associated 1σ SD bars displayed on a 1-year time base, according to the FTIR and MAX-DOAS retrievals (**a** and **b**, respectively) above Jungfraujoch from July 2010 to December 2012. The circle, triangle and square dots correspond to the monthly means from 2010, 2011 and 2012, respectively. The thick curves correspond to a running mean fit to the daily-mean columns displayed on a 1-year time base (not shown here), with a 15-day step and a 2-month-wide integration time. The shaded areas represent the 1σ SD associated with the running mean curves. As it is calculated on the basis of the daily-mean columns, this 1σ SD convolves interannual variability and variability of the monthly mean. Note that the FTIR abundances correspond to total columns and the MAX-DOAS data consist of partial columns within the 3.6–8 km altitude range. The HCHO amounts calculated from the smoothed CTM profiles are displayed in each frame as running mean fit (solid thick curve) and the associated 1σ SD (thin line). A similar figure, but for the HCHO concentration derived from MAX-DOAS and the CTMs within the 3.6–8 km near-surface layer, is drawn in (**c**).

ISSJ. Viatte et al. (2014) measured HCHO total columns in the Arctic at another background site in Eureka, Canada (80.0° N, 86.4° W, 610 m a.s.l.), and reported monthly averaged values over the 5-year period 2007–2011 from 0.27 to 3.14×10^{15} molec cm^{-2}. The total columns derived from the FTIR data set of Jungfraujoch are consistent with the measurements from Eureka, given that the strong vertical gradient of HCHO concentration in the troposphere and the ISSJ elevation contribute to the relatively lower HCHO amounts retrieved at Jungfraujoch. Moreover, Viatte et al. (2014) reported a seasonal cycle characterized by an amplitude of 93 % at Eureka, in agreement with the ISSJ FTIR observations. It is difficult to compare the ISSJ with other background sites because many of them experience enhancements in HCHO concentration resulting from distant anthropogenic activity and biomass burning. For example, Notholt et al.

(1997) reported higher monthly mean total columns between 1.67 and 4.25 $\times$ 10^{15} molec cm^{-2} at Ny Ålesund, Spitsbergen (78.9° N, 11.9° E, 15 m a.s.l.), for the 1992–1995 time period, as well as a second maximum during winter. Part of these differences compared to the ISSJ results might be explained by the updated spectroscopic line intensities for HCHO in HITRAN 2008 (Perrin et al., 2009) used in this study, increased by approximately 30 % compared to the previous HITRAN compilations and hence decreasing the retrieved total columns, added to the fact that direct transport of pollutants from Europe to Ny Ålesund occurs especially during winter. In the Southern Hemisphere, Jones et al. (2009) presented monthly mean total columns varying between 1.5 and 4.0 $\times$ 10^{15} molec cm^{-2} for the 1992–2005 period at Lauder, New Zealand (45.0° S, 169.7° E, 370 m a.s.l.), and Vigouroux et al. (2009) retrieved values ranging from 1.5 to 7.0 $\times$ 10^{15} molec cm^{-2} at Saint-Denis, Reunion Island (20.9° S, 55.5° E, 10 m a.s.l.), during 2004–2007 campaigns, both sites being largely influenced by long-range transport of biomass burning plumes and HCHO precursors originating from Australia and Africa/Madagascar, respectively.

The seasonal variability of HCHO observed by both FTIR and MAX-DOAS instruments (Fig. 4) is consistent with the annual variations of the atmospheric photochemistry as well as with the annual cycle of biogenic emissions at Northern Hemisphere mid-latitudes and more specifically over Europe (see Dufour et al., 2009b; Curci et al., 2010) and above Jungfraujoch (see Legreid et al., 2008, and references therein). Indeed, on an overall scale over Europe, the background of HCHO throughout the year is supplied by oxidation of CH_4 and other long-lived VOCs (Dufour et al., 2009b; Curci et al., 2010). In summer, enhanced temperatures and insolation induce a higher photochemical oxidation rate of VOCs by the OH radicals, which results in increasing the HCHO formation. Moreover, the summer periods are also characterized by large biogenic emissions of NMVOCs that are high-yield HCHO precursors, such as isoprene, taking place in the continental boundary layer and originating from plants and temperate forests during the growing season in the Northern Hemisphere (e.g., Dufour et al., 2009b; Stavrakou et al., 2009a; Curci et al., 2010). More specifically at Jungfraujoch, Legreid et al. (2008) reported measurements of higher concentrations in NMVOCs during summertime, which are attributed to secondary oxidation processes and higher emissions from biogenic sources essentially originating from northern Italy (because of the higher biogenic activity in this region compared to the north of the Alps). As explained previously in Sect. 2.1, air masses containing such biogenic compounds might be transported from the boundary layer to the ISSJ by different atmospheric mechanisms (air advection, thermally driven convection, front passage and topographic venting) and eventually add to the NMVOC precursors of HCHO. For instance, Bader et al. (2014) recently highlighted the role of biogenic sources and plant growth, especially from the region south of the Alps, in the increase of methanol concentration, a high-yield precursor of HCHO, during summertime at Jungfraujoch. Conversely, minima of HCHO amounts observed at the ISSJ (Fig. 4) are primarily due to the lower radiation and the relatively weak atmospheric moisture during winter, inducing lower concentrations of OH radicals and hence lower oxidation rates of VOCs. Nevertheless, more elevated concentrations in reactive compounds from anthropogenic origin (such as benzene, toluene and butane), which are potential precursors of HCHO, were measured in winter at Jungfraujoch (Balzani Lööv et al., 2008; Legreid et al., 2008; Starokozhev et al., 2009) mainly because of their longer lifetimes and more intensive anthropogenic combustion during this season. Using a statistical trajectory model, Legreid et al. (2008) identified northern Italy, southern France and southern Germany (highly industrialized and populated areas) as the main contributors to these anthropogenic emissions.

Figure 4 shows that both GEOS-Chem and IMAGES models, smoothed by the specific averaging kernels of FTIR and MAX-DOAS, are able to reproduce the seasonal variations of HCHO above Jungfraujoch over the July 2010–December 2012 time period, showing a maximum in summer and a minimum in winter. However, both CTMs simulate on average lower HCHO amounts than the columns retrieved from FTIR (from March to October) and MAX-DOAS (from June to August) observations, although these differences are not significant given the 1σ SD associated with the ground-based measurements. In winter, HCHO abundances from GEOS-Chem are relatively weaker or equal to FTIR and MAX-DOAS data, while IMAGES provides higher HCHO columns during this time period, especially in comparison with the MAX-DOAS partial columns. Such a difference can be explained by the fact that Jungfraujoch is sensitive to anthropogenic NMVOC emissions in winter and these differ between the two models. Indeed, total anthropogenic emissions over Europe (calculated within the 20° W–60° E and 36° N–88° N area) for NMVOC species common to both models amount to 4.7 Tg C yr^{-1} for GEOS-Chem and 15.7 Tg C yr^{-1} for IMAGES. Consequently, the CTMs simulate lower seasonal amplitudes above Jungfraujoch – more precisely, 80, 56 and 94 % for GEOS-Chem, and 63, 33 and 52 % for IMAGES – when successively compared to FTIR (83 %), 3.6–8 km MAX-DOAS (66 %) and 3.6–3.8 km MAX-DOAS (130 %) seasonal amplitudes, respectively. Ground-based observations from both remote sensing instruments systematically provide larger 1σ SD around the running mean curve than the models, especially during summertime. Indeed, the models dilute local enhancements in HCHO because of their relatively coarse spatial resolution.

The discrepancies between the FTIR and MAX-DOAS seasonal cycles of HCHO and the smoothed CTM outputs (reported in Table 4) have been estimated on the basis of the daily means over the entire July 2010–December 2012 time period by averaging the daily fractional differences (defined here as the difference between two columns divided

Table 4. Mean fractional differences (in $\% \pm 1\sigma$), calculated on the basis of daily-mean values, between the FTIR and MAX-DOAS HCHO columns (and near-surface concentration) and the CTM outputs for the July 2010–December 2012 time period above Jungfraujoch. These mean fractional differences are given for the comparisons involving the CTM profiles with and without smoothing by the FTIR and MAX-DOAS averaging kernels.

	FTIR total column	3.6–8 km MAX-DOAS column	3.6–3.8 km MAX-DOAS column
With smoothing			
IMAGES	-12.7 ± 36.2	5.3 ± 27.0	22.8 ± 44.6
GEOS-Chem	-12.3 ± 33.5	-5.8 ± 21.9	-7.4 ± 35.2
Without smoothing			
IMAGES	-10.7 ± 37.1	7.9 ± 27.4	23.3 ± 44.2
GEOS-Chem	-19.4 ± 35.4	-8.3 ± 29.2	-9.9 ± 35.0

by the average of these two columns) between the retrieved and the simulated HCHO columns (and concentrations in the near-surface layer). Such fractional difference aims at reducing the impact of the large HCHO columns in the overall comparison between the two data sets. Table 4 summarizes these mean fractional differences for comparisons involving the CTM outputs with and without smoothing by the FTIR and MAX-DOAS averaging kernels. These results show that smoothed GEOS-Chem columns underestimate both ground-based data sets and that smoothed IMAGES columns underestimate and overestimate the FTIR and MAX-DOAS data, respectively. Moreover, the smoothing generally appears to improve the comparisons between the CTMs and the ground-based data sets. When considered over the year as a whole, the 1σ SD associated with these mean fractional differences indicates that the discrepancies are not significant. Parts of these large errors are due to the inability of the models to reproduce the seasonal amplitude of HCHO abundances retrieved from FTIR and MAX-DOAS observations, as highlighted previously in Fig. 4.

In the present study, a direct comparison between the FTIR total columns and the MAX-DOAS 3.6–8 km partial columns would not be meaningful (see Sect. 3.1), but the CTM simulations of HCHO still allow for an estimation of the consistency between both ground-based retrievals. Indeed, the mean fractional differences between the models and the FTIR data as well as the mean fractional differences calculated between the models and the MAX-DOAS observations are embedded in the respective uncertainties of the ground-based measurements (see Table 2, 3 and 4). As the HCHO seasonal cycles derived from the same CTM simulations present similar discrepancies to the ground-based data sets when the CTM profiles are respectively smoothed by the FTIR and MAX-DOAS averaging kernels, this is an indication that the FTIR and MAX-DOAS retrievals are consistent between each other for HCHO above Jungfraujoch over the investigated time period.

4.2 Formaldehyde concentration profiles

Figure 5 displays the seasonal averages of the HCHO concentration profiles (in molec cm^{-3}) above Jungfraujoch for the FTIR and MAX-DOAS data sets, as well as for smoothed CTM outputs, calculated on the basis of daily mean profiles over the entire July 2010–December 2012 time period. The shaded areas correspond to the 1σ SD around the mean seasonal profile retrieved from FTIR (in red) and MAX-DOAS (in purple) observations. In addition, the slope of each concentration profile has been determined from a linear regression of data points within the 3.6–7 km altitude range common to the vertical resolution of both FTIR and MAX-DOAS techniques.

As already presented by Fig. 4, Fig. 5 illustrates the seasonal modulations of the averaged retrieved profiles in the lower troposphere above Jungfraujoch for each measurement technique. This modulation explains the largest part of the seasonal variability observed in the HCHO columns derived from the ground-based measurements. At the ISSJ altitude, mean HCHO concentrations indeed vary between 3.0 and 7.0×10^9 molec cm^{-3} from wintertime to summertime according to the FTIR data set and up to 8.0×10^9 molec cm^{-3} for the summer mean MAX-DOAS profiles. Throughout the year, these concentrations decrease rapidly with altitude, down to between 1.5 and 2.0×10^9 molec cm^{-3} at 7 km altitude in the MAX-DOAS profile, which corresponds to the upper limit of vertical sensitivity for this instrument, and down to negligible values around 12 km altitude regarding the FTIR data.

The higher resolution of the MAX-DOAS profiles allows for a better representation of the first tropospheric layers directly above Jungfraujoch in comparison with FTIR. This higher resolution results in stronger variations of the slope values associated with the retrieved HCHO profiles and in generally larger standard deviations around the mean profile in the closest vicinity of the ISSJ within each seasonal time period. In predominant background conditions such as at Jungfraujoch, a significant part of the HCHO column is situated in the free troposphere ($\sim 25\,\%$ on average is lo-

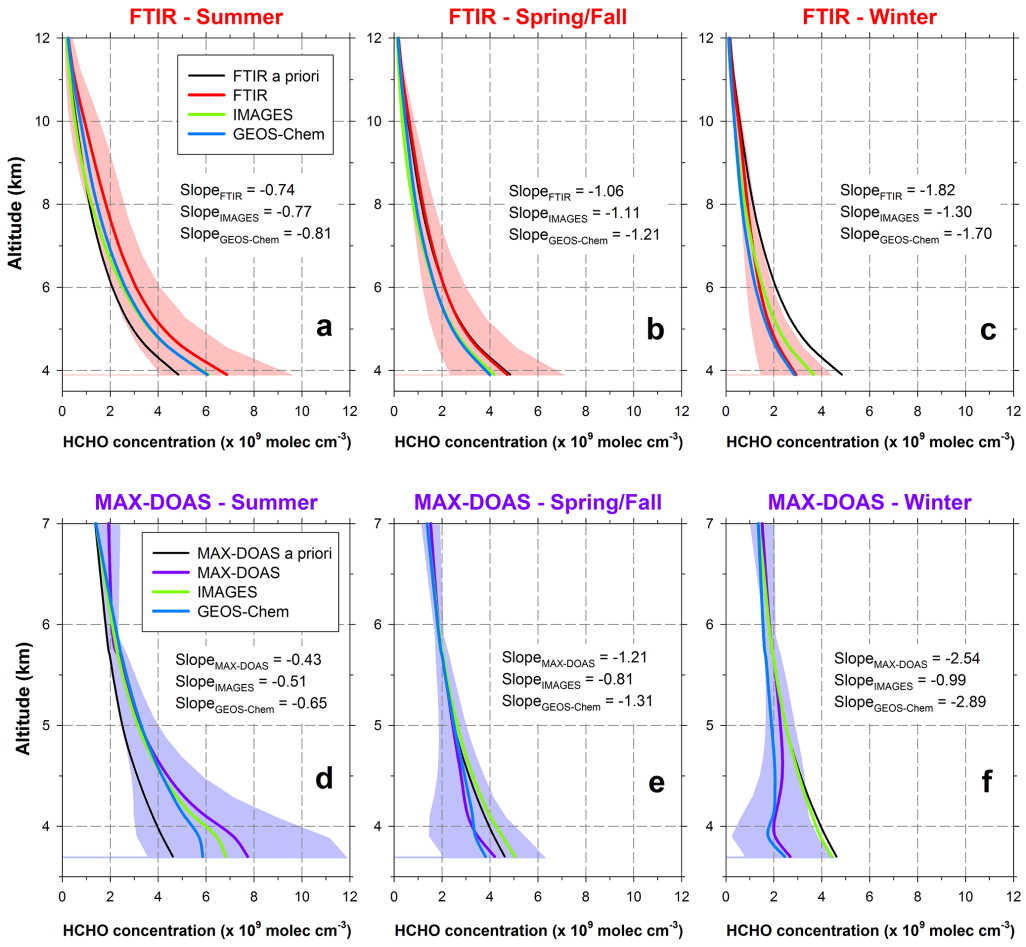

Figure 5. Mean seasonal profiles of HCHO concentration (in molec cm^{-3}) above Jungfraujoch according to the FTIR and MAX-DOAS retrievals (upper and lower frames, respectively), calculated on the basis of the daily means over the July 2010–December 2012 time period. The shaded areas correspond to the 1σ SD around the mean profiles. The smoothed profiles derived from the IMAGES (in green) and GEOS-Chem (in blue) simulations have been added to each frame. The mean slope of each profile has been estimated by adjusting a linear regression between 3.6 and 7 km altitude with the least mean squares method.

cated above 8 km), while in most other NDACC sites the contribution of the column above 8 km to the total column is generally negligible due to lower elevation and more polluted conditions. As previously highlighted by the respective eigenvectors and averaging kernels of FTIR and MAX-DOAS displayed in Fig. 3, both FTIR (because of its larger altitude range of sensitivity) and MAX-DOAS (due to its very high vertical resolution in the lowest tropospheric layers) are complementary and provide added-value measurements of HCHO distribution above Jungfraujoch.

The comparison between the smoothed CTM profiles and the ground-based retrievals presented in Fig. 5, as well as their associated slopes within the 3.6–7 km altitude range, confirms that both GEOS-Chem and IMAGES simulations tend to underestimate the retrieved HCHO abundances during summertime and that IMAGES overestimates it in winter. Regarding the spring and fall seasons, both models simulate slightly lower HCHO concentrations than FTIR, and IMAGES still overestimates HCHO amounts compared to the MAX-DOAS observations. However, these mean profiles derived from the smoothed CTM outputs are generally embedded in the 1σ SD area of the ground-based data on the entire range of investigated altitudes, and hence the related biases are not significant at that level of uncertainty. It is worth noting that the anomalies of the CTM outputs relative to the FTIR profile extend throughout the column in summer, while the MAX-DOAS results imply that the largest discrepancies take place near the surface. This results from the differences of resolution between both instruments (see Sect. 3.1), the FTIR retrievals being sensitive up to 10–12 km and the MAX-DOAS profiles tending to reproduce the a priori above 5.5 km.

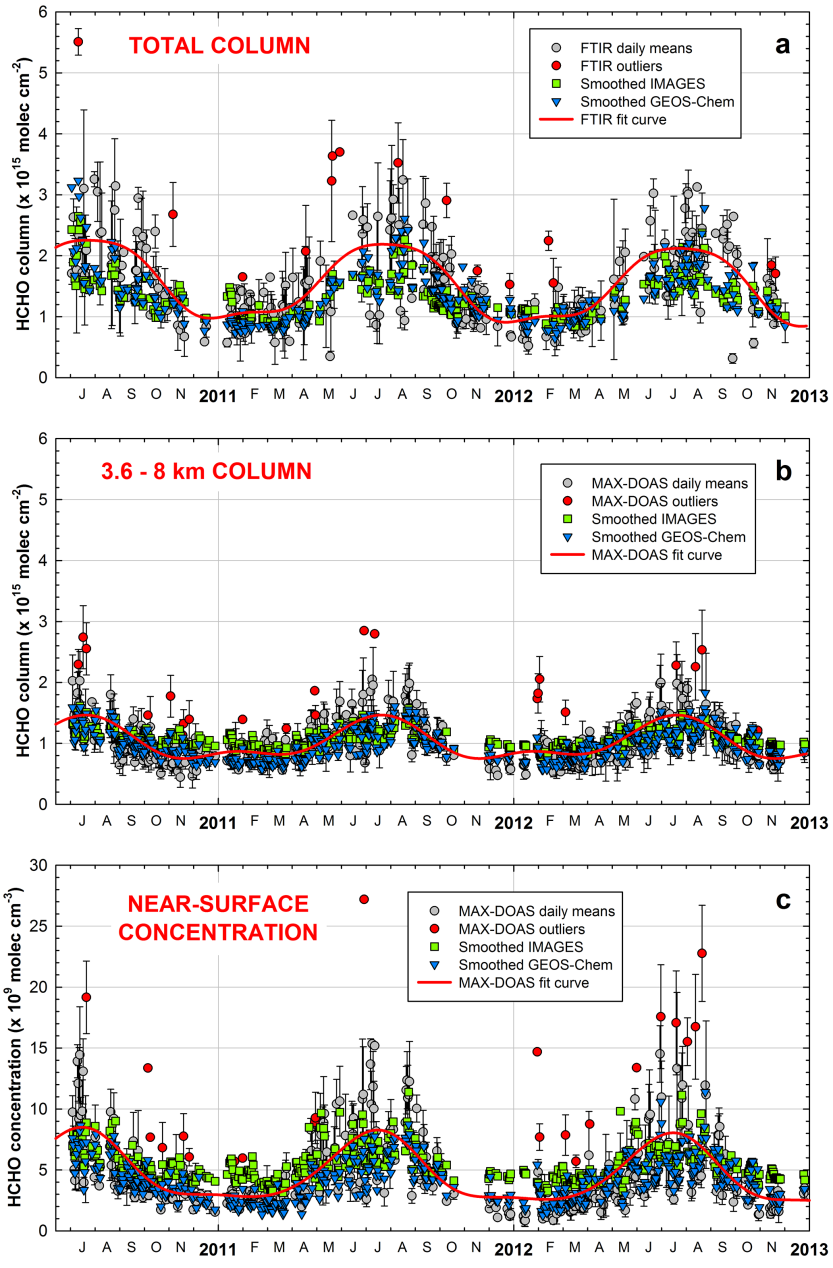

Figure 6. Time series of daily-mean HCHO abundances and the associated 1σ SD bars from the FTIR (**a**) and MAX-DOAS (**b**) data sets. The solid thick curves (in red) represent the fitting function calculated by applying to the whole time series the statistical bootstrap resampling method from Gardiner et al. (2008). The daily-mean HCHO amounts from the smoothed IMAGES and GEOS-Chem models are displayed in green and blue, respectively. A similar figure, but for the HCHO concentration derived from MAX-DOAS and the CTMs within the 3.6–3.8 km near-surface layer, is drawn in (**c**). The outliers (red dots) correspond to daily observation values with relative anomalies to the curve fit calculated by Gardiner et al. (2008), higher than the 95th percentile value of all relative anomalies of the data set.

4.3 Formaldehyde daily time series

Figure 6 presents the July 2010–December 2012 time series of daily-averaged HCHO columns and the associated 1σ SD, as retrieved from the FTIR and MAX-DOAS observations in Fig. 6a and b, respectively. The HCHO amounts consist of total tropospheric columns (FTIR) and in partial columns within the 3.6–8 km altitude range (MAX-DOAS) according to the vertical resolution and sensitivity of each remote sensing instrument. The daily mean outputs, derived from the HCHO profiles provided by both GEOS-Chem and IMAGES models and smoothed by applying the FTIR and MAX-DOAS averaging kernels, are drawn in blue and in green for the coincident days with the ground-based data sets.

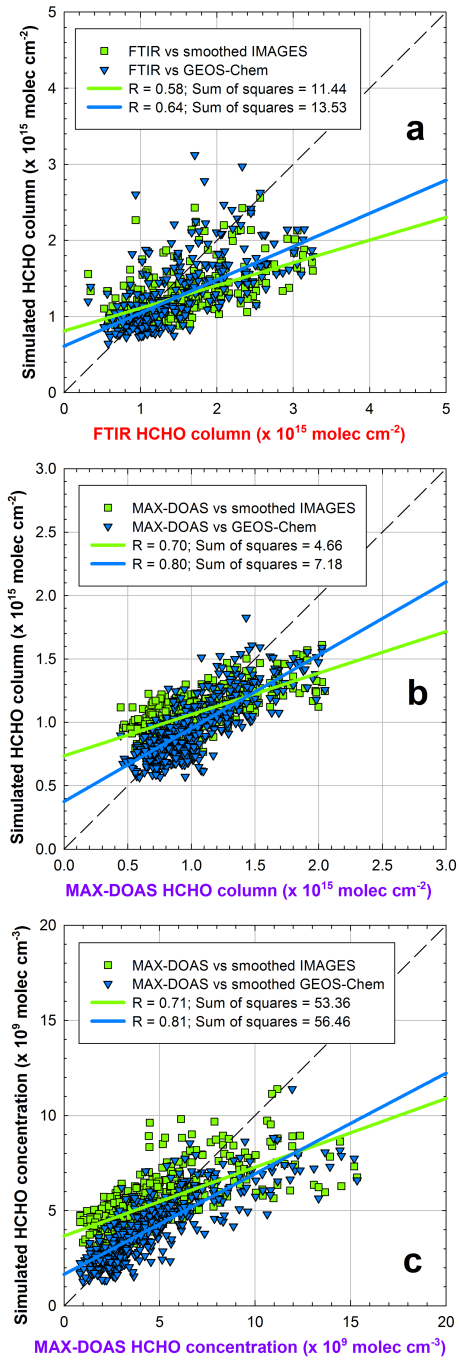

Figure 7. Direct comparisons between the FTIR and smoothed CTM daily-mean HCHO columns (**a**) and between the MAX-DOAS and smoothed CTM daily-mean partial columns within the 3.6–8 km altitude range (**b**) displayed in Fig. 6. The blue and green straight lines correspond to the linear regressions (with R as the correlation) between the ground-based measurements and the model outputs. A similar figure, but for the HCHO concentration derived from MAX-DOAS and the CTMs within the 3.6–3.8 km near-surface layer, is drawn in frame (**c**). Outliers identified as red dots in Fig. 6 have been discarded from the data sets.

The red solid thick curves represent the fitting of the whole time series by the statistical bootstrap resampling method (Gardiner et al., 2008), which is a combination of a linear function and a third-order Fourier series accounting for the intra-annual variability of the data set. The similar time series for the 3.6–3.8 km near-surface HCHO concentration derived from MAX-DOAS and both CTMs are drawn in Fig. 6c.

The daily-averaged total columns of HCHO retrieved from the FTIR solar spectra at the ISSJ vary between 0.32 and 5.51×10^{15} molec cm^{-2}. These values are consistent with total columns retrieved from FTIR solar spectra recorded at other NDACC sites (Notholt et al., 1997; Jones et al., 2009; Vigouroux et al., 2009; Viatte et al., 2014) given the ISSJ elevation and the dominance of weakly polluted air masses. For instance, Viatte et al. (2014) reported total column amounts ranging from 0.02 to 6.30×10^{15} molec cm^{-2} over a 5-year time series at Eureka. The MAX-DOAS time series present a minimum of partial column within the 3.6–8 km altitude range equal to 0.44×10^{15} molec cm^{-2} and a maximum reaching 2.85×10^{15} molec cm^{-2}. The FTIR data set shows the larger seasonal amplitude (consistent with the seasonal modulation previously highlighted in Fig. 4) but also the higher dispersion around the fitting function, with an absolute mean fractional difference over the whole time period equal to 24.1 % compared to 20.0 % for the MAX-DOAS time series. The minimum daily values during wintertime are approximately equal to 1.0×10^{15} molec cm^{-2} with a small dispersion around this value for both FTIR and MAX-DOAS time series, indicating a dominant contribution of the first tropospheric layers to the total amounts of HCHO above Jungfraujoch during winter (80–90 %) and conversely a less significant contribution during summer (60–70 %).

These results show that the seasonal modulation of HCHO and its day-to-day variability (for the latter, solely in the case where the uncertainties on the FTIR measurements are consistent with the MAX-DOAS uncertainties) are not solely due the variability in the lower troposphere (Fig. 6b and c) where the MAX-DOAS instrument is the most sensitive. Conversely, part of the variability also takes place in higher tropospheric layers. Indeed, the HCHO formation in the upper troposphere might be seasonally enhanced by large-scale atmospheric transport and/or convective fluxes bringing more precursor compounds to the upper layers (Stickler et al., 2006; Fried et al., 2008). In this latter case, such a variability may only be captured by the FTIR instrument owing to its more uniform vertical sensitivity throughout the troposphere compared to the MAX-DOAS, as indicated by the larger seasonal amplitude of the FTIR data set.

Finally, these results also suggest that the HCHO seasonality above Jungfraujoch is not solely influenced by the variations of photolysis and oxidation rate of CH_4, otherwise this seasonal signal would affect homogeneously the entire column. Conversely, the HCHO seasonality and its day-to-day variability seem to be driven rather by incursions of NMVOC precursors from anthropogenic (especially in win-

ter) and biogenic (as early in the year as March–April until late summer) sources through frequent injection of air parcels from boundary layer (see Sect. 2.1 and 4.1). A more detailed investigation of the different emission sources responsible for the HCHO seasonality and its day-to-day variability above Jungfraujoch is part of ongoing work involving FTIR decadal time series and CTM sensitivity runs.

The direct comparison performed between the FTIR and MAX-DOAS measurements and the HCHO columns derived from the smoothed profiles provided by GEOS-Chem and IMAGES, on the basis of the daily means, are drawn in Fig. 7a and b. The similar comparison involving HCHO concentration in the 3.6–3.8 km near-surface layer is presented in Fig. 7c. In order to improve these comparisons, some outliers, probably due to transport of air masses with high NMVOC precursor concentrations, have been discarded because the models are generally unable to reproduce such events. These outliers correspond to daily observation values with relative anomalies to the curve fit calculated by Gardiner et al. (2008) higher than the 95th percentile value of all relative anomalies of the data set. These outliers are identified for each time series as red dots in Fig. 6. The correlations between the 3.6–8 km MAX-DOAS data set and the models ($R = 0.80$ and 0.70 with GEOS-Chem and IMAGES, respectively; Fig. 7b) are better than those between FTIR measurements and smoothed CTM outputs ($R = 0.64$ and 0.58; Fig. 7a). The similar correlations but for comparisons involving the discarded outliers are 0.75 and 0.63 for MAX-DOAS versus GEOS-Chem and IMAGES, respectively, and 0.62 and 0.57 for FTIR versus GEOS-Chem and IMAGES. Although most of the large differences between the model data and the ground-based observations occur for daily means in summer or during the spring/fall season, tests have shown that these differences are not significantly related to a more particular time period of the year. Since considering only the errors associated with the HCHO columns retrieved from ground-based observations cannot explain all the observed biases between models and both FTIR and MAX-DOAS, these results also suggest that part of these discrepancies might be due to a day-to-day variability of the HCHO columns not captured by the model simulations above Jungfraujoch.

5 Conclusions

In the present study, we have described strategies for HCHO retrieval performed at the high-altitude remote station of Jungfraujoch, derived from ground-based FTIR solar spectra and UV-visible MAX-DOAS scans recorded during the July 2010–December 2012 time period. HCHO profiles and the corresponding column amounts have been derived from FTIR measurements using four microwindows that encompass the 2760–2860 cm^{-1} spectral domain (based on Vigouroux et al., 2009) according to an OEM retrieval process. The MAX-DOAS strategy consists of deriving DSCDs by spectral fitting in the 328.5–358.0 nm wavelength range and then in applying an OEM-based profiling method on the DSCDs to produce HCHO vertical profiles. Characterization of the retrieval products has revealed different vertical resolution and sensitivity between both remote sensing instruments. Indeed, most of the information on the vertical distribution of HCHO contained in the MAX-DOAS measurements is located in the first tropospheric layers above the ISSJ (below 5.5 km altitude) with a maximum sensitivity in the lowest layers close to the ground, while FTIR retrievals are mainly sensitive in the free troposphere (up to 12 km altitude) and vertically unresolved. Such a difference of vertical resolution does not allow direct comparisons of FTIR and MAX-DOAS data sets. Therefore we have successively confronted FTIR total columns and MAX-DOAS 3.6–8 km partial columns as well as the corresponding vertical profiles to HCHO columns and profiles simulated by two state-of-the-art three-dimensional CTMs: GEOS-Chem and IMAGES v2. The vertical sensitivity specific to each ground-based instrument has been taken into account by convolving the HCHO profiles produced by the CTMs above Jungfraujoch over the whole investigated time period by the FTIR and MAX-DOAS AVKs, respectively.

Analysis of such comparisons has indicated that HCHO profiles and the corresponding columns derived from both ground-based remote sensing techniques show consistent seasonal modulation at the ISSJ over the July 2010–December 2012 time period, characterized by summertime maximum and wintertime minimum. A dominant contribution of the first tropospheric layers to the total column of HCHO has been highlighted in winter (80–90 %), while this contribution has been slightly dampened in summer (60–70 %). Considering that the FTIR data set has presented higher seasonal amplitude than MAX-DOAS results, this suggests that seasonal modulation of HCHO (as well as its day-to-day variability) is not solely driven by lower-tropospheric variability but also influenced by HCHO variability occurring in higher tropospheric layers, mainly reproduced by the FTIR retrievals. Moreover, when compared to the FTIR and MAX-DOAS measurements, the CTM outputs have shown discrepancies embedded in the respective uncertainties of the ground-based measurements, i.e., mainly an underestimation in summer for both models. These results indicate a consistency between the HCHO retrievals from both remote sensing techniques as well as their complementarity for studying the vertical distribution of HCHO above Jungfraujoch.

Due to its remote location and its altitude, the ISSJ often allows investigation of atmospheric background conditions and is characterized by low HCHO. For example, layers above 8 km altitude contribute approximately 25 % to the total column above Jungfraujoch, while this contribution remains generally negligible at other NDACC stations. Therefore, the FTIR and MAX-DOAS data sets used in the present study and combined with CTM outputs have the potential to

provide an important background test site for investigating the vertical HCHO distribution, e.g., for satellite retrievals.

The seasonal modulation of HCHO above Jungfraujoch is not solely driven by the variation of the photo-oxidation rate of CH_4. Although the ISSJ is mainly located in the free troposphere, frequent injections of air masses from the boundary layer due to different mechanisms such as tropospheric venting, front passage and thermally driven convection may indeed occur, especially during summertime, bringing NMVOC precursors of HCHO from anthropogenic and biogenic emission sources to Jungfraujoch (e.g., Lugauer et al., 2000; Henne et al., 2004, 2005; Li et al., 2005; Legreid et al., 2008). Therefore, further work is required to identify and estimate the contribution of the different NMVOCs to the HCHO formation at the ISSJ.

The present study describes and validates an optimized FTIR strategy for HCHO retrieval at Jungfraujoch. This strategy is implemented in an ongoing work which aims at exploiting the multi-decadal observational time series of FTIR solar spectra available at the ISSJ (back to 1988) in order to investigate interannual variability and produce a long-term trend of HCHO. Little has been observed about the intra-day variability of HCHO; such a multi-decadal time series will also be helpful to consider this issue.

Further investigations involving sensitivity runs are also needed to explain why the observed HCHO amounts are underestimated by GEOS-Chem and IMAGES in summer above Jungfraujoch. Such sensitivity runs are beyond the scope of this study, which mainly focuses on the retrieval strategies. However, preliminary tests have already suggested that the HCHO concentration simulated by the CTMs at the ISSJ is strongly influenced by different emission sources implemented by the models. Moreover, after comparison with HCHO amounts retrieved from space-based ACE-FTS measurements, Dufour et al. (2009b) reported that GEOS-Chem and LMDz-INCA (INteractive Chemistry and Aerosols) underestimate the summer maximum over Europe (and Russia) due to large uncertainties remaining in the emissions of HCHO precursors.

The Supplement related to this article is available online at doi:10.5194/amt-8-1733-2015-supplement.

Acknowledgements. The contributions of University of Liège and BIRA-IASB have been mainly supported by the PRODEX project ACROSAT funded by the Belgian Science Policy Office (BELSPO). The F.R.S.-FNRS and the Fédération Wallonie Bruxelles contributed to observational activities support. E. Mahieu is a research associate with F.R.S.-FNRS. The Swiss GAW-CH program is further acknowledged. We are grateful to the International Foundation High Altitude Research Stations Jungfraujoch and Gornergrat (HFSJG, Bern) for supporting the facilities needed to perform the observations. We further acknowledge the vital contribution from all the Belgian colleagues in performing the Jungfraujoch FTIR observations used here. This research was also financially supported at ULg and BIRA-IASB by the EU 7th Framework Programme projects NORS (contract 284421) and AGACC-II (BELSPO, Brussels) and at BIRA-IASB by the FP7 project ACTRIS (contract 262254).

Edited by: R. Volkamer

References

Atkinson, R.: Atmospheric chemistry of VOCs and NO_x, Atmos. Environ., 34, 2063–2101, doi:10.1016/S1352-2310(99)00460-4, 2000.

Bader, W., Stavrakou, T., Muller, J.-F., Reimann, S., Boone, C. D., Harrison, J. J., Flock, O., Bovy, B., Franco, B., Lejeune, B., Servais, C., and Mahieu, E.: Long-term evolution and seasonal modulation of methanol above Jungfraujoch (46.5° N, 8.0° E): optimisation of the retrieval strategy, comparison with model simulations and independent observations, Atmos. Meas. Tech., 7, 3861–3872, doi:10.5194/amt-7-3861-2014, 2014.

Balzani Lööv, J. M., Henne, S., Legreid, G., Staehelin, J., Reimann, S., Prévôt, A. S. H., Steinbacher, M., and Vollmer, M. K.: Estimation of background concentrations of trace gases at the Swiss Alpine site Jungfraujoch (3580 m a.s.l.), J. Geophys. Res., 113, D22305, doi:10.1029/2007JD009751, 2008.

Bernath, P. F., McElroy, C. T., Abrams, M. C., Boone, C. D., Butler, M., Camy-Peyret, C., Carleer, M., Clerbaux, C., Coheur, P.-F., Colin, R., DeCola, P., De Mazière, M., Drummond, J. R., Dufour, D., Evans, W. F. J., Fast, H., Fussen, D., Gilbert, K., Jennings, D. E., Llewellyn, E. J., Lowe, R. P., Mahieu, E., McConnell, J. C., McHugh, M., McLeod, S. D., Michaud, R., Midwinter, C., Nassar, R., Nichitiu, F., Nowlan, C., Rinsland, C. P., Rochon, Y. J., Rowlands, N., Semeniuk, K., Simon, P., Skelton, R., Sloan, J. J., Soucy, M.-A., Strong, K., Tremblay, P., Turnbull, D., Walker, K. A., Walkty, I., Wardle, D. A., Wehrle, V., Zander, R., and Zou, J.: Atmospheric Chemistry Experiment (ACE): mission overview, Geophys. Res. Lett., 32, L15S01, doi:10.1029/2005GL022386, 2005.

Bey, I., Jacob, D. J., Yantosca, R. M., Logan, J. A., Field, B. D., Fiore, A. M., Li, Q., Liu, H. Y., Mickley, L. J., and Schultz, M. G.: Global modeling of tropospheric chemistry with assimilated meteorology: model description and evaluation, J. Geophys. Res.-Atmos., 106, 23073–23095, doi:10.1029/2001JD000807, 2001.

Bogumil, K., Orphal, J., Homann, T., Voigt, S., Spietz, P., Fleischmann, O. C., Vogel, A., Hartmann, M., Bovensmann, H., Frerik, J., and Burrows, J. P.: Measurements of molecular absorption spectra with the SCIAMACHY Pre-Flight Model: Instrument characterization and reference spectra for atmospheric remote sensing in the 230–2380 nm region, J. Photoch. Photobio. A, 157, 167–184, 2003.

Carlier, P., Hannachi, H., and Mouvier, G.: The chemistry of carbonyl compounds in the atmosphere: a review, Atmos. Environ., 20, 2079–2099, doi:10.1016/0004-6981(86)90304-5, 1986.

Chance, K. V. and Spurr, R. J.: Ring effect studies: Rayleigh scattering, including molecular parameters for rotational Raman scattering, and the Fraunhofer spectrum, Appl. Optics, 36, 5224–5230, 1997.

Chang, L., Palo, S., Hagan, M., Richter, J., Garcia, R., Riggin, D., and Fritts, D.: Structure of the migrating diurnal tide in the Whole Atmosphere Community Climate Model (WACCM), Adv. Space Res., 41, 1398–1407, doi:10.1016/j.asr.2007.03.035, 2008.

Clémer, K., Van Roozendael, M., Fayt, C., Hendrick, F., Hermans, C., Pinardi, G., Spurr, R., Wang, P., and De Mazière, M.: Multiple wavelength retrieval of tropospheric aerosol optical properties from MAXDOAS measurements in Beijing, Atmos. Meas. Tech., 3, 863–878, doi:10.5194/amt-3-863-2010, 2010.

Collaud Coen, M., Weingartner, E., Furger, M., Nyeki, S., Prévôt, A. S. H., Steinbacher, M., and Baltensperger, U.: Aerosol climatology and planetary boundary influence at the Jungfraujoch analyzed by synoptic weather types, Atmos. Chem. Phys., 11, 5931–5944, doi:10.5194/acp-11-5931-2011, 2011.

Curci, G., Palmer, P. I., Kurosu, T. P., Chance, K., and Visconti, G.: Estimating European volatile organic compound emissions using satellite observations of formaldehyde from the Ozone Monitoring Instrument, Atmos. Chem. Phys., 10, 11501–11517, doi:10.5194/acp-10-11501-2010, 2010.

De Smedt, I., Stavrakou, T., Müller, J.-F., van der A. R. J., and Van Roozendael, M.: Trend detection in satellite observations of formaldehyde tropospheric columns, Geophys. Res. Lett., 37, L18808, doi:10.1029/2010GL044245, 2010.

Dufour, G., Szopa, S., Barkley, M. P., Boone, C. D., Perrin, A., Palmer, P. I., and Bernath, P. F.: Global upper-tropospheric formaldehyde: seasonal cycles observed by the ACE-FTS satellite instrument, Atmos. Chem. Phys., 9, 3893–3910, doi:10.5194/acp-9-3893-2009, 2009a.

Dufour, G., Wittrock, F., Camredon, M., Beekmann, M., Richter, A., Aumont, B., and Burrows, J. P.: SCIAMACHY formaldehyde observations: constraint for isoprene emission estimates over Europe?, Atmos. Chem. Phys., 9, 1647–1664, doi:10.5194/acp-9-1647-2009, 2009b.

Fleischmann, O. C., Hartmann, M., Burrows, J. P., and Orphal, J.: New ultraviolet absorption cross-sections of BrO at atmospheric temperatures measured by time-windowing Fourier transform spectroscopy, J. Photoch. Photobio. A, 168, 117–132, 2004.

Fried, A., McKeen, S., Sewell, S., Harder, J., Henry, B., Goldan, P., Kuster, W., Williams, E., Baumann, K., Shetter, R., and Cantrell, C.: Photochemistry of formaldehyde during the 1993 Tropospheric OH Photochemistry Experiment, J. Geophys. Res.-Atmos., 102, 6283–6296, doi:10.1029/96JD03249, 1997.

Fried, A., Crawford, J., Olson, J., Walega, J., Potter, W., Wert, B., Jordan, C., Anderson, B., Shetter, R., Lefer, B., Blake, D., Blake, N., Meinardi, S., Heikes, B., O'Sullivan, D., Snow, J., Fuelberg, H., Kiley, C. M., Sandholm, S., Tan, D., Sachse, G., Singh, H., Faloona, I., Harward, C. N., and Carmichael, G. R.: Airborne tunable diode laser measurements of formaldehyde during TRACE-P: distributions and box-model comparisons, J. Geophys. Res., 108, 8798, doi:10.1029/2003JD003451, 2003.

Fried, A., Olson, J. R., Walega, J. G., Crawford, J. H., Chen, G., Weibring, P., Richter, D., Roller, C., Tittel, F., Porter, M., Fuelberg, H., Halland, J., Bertram, T. H., Cohen, R. C., Pickering, K., Heikes, B. G., Snow, J. A., Shen, H., O'Sullivan, D. W., Brune, W. H., Ren, X., Blake, D. R., Blake, N., Sachse, G., Diskin, G. S., Podolske, J., Vay, S. A., Shetter, R. E., Hall, S. R., Anderson, B. E., Thornhill, L., Clark, A. D., McNaughton, C. S., Singh, H. B., Avery, M. A., Huey, G., Kim, S., and Millet, D. B.: Role of convection in redistributing formaldehyde to the Upper Troposphere over North America and the North Atlantic during the Summer 2004 INTEX campaign, J. Geophys. Res., 113, D17306, doi:10.1029/2007JD009760, 2008.

Fried, A., Cantrell, C., Olson, J., Crawford, J. H., Weibring, P., Walega, J., Richter, D., Junkermann, W., Volkamer, R., Sinreich, R., Heikes, B. G., O'Sullivan, D., Blake, D. R., Blake, N., Meinardi, S., Apel, E., Weinheimer, A., Knapp, D., Perring, A., Cohen, R. C., Fuelberg, H., Shetter, R. E., Hall, S. R., Ullmann, K., Brune, W. H., Mao, J., Ren, X., Huey, L. G., Singh, H. B., Hair, J. W., Riemer, D., Diskin, G., and Sachse, G.: Detailed comparisons of airborne formaldehyde measurements with box models during the 2006 INTEX-B and MILAGRO campaigns: potential evidence for significant impacts of unmeasured and multi-generation volatile organic carbon compounds, Atmos. Chem. Phys., 11, 11867–11894, doi:10.5194/acp-11-11867-2011, 2011.

Frieß, U., Monks, P. S., Remedios, J. J., Rozanov, A., Sinreich, R., Wagner, T., and Platt, U.: MAX-DOAS O_4 measurements: a new technique to derive information on atmospheric aerosols: 2. Modeling studies, J. Geophys. Res., 111, D14203, doi:10.1029/2005jd006618, 2006.

Fu, T.-M., Jacob, D. J., Palmer, P. I., Chance, K., Wang, Y. X., Barletta, B., Blake, D. R., Stanton, J. C., and Pilling, M. J.: Space-based formaldehyde measurements as constraints on volatile organic compound emissions in east and south Asia and implications for ozone, J. Geophys. Res., 112, D06312, doi:10.1029/2006JD007853, 2007.

Gardiner, T., Forbes, A., de Mazière, M., Vigouroux, C., Mahieu, E., Demoulin, P., Velazco, V., Notholt, J., Blumenstock, T., Hase, F., Kramer, I., Sussmann, R., Stremme, W., Mellqvist, J., Strandberg, A., Ellingsen, K., and Gauss, M.: Trend analysis of greenhouse gases over Europe measured by a network of ground-based remote FTIR instruments, Atmos. Chem. Phys., 8, 6719–6727, doi:10.5194/acp-8-6719-2008, 2008.

Gielen, C., Van Roozendael, M., Hendrick, F., Pinardi, G., Vlemmix, T., De Bock, V., De Backer, H., Fayt, C., Hermans, C., Gillotay, D., and Wang, P.: A simple and versatile cloud-screening method for MAX-DOAS retrievals, Atmos. Meas. Tech., 7, 3509–3527, doi:10.5194/amt-7-3509-2014, 2014.

Grainger, J. and Ring, J.: Anomalous Fraunhofer line profiles, Nature, 193, p. 762, doi:10.1038/193762a0, 1962.

Guenther, A., Karl, T., Harley, P., Wiedinmyer, C., Palmer, P. I., and Geron, C.: Estimates of global terrestrial isoprene emissions using MEGAN (Model of Emissions of Gases and Aerosols from Nature), Atmos. Chem. Phys., 6, 3181–3210, doi:10.5194/acp-6-3181-2006, 2006.

Hak, C., Pundt, I., Trick, S., Kern, C., Platt, U., Dommen, J., Ordóñez, C., Prévôt, A. S. H., Junkermann, W., Astorga-Lloréns, C., Larsen, B. R., Mellqvist, J., Strandberg, A., Yu, Y., Galle, B., Kleffmann, J., Lörzer, J. C., Braathen, G. O., and Volkamer, R.: Intercomparison of four different in-situ techniques for ambient formaldehyde measurements in urban air, Atmos. Chem. Phys., 5, 2881–2900, doi:10.5194/acp-5-2881-2005, 2005.

Harder, J. W., Fried, A., Sewell, S., and Henry, B.: Comparison of tunable diode laser and long-path ultraviolet/visible spectroscopic measurements of ambient formaldehyde concentrations

during the 1993 OH Photochemistry Experiment, J. Geophys. Res., 102, 6267–6282, doi:10.1029/96JD01731, 1997.

Hase, F., Hannigan, J. W., Coffey, M. T., Goldman, A., Höpfner, M., Jones, N. B., Rinsland, C. P., and Wood, S. W.: Intercomparison of retrieval codes used for the analysis of high-resolution, ground-based FTIR measurements, J. Quant. Spectrosc. Ra., 87, 25–52, doi:10.1016/j.jqsrt.2003.12.008, 2004.

Heckel, A., Richter, A., Tarsu, T., Wittrock, F., Hak, C., Pundt, I., Junkermann, W., and Burrows, J. P.: MAX-DOAS measurements of formaldehyde in the Po-Valley, Atmos. Chem. Phys., 5, 909–918, doi:10.5194/acp-5-909-2005, 2005.

Hendrick, F., Müller, J.-F., Clémer, K., Wang, P., De Mazière, M., Fayt, C., Gielen, C., Hermans, C., Ma, J. Z., Pinardi, G., Stavrakou, T., Vlemmix, T., and Van Roozendael, M.: Four years of ground-based MAX-DOAS observations of HONO and NO_2 in the Beijing area, Atmos. Chem. Phys., 14, 765–781, doi:10.5194/acp-14-765-2014, 2014.

Henne, S., Furger, M., Nyeki, S., Steinbacher, M., Neininger, B., de Wekker, S. F. J., Dommen, J., Spichtinger, N., Stohl, A., and Prévôt, A. S. H.: Quantification of topographic venting of boundary layer air to the free troposphere, Atmos. Chem. Phys., 4, 497–509, doi:10.5194/acp-4-497-2004, 2004.

Henne, S., Dommen, J., Neininger, B., Reimann, S., Staehelin, J., and Prévôt, A. S. H.: Influence of mountain venting in the Alps on the ozone chemistry of the lower free troposphere and the European pollution export, J. Geophys. Res., 110, D22307, doi:10.1029/2005JD005936, 2005.

Herndon, S. C., Jayne, J. T., Zahniser, M. S., Worsnop, D. R., Knighton, B., Alwine, E., Lamb, B. K., Zavala, M., Nelson, D. D., McManus, J. B., Shorter, J. H., Canagaratnam, M. R., Onasch, T. B., and Kolb, C. E.: Characterization of urban pollutant emission fluxes and ambient concentration distributions using a mobile laboratory with rapid response instrumentation, Faraday Discuss., 130, 327–339, doi:10.1039/B500411J, 2005.

Hönninger, G., von Friedeburg, C., and Platt, U.: Multi axis differential optical absorption spectroscopy (MAX-DOAS), Atmos. Chem. Phys., 4, 231–254, doi:10.5194/acp-4-231-2004, 2004.

Houweling, S., Dentener, F., and Lelieveld, J.: The impact of nonmethane hydrocarbon compounds on tropospheric photochemistry, J. Geophys. Res.-Atmos., 103, 10673–10696, doi:10.1029/97JD03582, 1998.

Inomata, S., Tanimoto, H., Kameyama, S., Tsunogai, U., Irie, H., Kanaya, Y., and Wang, Z.: Technical Note: Determination of formaldehyde mixing ratios in air with PTR-MS: laboratory experiments and field measurements, Atmos. Chem. Phys., 8, 273–284, doi:10.5194/acp-8-273-2008, 2008.

Irie, H., Takashima, H., Kanaya, Y., Boersma, K. F., Gast, L., Wittrock, F., Brunner, D., Zhou, Y., and Van Roozendael, M.: Eight-component retrievals from ground-based MAX-DOAS observations, Atmos. Meas. Tech., 4, 1027–1044, doi:10.5194/amt-4-1027-2011, 2011.

Jacquemart, D., Laraia, A., Kwabia Tchana, F., Gamache, R. R., Perrin, A., and Lacome, N.: Formaldehyde around 3.5 and 5.7-μm: Measurement and calculation of broadening coefficients, J. Quant. Spectrosc. Ra., 111, 1209–1222, doi:10.1016/j.jqsrt.2010.02.004, 2010.

Jenkin, M. E., Murrellis, T. P., and Passant, N. R.: The temporal dependence of ozone precursor emissions: estimation and application, AEA Technology, Report No. AEAT/R/ENV/0355, Issue 1, 2000.

Jones, N. B., Riedel, K., Allan, W., Wood, S., Palmer, P. I., Chance, K., and Notholt, J.: Long-term tropospheric formaldehyde concentrations deduced from ground-based fourier transform solar infrared measurements, Atmos. Chem. Phys., 9, 7131–7142, doi:10.5194/acp-9-7131-2009, 2009.

Kanakidou, M., Seinfeld, J. H., Pandis, S. N., Barnes, I., Dentener, F. J., Facchini, M. C., Van Dingenen, R., Ervens, B., Nenes, A., Nielsen, C. J., Swietlicki, E., Putaud, J. P., Balkanski, Y., Fuzzi, S., Horth, J., Moortgat, G. K., Winterhalter, R., Myhre, C. E. L., Tsigaridis, K., Vignati, E., Stephanou, E. G., and Wilson, J.: Organic aerosol and global climate modelling: a review, Atmos. Chem. Phys., 5, 1053–1123, doi:10.5194/acp-5-1053-2005, 2005.

Koelemeijer, R. B. A., de Haan, J. F., and Stammes, P.: A database of spectral surface reflectivity in the range 335–772 nm derived from 5.5 years of GOME observations, J. Geophys. Res., 108, 4070, doi:10.1029/2002JD002429, 2003.

Li, Y. S., Campana, M., Reimann, S., Schaub, D., Stemmler, K., Staehelin, J., and Thomas, P. T.: Hydrocarbon concentrations at the Alpine mountain sites Jungfraujoch and Arosa, Atmos. Environ., 39, 1113–1127, doi:10.1016/j.atmosenv.2004.09.084, 2005.

Legreid, G., Folini, D., Staehelin, J., Balzani Lööv, J., Steinbacher, M., and Reimann, S.: Measurements of organic trace gases including oxygenated volatile organic compounds at the high alpine site Jungfraujoch (Switzerland): seasonal variation and source allocations, J. Geophys. Res., 113, D05307, doi:10.1029/2007JD008653, 2008.

Lee, M., Heikes, B. G., Jacob, D. J., Sachse, G., and Anderson, B.: Hydrogen peroxide, organic hydroperoxide, and formaldehyde as primary pollutants from biomass burning, J. Geophys. Res., 102, 1301–1309, doi:10.1029/96JD01709, 1997.

Lee, Y. N., Zhou, X., Kleinman, L. I., Nunnermacker, L. J., Springston, S. R., Daum, P. H., Newman, L., Keigley, W. G., Holdren, M. W., Spicer, C. W., Young, V., Fu, B., Parrish, D. D., Holloway, J., Williams, J., Roberts, J. M., Ryerson, T. B., and Fehsenfeld, F. C.: Atmospheric chemistry and distribution of formaldehyde and several multioxygenated carbonyl compounds during the 1995 Nashville Middle Tennessee Ozone Study, J. Geophys. Res.-Atmos., 103, 22449–22462, doi:10.1029/98JD01251, 1998.

Logan, J. A., Prather, M. J., Wofsy, S. C., and McElroy, M. B.: Tropospheric chemistry: a global perspective, J. Geophys. Res., 86, 7210–7254, doi:10.1029/JC086iC08p07210, 1981.

Lugauer, M., Baltensperger, U., Furger, M., Gäggeler, H. W., Jost, D. T., Nyeki, S., and Schwikowski, M.: Influences of vertical transport and scavenging on aerosol particle surface area and radon decay product concentrations at the Jungfraujoch (3454 m a.s.l.), J. Geophys. Res., 105, 1986–19879, doi:10.1029/2000JD900184, 2000.

Mao, J., Jacob, D. J., Evans, M. J., Olson, J. R., Ren, X., Brune, W. H., Clair, J. M. St., Crounse, J. D., Spencer, K. M., Beaver, M. R., Wennberg, P. O., Cubison, M. J., Jimenez, J. L., Fried, A., Weibring, P., Walega, J. G., Hall, S. R., Weinheimer, A. J., Cohen, R. C., Chen, G., Crawford, J. H., McNaughton, C., Clarke, A. D., Jaeglé, L., Fisher, J. A., Yantosca, R. M., Le Sager, P., and Carouge, C.: Chemistry of hydrogen oxide radicals (HO_x) in

the Arctic troposphere in spring, Atmos. Chem. Phys., 10, 5823–5838, doi:10.5194/acp-10-5823-2010, 2010.

Mao, J., Paulot, F., Jacob, D. J., Cohen, R. C., Crounse, J. D., Wennberg, P. O., Keller, C. A., Hudman, R. C., Barkley, M. P., and Horowitz, L. W.: Ozone and organic nitrates over the eastern United States: Sensitivity to isoprene chemistry, J. Geophys. Res.-Atmos., 118, 11,256–268, doi:10.1002/jgrd.50817, 2013.

Meller, R. and Moortgat, G. K.: Temperature dependence of the absorption cross sections of formaldehyde between 223 and 323 K in the wavelength range 225–375 nm, J. Geophys. Res., 105, 7089–7101, 2000.

Notholt, J., Toon, G., Stordal, F., Solberg, S., Schmidbauer, N., Becker, E., Meier, A., and Sen, B.: Seasonal variations of atmospheric trace gases in the high Arctic at 79 ° N, J. Geophys. Res., 102, 12855–12861, doi:10.1029/97JD00337, 1997.

Park, R. J., Jacob, D. J., Field, B. D., Yantosca, R. M., and Chin, M.: Natural and transboundary pollution influences on sulfate-nitrate-ammonium aerosols in the United States: implications for policy, J. Geophys. Res., 109, D15204, doi:10.1029/2003JD004473, 2004.

Peeters, J. and Müller, J.-F.: HO_x radical regeneration in isoprene oxidation via peroxy radical isomerisations. II: Experimental evidence and global impact, Phys. Chem. Chem. Phys., 12, 14227–14235, 2010.

Peeters, J., Müller, J.-F., Stavrakou, T., and Nguyen, S. V.: Hydroxyl radical recycling in isoprene oxidation driven by hydrogen bonding and hydrogen tunneling: the upgraded LIM1 mechanism, J. Phys. Chem., 118, 8625–8643, doi:10.1021/jp5033146, 2014.

Perrin, A., Jacquemart, D., Kwabia Tchanab, F., and Lacome, N.: Absolute line intensities measurements and calculations for the 5.7 and 3.6 µm bands of formaldehyde, J. Quant. Spectrosc. Ra., 110, 700–716, doi:10.1016/j.jqsrt.2008.11.005, 2009.

Pikelnaya, O., Hurlock, S. C., Trick, S., and Stutz, J.: Intercomparison of multiaxis and long-path optical absorption spectroscopy measurements in the marine boundary layer, J. Geophys. Res., 112, D10S01, doi:10.1029/2006JD007727, 2007.

Pinardi, G., Van Roozendael, M., Abuhassan, N., Adams, C., Cede, A., Clémer, K., Fayt, C., Frieß, U., Gil, M., Herman, J., Hermans, C., Hendrick, F., Irie, H., Merlaud, A., Navarro Comas, M., Peters, E., Piters, A. J. M., Puentedura, O., Richter, A., Schönhardt, A., Shaiganfar, R., Spinei, E., Strong, K., Takashima, H., Vrekoussis, M., Wagner, T., Wittrock, F., and Yilmaz, S.: MAX-DOAS formaldehyde slant column measurements during CINDI: intercomparison and analysis improvement, Atmos. Meas. Tech., 6, 167–185, doi:10.5194/amt-6-167-2013, 2013.

Platt, U. and Stutz, J.: Differential Optical Absorption Spectroscopy (DOAS): principles and Applications, ISBN 978-3-540-21193-8, Springer, Berlin-Heidelberg, Germany, 2008.

Possanzini, M., Di Palo, V., and Ceccinato, A.: Sources and photodecomposition of formaldehyde and acetaldehyde in Rome ambient air, Atmos. Environ., 36, 3195–3201, doi:10.1016/S1352-2310(02)00192-9, 2002.

Pukīte, J., Kühl, S., Deutschmann, T., Platt, U., and Wagner, T.: Extending differential optical absorption spectroscopy for limb measurements in the UV, Atmos. Meas. Tech., 3, 631–653, doi:10.5194/amt-3-631-2010, 2010.

Reimann, S., Schaub, D., Stemmler, K., Folini, D., Hill, M., Hofer, P., Buchmann, B., Simmonds, P. G., Greally, B. R., and O'Doherty, S.: Halogenated greenhouse gases at the Swiss High Alpine Site of Jungfraujoch (3580 m a.s.l.): continuous measurements and their use for regional European source allocation, J. Geophys. Res., 109, D05307, doi:10.1029/2003JD003923, 2004.

Rinsland, C. P., Jones, N. B., Connor, B. J., Logan, J. A., Pougatchev, N. S., Goldman, A., Murcray, F. J., Stephen, T. M., Pine, A. S., Zander, R., Mahieu, E., and Demoulin, P.: Northern and Southern Hemisphere ground-based infrared spectroscopic measurements of tropospheric carbon monoxide and ethane, J. Geophys. Res., 103, 28197–28217, doi:10.1029/98JD02515, 1998.

Rodgers, C. D.: Inverse Methods for Atmospheric Sounding: Theory and Practice, Series on Atmospheric, Oceanic and Planetary Physics, Vol. 2, World Scientific Publishing Co., Singapore, 2000.

Rodgers, C. D. and Connor, B. J.: Intercomparison of remote sounding instruments, J. Geophys. Res., 108, 4116–4129, doi:10.1029/2002JD002299, 2003.

Rothman, L. S.: AFGL Atmospheric absorption line parameters compilation: 1980 version, Appl. Optics, 20, 791–795, doi:10.1021/jp5033146, 1981.

Rothman, L. S., Gordon, I. E., Barbe, A., Benner, D. C., Bernath, P. F., Birk, M., Boudon, V., Brown, L. R., Campargue, A., Champion, J.-P., Chance, K., Coudert, L. H., Danaj, V., Devi, V. M., Fally, S., Flaud, J.-M., Gamache, R. R., Goldmanm, A., Jacquemart, D., Kleiner, I., Lacome, N., Lafferty, W. J., Mandin, J.-Y., Massie, S. T., Mikhailenko, S. N., Miller, C. E., Moazzen-Ahmadi, N., Naumenko, O. V., Nikitin, A. V., Orphal, J., Perevalov, V. I., Perrin, A., Predoi-Cross, A., Rinsland, C. P., Rotger, M., Simeckova, M., Smith, M. A. H., Sung, K., Tashkun, S. A., Tennyson, J., Toth, R. A., Vandaele, A. C., and Vander Auwera, J.: The Hitran 2008 molecular spectroscopic database, J. Quant. Spectrosc. Ra., 110, 533–572, doi:10.1016/j.jqsrt.2009.02.013, 2009.

Rothman, L. S., Gordon, I. E., Babikov, Y., Barbe, A., Chris Benner, D., Bernath, P. F., Birk, M., Bizzocchi, L., Boudon, V., Brown, L. R., Campargue, A., Chance, K., Cohen, E. A., Coudert, L. H., Devi, V. M., Drouin, B. J., Fayt, A., Flaud, J.-M., Gamache, R. R., Harrison, J. J., Hartmann, J.-M., Hill, C., Hodges, J. T., Jacquemart, D., Jolly, A., Lamouroux, J., Le Roy, R. J., Li, G., Long, D. A., Lyulin, O. M., Mackie, C. J., Massie, S. T., Mikhailenko, S., Müller, H. S. P., Naumenko, O. V., Nikitin, A. V., Orphal, J., Perevalov, V., Perrin, A., Polovtseva, E. R., Richard, C., Smith, M. A. H., Starikova, E., Sung, K., Tashkun, S., Tennyson, J., Toon, G. C., Tyuterev, Vl. G., and Wagner, G.: The HITRAN2012 molecular spectroscopic database, J. Quant. Spectrosc. Ra., 130, 4–50, doi:10.1016/j.jqsrt.2013.07.002, 2013.

Schultz, M. G., Backman, L., Balkanski, Y., Bjoerndalsaeter, S., Brand, R., Burrows, J. P., Dalsøren, S., de Vasconcelos, L., Grodtmann, B., Hauglustaine, D. A., Heil, A., Hoelzemann, J. J., Isaksen, I. S. A., Kaurola, J., Knorr, W., Ladstaetter-Weißenmayer, A., Mota, B., Oom, D., Pacyna, J., Panasiuk, D., Pereira, J. M. C., Pulles, T., Pyle, J., Rast, S., Richter, A., Savage, N., Scnadt, C., Schulz, M., Spessa, A., Staehelin, J., Sundet, J. K., Szopa, S., Thonicke, K., van het Bolscher, M., van Noije, T., van Velthoven, P., Vik, A. F., and Wittrock, F.: REanalysis of the TROpospheric chemical composition of the past 40 years (RETRO): a long-term global modeling study of tropospheric chemistry, Jülich/Hamburg, Germany, 48/2007 report

on Earth System Science of the Max Planck Institute for Meteorology, Hamburg, Germany, ISSN 1614–1199, available at: http://retro.enes.org (last access: 17 July 2014), 2007.

Shettle, E. P.: Models of aerosols, clouds, and precipitation for atmospheric propagation studies, in: NATO AGARD Conference Proceedings No. 454: Atmospheric propagation in the UV, visible, IR and mm-region and related system aspects, 9–13 October 1989, Neuilly sur Seine, France, 1989.

Simpson, D., Michael Gauss, S. T., and Valdebenito, A.: Model Updates Transboundary acidification, eutrophication and ground level ozone in Europe EMEP Status Report 1/2010, The Norwegian Meteorological Institute, Oslo, Norway, 2010.

Spurr, R., LIDORT and VLIDORT: Linearized Pseudo-Spherical Scalar and Vector Discrete Ordinate Radiative Transfer Models for Use in Remote Sensing Retrieval Problems, Light Scattering Reviews, Vol. 3, edited by: Kokhanovsky, A., Springer, Berlin Heidelberg, Germany, 2008.

Sussmann, R., Borsdorff, T., Rettinger, M., Camy-Peyret, C., Demoulin, P., Duchatelet, P., Mahieu, E., and Servais, C.: Technical Note: Harmonized retrieval of column-integrated atmospheric water vapor from the FTIR network – first examples for long-term records and station trends, Atmos. Chem. Phys., 9, 8987–8999, doi:10.5194/acp-9-8987-2009, 2009.

Staffelbach, T., Neftel, A., Stauffer, B., and Jacob, D. J.: A record of the atmospheric methane sink from formaldehyde in polar ice cores, Nature, 349, 603–605, doi:10.1038/349603a0, 1991.

Starokozhev, E., Fries, E., Cycura, A., and Püttmann, W.: Distribution of VOCs between air and snow at the Jungfraujoch high alpine research station, Switzerland, during CLACE 5 (winter 2006), Atmos. Chem. Phys., 9, 3197–3207, doi:10.5194/acp-9-3197-2009, 2009.

Stavrakou, T., Müller, J.-F., De Smedt, I., Van Roozendael, M., van der Werf, G. R., Giglio, L., and Guenther, A.: Global emissions of non-methane hydrocarbons deduced from SCIAMACHY formaldehyde columns through 2003–2006, Atmos. Chem. Phys., 9, 3663–3679, doi:10.5194/acp-9-3663-2009, 2009a.

Stavrakou, T., Müller, J.-F., De Smedt, I., Van Roozendael, M., van der Werf, G. R., Giglio, L., and Guenther, A.: Evaluating the performance of pyrogenic and biogenic emission inventories against one decade of space-based formaldehyde columns, Atmos. Chem. Phys., 9, 1037–1060, doi:10.5194/acp-9-1037-2009, 2009b.

Stavrakou, T., Guenther, A., Razavi, A., Clarisse, L., Clerbaux, C., Coheur, P.-F., Hurtmans, D., Karagulian, F., De Mazière, M., Vigouroux, C., Amelynck, C., Schoon, N., Laffineur, Q., Heinesch, B., Aubinet, M., Rinsland, C., and Müller, J.-F.: First space-based derivation of the global atmospheric methanol emission fluxes, Atmos. Chem. Phys., 11, 4873–4898, doi:10.5194/acp-11-4873-2011, 2011.

Stavrakou, T., Müller, J.-F., Boersma, K. F., van der A, R. J., Kurokawa, J., Ohara, T., and Zhang, Q.: Key chemical NO_x sink uncertainties and how they influence top-down emissions of nitrogen oxides, Atmos. Chem. Phys., 13, 9057–9082, doi:10.5194/acp-13-9057-2013, 2013.

Stavrakou, T., Müller, J.-F., Bauwens, M., De Smedt, I., Van Roozendael, M., Guenther, A., Wild, M., and Xia, X.: Isoprene emissions over Asia 1979–2012: impact of climate and land-use changes, Atmos. Chem. Phys., 14, 4587–4605, doi:10.5194/acp-14-4587-2014, 2014.

Stickler, A., Fischer, H., Williams, J., de Reus, M., Sander, R., Lawrence, M. G., Crowley, J. N., and Lelieveld, J.: Influence of summertime deep convection on formaldehyde in the middle and upper troposphere over Europe, J. Geophys. Res., 111, D14308, doi:10.1029/2005JD007001, 2006.

Tan, D., Faloona, I., Simpas, J. B., Brune, W., Shepson, P. B., Couch, T. L., Sumner, A. L., Carroll, M. A., Thornberry, T., Apel, E., Riemer, D., and Stockwell, W.: HO_x budgets in a deciduous forest: results from the PROPHET summer 1998 campaign, J. Geophys. Res.-Atmos., 106, 24407–24427, doi:10.1029/2001JD900016, 2001.

Tejwani, G. D. T. and Yeung, E. S.: Pressure-broadened linewidths of formaldehyde, J. Chem. Phys., 66, 4915–4918, doi:10.1063/1.433830, 1977.

Thalman, R. and Volkamer, R.: Temperature dependent absorption cross-sections of O_2-O_2 collision pairs between 340 and 630 nm at atmospherically relevant pressure, Phys. Chem. Chem. Phys., 15, 15371–15381, doi:10.1039/C3CP50968K, 2013.

Vandaele, A. C., Hermans, C., Simon, P. C., Carleer, M., Colin, R., Fally, S., Merienne, M.-F., Jenouvrier, A., and Coquart, B.: Measurements of the NO_2 absorption cross-section from 42 000 cm^{-1} to 10 000 cm^{-1} (238–1000 nm) at 220 K and 294 K, J. Quant. Spectrosc. Ra., 59, 171–184, doi:10.1016/S0022-4073(97)00168-4, 1998.

van der Werf, G. R., Randerson, J. T., Giglio, L., Collatz, G. J., Mu, M., Kasibhatla, P. S., Morton, D. C., DeFries, R. S., Jin, Y., and van Leeuwen, T. T.: Global fire emissions and the contribution of deforestation, savanna, forest, agricultural, and peat fires (1997–2009), Atmos. Chem. Phys., 10, 11707–11735, doi:10.5194/acp-10-11707-2010, 2010.

van Donkelaar, A., Martin, R. V., Leaitch, W. R., Macdonald, A. M., Walker, T. W., Streets, D. G., Zhang, Q., Dunlea, E. J., Jimenez, J. L., Dibb, J. E., Huey, L. G., Weber, R., and Andreae, M. O.: Analysis of aircraft and satellite measurements from the Intercontinental Chemical Transport Experiment (INTEX-B) to quantify long-range transport of East Asian sulfur to Canada, Atmos. Chem. Phys., 8, 2999–3014, doi:10.5194/acp-8-2999-2008, 2008.

Viatte, C., Strong, K., Walker, K. A., and Drummond, J. R.: Five years of CO, HCN, C_2H_6, C_2H_2, CH_3OH, HCOOH and H_2CO total columns measured in the Canadian high Arctic, Atmos. Meas. Tech., 7, 1547–1570, doi:10.5194/amt-7-1547-2014, 2014.

Vigouroux, C., Hendrick, F., Stavrakou, T., Dils, B., De Smedt, I., Hermans, C., Merlaud, A., Scolas, F., Senten, C., Vanhaelewyn, G., Fally, S., Carleer, M., Metzger, J.-M., Müller, J.-F., Van Roozendael, M., and De Mazière, M.: Ground-based FTIR and MAX-DOAS observations of formaldehyde at Réunion Island and comparisons with satellite and model data, Atmos. Chem. Phys., 9, 9523–9544, doi:10.5194/acp-9-9523-2009, 2009.

Wagner, T., Dix, B., von Friedeburg, C., Friess, U., Sanghavi, S., Sinreich, R., and Platt, U.: MAX-DOAS O_4 measurements: A new technique to derive information on atmospheric aerosols – principles and information content, J. Geophys. Res., 109, D22205, doi:10.1029/2004jd004904, 2004.

Wagner, T., Deutschmann, T., and Platt, U.: Determination of aerosol properties from MAX-DOAS observations of the Ring effect, Atmos. Meas. Tech., 2, 495–512, doi:10.5194/amt-2-495-2009, 2009.

Wagner, T., Beirle, S., Brauers, T., Deutschmann, T., Frieß, U., Hak, C., Halla, J. D., Heue, K. P., Junkermann, W., Li, X., Platt, U., and Pundt-Gruber, I.: Inversion of tropospheric profiles of aerosol extinction and HCHO and NO_2 mixing ratios from MAX-DOAS observations in Milano during the summer of 2003 and comparison with independent data sets, Atmos. Meas. Tech., 4, 2685–2715, doi:10.5194/amt-4-2685-2011, 2011.

Wang, T., Hendrick, F., Wang, P., Tang, G., Clémer, K., Yu, H., Fayt, C., Hermans, C., Gielen, C., Müller, J.-F., Pinardi, G., Theys, N., Brenot, H., and Van Roozendael, M.: Evaluation of tropospheric SO_2 retrieved from MAX-DOAS measurements in Xianghe, China, Atmos. Chem. Phys., 14, 11149–11164, doi:10.5194/acp-14-11149-2014, 2014.

Wittrock, F., Richter, A., Oetjen, H., Burrows, J. P., Kanakidou, M., Myriokefalitakis, S., Volkamer, R., Beirle, S., Platt, U., and Wagner, T.: Simultaneous global observations of glyoxal and formaldehyde from space, Geophys. Res. Lett., 33, L16804, doi:10.1029/2006GL026310, 2006.

Xiao, Y., Logan, J. A., Jacob, D. J., Hudman, R. C., Yantosca, R., and Blake, D. R.: Global budget of ethane and regional constraints on U. S. sources, J. Geophys. Res., 113, D21306, doi:10.1029/2007JD009415, 2008.

Zander, R., Mahieu, E., Demoulin, P., Duchatelet, P., Roland, G., Servais, C., Mazière, M. D., Reimann, S., and Rinsland, C. P.: Our changing atmosphere: evidence based on long-term infrared solar observations at the Jungfraujoch since 1950, Sci. Total Environ., 391, 184–195, doi:10.1016/j.scitotenv.2007.10.018, 2008.

Zellweger, C., Forrer, J., Hofer, P., Nyeki, S., Schwarzenbach, B., Weingartner, E., Ammann, M., and Baltensperger, U.: Partitioning of reactive nitrogen (NO_y) and dependence on meteorological conditions in the lower free troposphere, Atmos. Chem. Phys., 3, 779–796, doi:10.5194/acp-3-779-2003, 2003.

Supplement of Atmos. Chem. Phys. Discuss., 15, 31287–31333, 2015
http://www.atmos-chem-phys-discuss.net/15/31287/2015/
doi:10.5194/acpd-15-31287-2015-supplement

Atmospheric Chemistry and Physics Discussions

Supplement of

Diurnal cycle and multi-decadal trend of formaldehyde in the remote atmosphere near 46° N

B. Franco et al.

Correspondence to: B. Franco (bruno.franco@ulg.ac.be)

Table S1. Monthly parameters determined by adjusting the fitting parametric model (Eq. 1) to the observed monthly intra-day cycles of HCHO total column above Jungfraujoch, on the basis of the 1995 – 2015/06 BRUKER data set. The modelled intra-day variations represented in Figs. 1 and 3a may be reproduced by including these parameters in Eq. 1.

	a	**b**	**c**	$\mathbf{x_0}$
January	1.138E+15	209.919	43.581	12.826
February	1.181E+15	11.982	2.454	12.749
March	1.441E+15	13.507	2.835	12.615
April	1.736E+15	26.432	4.663	12.561
May	2.148E+15	18.963	2.850	12.859
June	2.520E+15	33.567	4.410	13.108
July	2.701E+15	204.648	23.096	12.682
August	2.644E+15	33.803	4.203	12.253
September	2.204E+15	17.361	2.378	12.304
October	1.846E+15	13.844	1.905	12.634
November	1.459E+15	3.068E+06	5.481E+05	12.074
December	1.186E+15	113.108	20.708	12.036

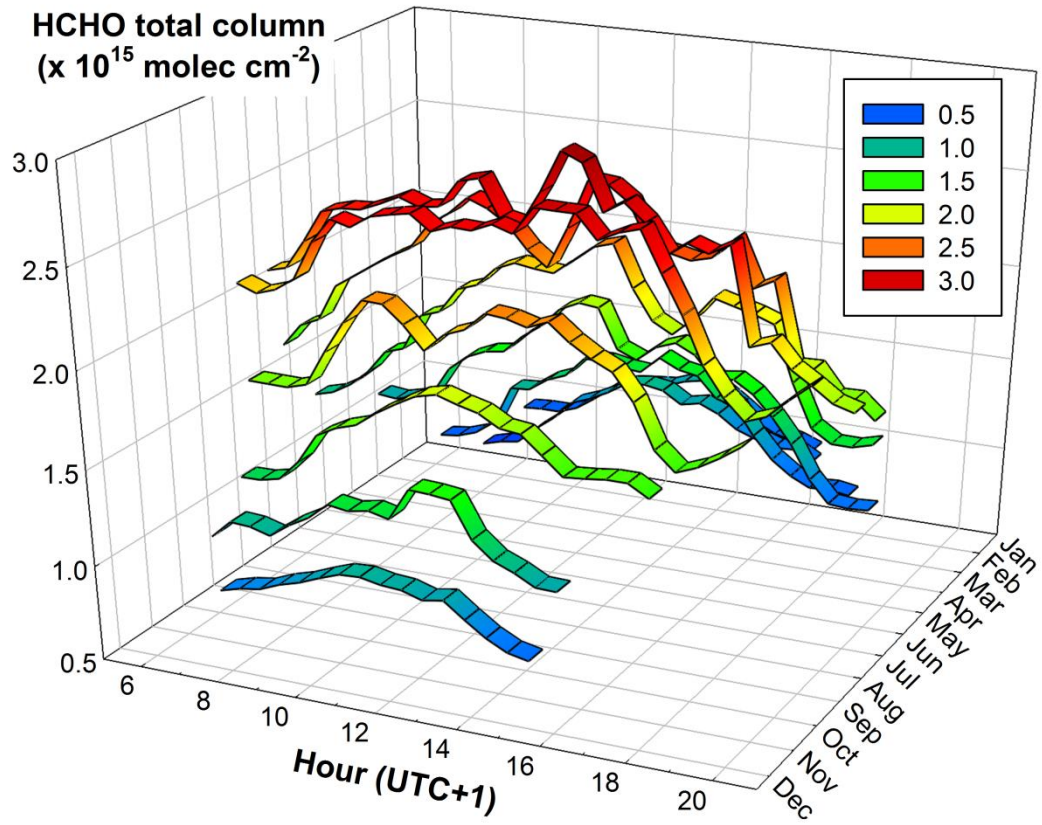

Figure S1. Monthly intra-day variation of HCHO total column, represented by the running average of the HCHO total columns (in molec cm^{-2}) derived from all individual observations made by the Bruker instrument between 1995 and June 2015 at the ISSJ. It is expressed according to the hour of the day and for each month of the year. The running average corresponds to a 0.5 h time step and a 1.5 h-wide integration length.

Atmos. Chem. Phys. Discuss., 15, 31287–31333, 2015
www.atmos-chem-phys-discuss.net/15/31287/2015/
doi:10.5194/acpd-15-31287-2015

Atmospheric Chemistry and Physics Discussions

Diurnal cycle and multi-decadal trend of formaldehyde in the remote atmosphere near 46° N

B. Franco[1], E. A. Marais[2], B. Bovy[1], W. Bader[1], B. Lejeune[1], G. Roland[1], C. Servais[1], and E. Mahieu[1]

[1]Institute of Astrophysics and Geophysics of the University of Liège, Liège, Belgium
[2]School of Engineering and Applied Sciences, Harvard University, Cambridge, MA, USA

Received: 28 September 2015 – Accepted: 30 October 2015 – Published: 9 November 2015

Correspondence to: B. Franco (bruno.franco@ulg.ac.be)

Published by Copernicus Publications on behalf of the European Geosciences Union.

Abstract

Only very few long-term trends of formaldehyde (HCHO) exist. Furthermore, many uncertainties remain as to its diurnal cycle, representing a large short-term variability superimposed on seasonal and inter-annual variations that should be accounted for when comparing ground-based observations to e.g., model results. In this study, we derive a multi-decadal time series (January 1988–June 2015) of HCHO total columns from ground-based high-resolution Fourier transform infrared (FTIR) solar spectra recorded at the high-altitude station of Jungfraujoch (Swiss Alps, 46.5° N, 8.0° E, 3580 m a.s.l.), allowing for the characterization of the mid-latitudinal atmosphere for background conditions. First we investigate the HCHO diurnal variation, peaking around noontime and mainly driven by the intra-day insolation modulation and methane (CH_4) oxidation. We also characterize quantitatively the diurnal cycles by adjusting a parametric model to the observations, which links the daytime to the HCHO columns according to the monthly intra-day regimes. It is then employed to scale all the individual FTIR measurements on a given daytime in order to remove the effect of the intra-day modulation for improving the trend determination and the comparison with HCHO columns simulated by the state-of-the-art chemical transport model GEOS-Chem v9-02. Such a parametric model will be useful to scale the Jungfraujoch HCHO columns on satellite overpass times in the framework of future calibration/validation efforts of space borne sensors. GEOS-Chem sensitivity tests suggest then that the seasonal and inter-annual HCHO column variations above Jungfraujoch are predominantly led by the atmospheric CH_4 oxidation, with a maximum contribution of 25 % from the anthropogenic non-methane volatile organic compound precursors during wintertime. Finally, trend analysis of the so-scaled 27 year FTIR time series reveals a long-term evolution of the HCHO columns in the remote troposphere to be related with the atmospheric CH_4 fluctuations and the short-term OH variability: $+2.9\,\%\,yr^{-1}$ between 1988 and 1995, $-3.7\,\%\,yr^{-1}$ over 1996–2002 and $+0.8\,\%\,yr^{-1}$ from 2003 onwards.

ACPD
15, 31287–31333, 2015

1 Introduction

Formaldehyde (HCHO) is the most abundant aldehyde and one of the highest reactive species in the Earth's atmosphere, with a midday lifetime on the order of a few hours (Logan et al., 1981; Possanzini et al., 2002). Being a product of the oxidation of most of the volatile organic compounds (VOCs), HCHO plays a primary role in tropospheric chemistry and in the control of air quality. Besides dry and wet deposition of generally lesser importance (Atkinson, 2000), HCHO is predominantly removed from the atmosphere via catalytic pathways that are photochemically driven (Luecken et al., 2012). Indeed, large losses occur when HCHO reacts with the hydroxyl radicals (OH) available in the atmosphere to yield water vapor (H_2O) and the HCO radical. By consuming OH, the main sink of methane (CH_4) in the troposphere, the HCHO abundance contributes to increasing the lifetime of this major greenhouse gas. HCHO also decomposes by photolysis either in H_2 (molecular hydrogen) and CO (carbon monoxide) or in H (hydrogen) and HCO. Since HCO reacts with oxygen, all these catalytic pathways release CO and hydrogen oxides (HO_x), making HCHO a key component in the production of CO by oxidation of hydrocarbons (Cantrell et al., 1990; Anderson et al., 1996; Calvert et al., 2000; Fried et al., 2002). As HO_x radicals are major oxidizers in the atmosphere, HCHO also constitutes a useful tracer of the atmospheric oxidative capacity (Staffelbach et al., 1991). Moreover, in the presence of sufficient amounts of nitrogen oxides (NO_x), for instance in polluted air masses over urban areas (Hak et al., 2005), the HO_x produced by the HCHO removal processes converts nitric oxide to nitrogen dioxide, which results in a net production of tropospheric ozone by photolysis (O_3; Cantrell et al., 1990; Houweling et al., 1998; Hak et al., 2005; Kanakidou et al., 2005).

On the global scale, CH_4 oxidation by OH constitutes the main source throughout the background troposphere, accounting for more than half of the overall production, while the remainder generally results from the oxidation of most of the non-methane VOCs (NMVOCs). However, where strong NMVOC emissions take place over continents, the oxidation of these compounds can dominate the methane-originated HCHO produc-

ACPD
15, 31287–31333, 2015

tion, especially in the continental boundary layer (Millet et al., 2008; Pfister et al., 2008; Dufour et al., 2009a, b; Stavrakou et al., 2009a, b). Among the NMVOCs emitted over continents, biogenic compounds are dominant during the growing season of vegetation, providing ∼ 85 % of the total emissions with the largest contribution coming from isoprene (e.g., Palmer et al., 2003, 2006; Millet et al., 2008). Global HCHO production from anthropogenic NMVOCs is relatively reduced, but is significantly enhanced over largely populated and industrialized areas. NMVOCs from pyrogenic sources (mainly biomass burning) generally provide small HCHO contributions on the global scale, although fire events can enhance HCHO emissions in specific areas (see e.g., Vigouroux et al., 2009). In addition, only a negligible fraction of HCHO (< 1 %) results from direct emissions to the atmosphere by various sources such as biomass burning, vegetation or incomplete fossil fuel combustion (e.g., Carlier et al., 1986; Lee et al., 1997; Hak et al., 2005; Herndon et al., 2005; Fu et al., 2007; De Smedt et al., 2010).

Formaldehyde has already been intensely observed, using measurements obtained from in situ instruments (e.g., de Serves, 1994; DiGangi et al., 2011, 2012), aircraft campaigns (e.g., Fried et al., 2002, 2008, 2011; Frost et al., 2002; Wert et al., 2003) and various satellite sensors (e.g., Chance et al., 2000; Wittrock et al., 2006; Dufour et al., 2009a, b; Stavrakou et al., 2009a, b, 2015; De Smedt et al., 2010, 2015; Marais et al., 2012, 2014), as well as ground-based remote measurements derived from UV-Visible passive Multi-AXis Differential Optical Absorption Spectroscopy (MAX-DOAS) instruments (e.g., Heckel et al., 2005; Pikelnaya et al., 2007; Inomata et al., 2008; Irie et al., 2011; Wagner et al., 2011; Pinardi et al., 2013; Franco et al., 2015b) and from high-resolution infrared solar spectra recorded with Fourier Transform InfraRed (FTIR) spectrometers (e.g., Mahieu et al., 1997; Notholt et al., 1997; Jones et al., 2009; Vigouroux et al., 2009; Paton-Walsh et al., 2010; Viatte et al., 2014; Franco et al., 2015b). However, few long-term trends of HCHO loadings exist, particularly due to the lack of extended consistent data sets. Offering regular and quasi global geographical sampling of the Earth's atmosphere, UV-Vis satellite sensors such as SCIAMACHY (SCanning Imaging Absorption spectroMeter for Atmospheric CHartographY),

ACPD
15, 31287–31333, 2015

GOME, GOME-2 (Global Ozone Monitoring Experiment) and OMI (Ozone Monitoring Instrument), provide some sensitivity in the free troposphere and have been used recently to produce regional decadal trends of HCHO columns at the global scale (De Smedt et al., 2010, 2015). Nonetheless, most space borne observational campaigns are time-limited, added to the fact that such measurements can be considerably affected by instrumental ageing as well as by noise and error sources in the lowermost atmospheric layers, where lies the bulk of HCHO.

Although the seasonal intra-day variation of HCHO has been studied in field campaigns in different environments (Junkermann, 2009; Choi et al., 2010; MacDonald et al., 2012) or using ground-based MAX-DOAS and space borne UV-Vis measurements at various locations (De Smedt et al., 2015; Stavrakou et al., 2015), consistent diurnal observations of HCHO columns remain sparse and time-limited. Hence the uncertainties on the intra-day cycle remain high, added to the fact that the diurnal pattern of HCHO may vary considerably from site to site according to many local factors, such as the emissions of NMVOC precursors, the chemical regime and the influence of the planetary boundary layer. More particularly, the HCHO diurnal cycle may be responsible for significant short-term variability that needs to be accounted for when comparing results derived from space borne instruments, according to their respective overpass times. Furthermore, the HCHO intra-day modulation remains incompletely captured by the chemistry transport models (CTMs), especially for remote conditions (Stavrakou et al., 2015). Therefore, the characterization of the HCHO diurnal cycle using high-quality ground-based observations is definitely required for validation/calibration efforts of satellite sensors and models.

Ground-based instruments, such as the high-resolution FTIR spectrometers distributed worldwide at strategic locations and part of the Network for the Detection of Atmospheric Climate Change (NDACC; see http://ndacc.org), are important contributors to the monitoring of the Earth's atmosphere. An optimized retrieval strategy has been recently developed to derive HCHO total columns from ground-based FTIR solar spectra recorded at the high-altitude NDACC station of Jungfraujoch (Swiss Alps, 46.5° N,

ACPD
15, 31287–31333, 2015

8.0° E, 3580 m a.s.l.). The results have been successfully validated against MAX-DOAS measurements and simulation of two CTMs, GEOS-Chem (Goddard Earth Observing System – chemical transport model; Bey et al., 2001) and IMAGES v2 (Intermediate Model of Annual and Global Evolution of Species; Stavrakou et al., 2013), over the 2010–2012 time period (Franco et al., 2015b). The Jungfraujoch FTIR observational database covers now more than 30 years (back to 1988 in the case of HCHO observations) and is unique worldwide in terms of the quality and density of the measurements as well as of their temporal coverage. Time series of high-quality geophysical data derived from this database are particularly appropriate for multi-decadal studies of many important constituents of the Earth's atmosphere, including HCHO and its VOC precursors. Used as comparative and complementary data, they are also of crucial importance for the calibration and validation of models as well as of current and future satellite sensors.

In the present study, we use the observational database of ground-based solar spectra recorded by two high-resolution FTIR spectrometers operated at the Jungfraujoch station, in order to produce a 27 year time series of HCHO total column (from 1988 to mid-2015). To our best knowledge, it represents the longest time series of remote HCHO measurements. We first investigate the intra-day variation of HCHO total columns in the remote troposphere, using a consistent subset of observations spanning more than twenty years. As this 20 year subset provides robust statistics without inducing errors and/or biases resulting from the use of different sources of measurements, we also characterize the HCHO diurnal cycle on a monthly basis by adjusting a fitting parametric model to the observed intra-day variations. These parameters being determined according to the observations, we employ this model to scale all individual HCHO measurements of the entire Jungfraujoch database at a given moment of the day with the aim of removing the effect of intra-day variability in the HCHO time series. Such a parametric model will be useful for carrying out comparisons between ground-based FTIR and space borne UV-Vis HCHO columns, at the overpass time specific to each satellite sensor (e.g., 09:30 LT for GOME-2B and 13:30 LT for OMI).

ACPD
15, 31287–31333, 2015

In the second part of this study, we employ simulations made with the state-of-the-art 3-D CTM GEOS-Chem to investigate the main sources and drivers of HCHO above Jungfraujoch. First we compare the ground-based FTIR observations with HCHO total columns simulated by the CTM, taking into account the vertical resolution and specific sensitivity of the FTIR retrievals. Then sensitivity runs are performed with the aim of evaluating the contribution of different precursor species or source category (from anthropogenic, biogenic and biomass burning sources) to the HCHO loadings and seasonality.

Finally, we analyze the multi-decadal FTIR time series of the Jungfraujoch station (1988–2015) in order to study the inter-annual variability and deduce trends of HCHO columns in the remote troposphere of the mid-latitudinal Northern Hemisphere.

This paper is organized as follows: we briefly introduce in Sect. 2 the FTIR instrumental setups and data sets, as well as the GEOS-Chem model. In Sect. 3, we investigate the HCHO diurnal variation, describe the fitting parametric model and how it is adjusted to the observations. We report in Sect. 4 the results of the comparison between FTIR measurements and GEOS-Chem simulations, as well as of the sensitivity runs. Section 5 is devoted to the analysis of the 1988–2015 time series of HCHO total columns above the Jungfraujoch station, involving trends determination. Section 6 concludes this study with discussions of the results and identifies avenues for future work.

2 Data sets

2.1 FTIR instrumentation and measurements

The long-term HCHO time series presented and investigated in this study has been produced from the analysis of solar spectra recorded between January 1988 and June 2015 under clear-sky conditions at the high-altitude International Scientific Station of the Jungfraujoch (hereafter ISSJ; Swiss Alps, 46.5° N, 8.0° E, 3580 m a.s.l.). These spectra were recorded using two very high spectral resolution FTIR spectrometers.

ACPD
15, 31287–31333, 2015

A "home-made" instrument was primarily in operation until the mid-1990s and then progressively replaced by a more sensitive commercial Bruker-120 HR instrument. A thorough description of the instrumentation is given by Zander et al. (2008). The consistency among the HCHO columns retrieved from the two subsets is evaluated in Sect. 5.1 using all available coincident measurement days of 1995–1997.

The ISSJ is mainly located in the free troposphere during winter and represents a unique site to study the atmospheric background conditions over central Europe. During the rest of the year, injections of air masses from the planetary boundary layer can occur, bringing biogenic and anthropogenic pollutants from the nearby valleys. Furthermore, the very high dryness due to the altitude, combined to the presence of the Aletsch Glacier (adding to the local dryness) in the immediate vicinity of the station, limits significantly the interference by water vapor in the infrared solar measurements. More details regarding the measurement site can be found in Zander et al. (2008) and Franco et al. (2015b), as well as in references therein.

The overall database investigated here consists of 10 979 solar spectra, of which 1436 were recorded by the "home-made" spectrometer over the 1988–1997 period and 9542 were obtained with the Bruker instrument between 1995 and June 2015 (referred to below as the LIEGE and BRUKER data sets, respectively), both equipped with indium antimonide (InSb) cooled detectors. The spectra were recorded using optical filters maximizing the signal-to-noise (S/N) ratio over the 2400–3310 cm^{-1} spectral domain, thus encompassing the ν_1 infrared band of HCHO centered at 2783 cm^{-1}. The typical spectral resolution (defined here as twice the maximum optical path difference) alternates between 0.003 and 0.005 cm^{-1} for both instruments, with the highest resolution adopted for minimum variation of the airmass and observing geometry, predominantly around midday. S/N ratios vary between 550 to more than 3100 (average spectra resulting from several successive individual scans).

The retrieval strategy applied to both spectral data sets is the one developed and described by Franco et al. (2015b). A short summary of this strategy is given in Table 1. Characterization of the FTIR retrievals indicates a sensitivity throughout the tro-

ACPD
15, 31287–31333, 2015

posphere (up to 12 km altitude). The mean Degree Of Freedom for Signal (DOFS) over the entire data set is ∼ 1, hence only total columns of HCHO may be obtained. In addition, the individual observations characterized by a DOFS value lower than 0.35 have been discarded. Franco et al. (2015b) also provides a complete error budget of the HCHO measurements, quoting the total systematic and random components at ±14 and ±21 %, respectively.

2.2 GEOS-Chem simulations and processing

GEOS-Chem is a global 3-D chemical transport model capable of simulating global trace gas (more than 100 tracers) and aerosol distributions. In the present study, GEOS-Chem is driven by the Goddard Earth Observing System v5 (GEOS-5) assimilated meteorological fields from the NASA Global Modeling Assimilation Office (GMAO). The GEOS-5 data are available at a native horizontal resolution of $0.5^{\circ} \times 0.667^{\circ}$ and at a 6 h temporal frequency (3 h for surface variables and mixing depths). These meteorological fields provide a description of the atmosphere on the basis of 72 hybrid pressure-σ levels from the surface up to 0.01 hPa. For the simulations used here, the GEOS-5 meteorological fields are degraded to a $2^{\circ} \times 2.5^{\circ}$ horizontal resolution and 47 vertical levels, lumping together levels above ∼ 80 hPa. We apply the standard full chemistry GEOS-Chem simulation that includes detailed O_3–NO_x–VOCs–aerosol coupled chemistry described by Bey et al. (2001) and Park et al. (2004), with updates by Mao et al. (2010).

Conversely to Franco et al. (2015b) who used GEOS-Chem version 9-01-03, we employ here the model version 9-02 (http://acmg.seas.harvard.edu/geos/doc/archive/man.v9-02/index.html) that implements a new isoprene oxidation scheme as standard. This chemistry is largely based on the work of Paulot et al. (2009a, b) and has been proved to yield more HCHO from the isoprene oxidation pathways for weakly-polluted conditions (under very low-NO_x concentrations; see Marais et al., 2012). Nonetheless, results provided by the version 9-01-03 of GEOS-Chem (according to the same standard full chemistry simulation) are also provided hereafter for comparison purpose. The

ACPD
15, 31287–31333, 2015

isoprene oxidation scheme applied in GEOS-Chem v9-01-03 is described in Mao et al. (2013).

In GEOS-Chem, the global biomass burning emissions are derived from the Global Fire Emissions Database (GFED) v3 (van der Werf et al., 2010) and the global biogenic emissions are obtained with the Model of Emissions of Gases and Aerosols from Nature (MEGAN) v2.0 (Guenther et al., 2006) in GEOS-Chem v9-01-03 and v2.1 (Guenther et al., 2012) in version 9-02. Over Europe, the anthropogenic emissions of CO, NO_x, SO_x (sulfur oxides), ammonia and NMVOCs are provided by the European Monitoring and Evaluation Programme (EMEP; http://www.ceip.at/) regional inventory for the year 2010 (Simpson et al., 2010), except for ethane and propane that are derived from an offline simulation (Xiao et al., 2008), and acetone that is from the REanalysis of the TROpospheric chemical composition (RETRO; http://gcmd.gsfc.nasa.gov/records/GCMD_GEIA_RETRO.html) global emission inventory (Van het Bolscher et al., 2008) for base year 2000. The global and regional inventories are scaled to the years of interest using energy statistics (van Donkelaar et al., 2008). Annual average CH_4 concentrations are prescribed over four latitude bands (0–30; 30–90°) on the basis of CH_4 measurements from the NOAA Global Monitoring Division flask measurements.

In addition to the standard full chemistry simulations of GEOS-Chem v9-02 (hereafter called standard runs), three other runs also implementing the standard full chemistry have been performed with the version 9-02, but in each of them either the anthropogenic, biogenic or biomass burning emissions of NMVOCs and NO (nitric oxide) have been turned off. These additional simulations are referred to below as non-anthropogenic, non-biogenic and non-biomass burning runs, respectively. It is worth noting that CH_4 concentrations in these sensitivity runs are still derived from the NOAA measurements, as for the standard simulation. The different GEOS-Chem data sets used in the present study are obtained from July 2005–May 2013 simulations, for which the GEOS-5 meteorological fields are available. These simulations were preceded by

ACPD
15, 31287–31333, 2015

a 1 year run for chemical initialization, restarted several times to remove the effect of initial conditions.

The GEOS-Chem outputs consist of HCHO volume mixing ratio (VMR) profiles simulated at the closest pixel to the Jungfraujoch station and saved at a 3 h time step. The comparisons between the GEOS-Chem simulations and the FTIR total columns account for the vertical resolution and sensitivity of the FTIR retrievals. To this end, the individual VMR profiles simulated by GEOS-Chem have been regridded onto the 39-layer vertical scheme adopted at the ISSJ for the FTIR retrievals, according to a mass conservative interpolation (see details in Bader et al., 2015). Then these profiles have been smoothed according to the formalism of Rodgers and Connor (2003) by convolving them with the FTIR averaging kernels, seasonally averaged over March–May, June–August, September–November and December–February, as well as over successive years, on the basis of the July 2005–May 2013 FTIR dataset. The GEOS-Chem total columns have eventually been computed from these smoothed VMR profiles by using the corresponding regridded air density profiles simulated by the model. The comparisons between the FTIR measurements and the GEOS-Chem simulations are performed over the 919 days with observations available in the July 2005–May 2013 time range.

3 Formaldehyde diurnal variation

3.1 Observed intra-day modulation

In this Section, we investigate the HCHO diurnal variation above the ISSJ using the total column measurements derived from the January 1995–June 2015 BRUKER data set, owing to their overall improved temporal regularity and measurement density compared to the LIEGE data set. The total columns have been normalized to the mean annual pressure at the ISSJ (654 hPa) in order to avoid the effects due to pressure variation between different days/seasons on the retrieved HCHO columns. Figure 1 shows

ACPD
15, 31287–31333, 2015

the intra-day modulation of the HCHO abundance above Jungfraujoch averaged over each month of the mean year (with the HCHO total columns averaged every 0.5 h as grey circles), according to the FTIR observations made over the entire 1995–mid-2015 time period (a global view of the observed and modelled monthly intra-day cycles is available in Fig. S1 in the Supplement and in Fig. 3a, Sect. 4.1, respectively).

At the global scale, the diurnal cycles of HCHO loadings depend on local chemical regimes, which generally vary across the seasons and determine the HCHO formation and loss, as well as local emissions of NMVOC precursors and their diurnal variability. For instance, it has been shown that daytime photochemical production and anthropogenic NMVOC emissions drive the HCHO diurnal modulation over highly-populated and industrialized areas, such as in Belgium and Holland (see Stavrakou et al., 2015). However, at a remote site such as the ISSJ, located in the free troposphere during most part of the year, the overall sunrise to sunset modulation of the HCHO total columns is predominantly driven by the atmospheric photochemistry and the CH_4 oxidation (see Sect. 4.2): enhanced insolation and higher temperatures intensify the concentration in OH radicals and hence the photochemical oxidation rate of VOC precursors of HCHO. It is characterized by a.m. increases and p.m. decreases of the HCHO columns, peaking around mid-day and in the early afternoon. The amplitude of the intra-day modulation varies largely from month to month: from 0.2×10^{15} molec cm^{-2} in December up to 1.0×10^{15} molec cm^{-2} during summertime. The weaker amplitude in winter is due to relatively low solar zenith angle (SZA) around noontime, inducing less radiation, as well as to the weak moisture, both hindering the formation of OH. A similar pattern of HCHO diurnal cycle was reported over the remote ocean by MAX-DOAS measurements (Peters et al., 2012).

The FTIR measurements are irregularly distributed throughout the day, with most of the observations performed before mid-day because of frequent high cirrus clouds occurrences in the afternoon as well as the mountainous summits around the station, occulting the sun at SZA larger than $\sim 80^{\circ}$ during wintertime (see Fig. 4 in Zander et al., 2010). As a consequence, the relative uncertainty associated with the p.m. ob-

ACPD
15, 31287–31333, 2015

servations increases (see the error bars in Fig. 1). Furthermore, the retrievals from low-SZA spectra (around mid-day) are characterized by relatively low DOFS values, such as illustrated in Fig. 2a, due to the very weak solar absorptions by HCHO for low airmasses. This contributes to increasing the uncertainty on the retrieved total columns and explains the fluctuations of the running average observed around noontime during the summer months (see Fig. 1). The diurnal variation of the HCHO abundance also shows for some months (e.g., August and September in Fig. 1b and d, respectively) a small re-increase of the total columns at the end of the day. This results from the fact that only observations made during later (earlier) days of the month are available at this moment for the first (last) six months of the year (see Fig. 2b), due to the increasing (shortening) day length. Given the typical seasonal cycle of HCHO throughout the year, such measurements hence provide somewhat larger (lower) HCHO columns.

3.2 Parametric model of the diurnal variation

The diurnal modulation of the HCHO abundance above Jungfraujoch corresponds to a large short-term variability that should be accounted for when comparing ground-based observations to e.g., satellite measurements and model results. Moreover, it is worth describing such a modulation in order to remove it before investigating seasonal/inter-annual variability of HCHO in the following parts of this study. Therefore, we have adjusted a fitting parametric model to each monthly subset, the results being presented in Fig. 1. To this end, the intra-day modulation used to adjust the parametric model consists of a running average (not shown in Fig. 1) of all individual FTIR measurements within each month, calculated using a 0.5 h time step and a 1.5 h-wide integration length (compatible with the HCHO lifetime). The smoothing associated with the running average helps dampening the contribution of very high HCHO loadings that correspond to "polluting" events. The previous analysis has highlighted that modelling the HCHO diurnal cycle merely according to the seasons would not capture the large differences observed from month to month, especially during spring and fall. Hence we have also adjusted the fitting parametric model while considering monthly diurnal cy-

ACPD
15, 31287–31333, 2015

cles, in order to keep enough p.m. observations (i.e. statistics) for adjusting the model with high reliability.

The model used here (described in Eq. 1) consists in a re-parametrization of the standard statistical form of the Weibull continuous probability distribution of a random variable x. In this study, it determines the HCHO total column (y) as a density function of the hour of the day (x), according to the amplitude (a), the scale parameter (b), the shape parameter (c) and the location parameter (or threshold; x_0) of the distribution. The Weibull density function is a versatile distribution capable of adopting the characteristics of other types of distributions, according to the value of the shape parameter (c), and is widely used to mimic peaking distributions with asymmetric slopes.

$$y = a\left(\frac{c-1}{c}\right)^{\left(\frac{1-c}{c}\right)} \times \left|\frac{x-x_0}{b} + \left(\frac{c-1}{c}\right)^{\left(\frac{1}{c}\right)}\right|^{(c-1)} \times \exp^{-\left|\frac{x-x_0}{b}+\left(\frac{c-1}{c}\right)^{\left(\frac{1}{c}\right)}\right|^{c}+\frac{c-1}{c}} \quad (1)$$

The model has been adjusted to the observations and the parameters calculated by using the iterative Levenberg–Marquardt algorithm (Marquardt, 1963) that minimizes the sum of the squared differences between the observations and the predicted values of the model until convergence occurs (i.e. when the residuals no longer decreases significantly). The model fit for each month is represented as solid color curves in Fig. 1, along with the associated 95 % confidence and prediction bands. The coefficients of determination (R^2) calculated between the monthly observations and model fits are high and range from 0.78 to 0.95 (see Fig. 1). The parameters a, b, c and x_0 determined by the adjustments are given for each month in Table S1 in the Supplement so that one may reproduce the model fits using Eq. (1).

The model is able to reproduce with reliability the diurnal modulation of HCHO loadings above Jungfraujoch and allows for its quantitative characterization for a typical day of each month of the year, thanks to the large BRUKER statistical database. Since this

ACPD
15, 31287–31333, 2015

model is parameterized, we use it in this study to scale individual FTIR measurements on a given moment of the day before carrying out a comparison with GEOS-Chem outputs (see Sect. 4.1) and a long-term trend study (see Sect. 5.2). Nonetheless, such a model cannot be used to extrapolate the HCHO total columns outside the actual range of measurements. In addition, this model is only valid if the condition in Eq. (2) is true, otherwise the Weibull distribution collapses and the results are null (e.g., for the very first hours of the day).

$$x > x_0 - b\left(\frac{c-1}{c}\right)^{\left(\frac{1}{c}\right)} \quad (2)$$

In order to remove the effect of the intra-day cycle, the pressure-normalized total columns obtained from all individual measurements have been scaled to 9 a.m. (UTC+1) on the basis of the parametric model described previously. Using Eq. (1) that links the daytime to the HCHO columns, as well as the constant parameters determined for each month, the total column derived from a solar spectrum is scaled according to the difference between the actual time of the corresponding observation and 9 a.m. (UTC + 1). An example is illustrated for June by the color circles in Fig. 3a (see Sect. 4.1): an initial total column of 2.356×10^{15} molec cm^{-2} derived from an observation made at 13.025 a.m. is decreased to 2.072×10^{15} molec cm^{-2} when scaled at 9 a.m. Here we have chosen 9 a.m. as reference time because observations for every month are available at this moment of the day, added to the fact that the gap between the different monthly intra-day regimes in terms of HCHO columns is minimal in the morning.

ACPD
15, 31287–31333, 2015

4 Formaldehyde simulated by GEOS-Chem

4.1 Comparison with GEOS-Chem standard run

Figure 3 presents the monthly diurnal variations as adjusted by the parametric model on the basis of the FTIR observations in Sect. 3.2 (Fig. 3a) and as derived from the 3 h outputs of the GEOS-Chem v9-02 standard run spanning the mid-2005–mid-2013 time period (Fig. 3b). The diurnal modulation of HCHO loadings above Jungfraujoch represents a large short-term variability superimposed on seasonal and inter-annual variations (Fig. 3a) that should be accounted for when comparing ground-based observations to e.g., model results. However, Fig. 3b shows that GEOS-Chem does not capture the observed monthly intra-day variation. That a CTM is unable to simulate the observed HCHO diurnal modulation, especially for remote conditions, has already been reported with IMAGES v2 (Stavrakou et al., 2015). This can be partially explained by the fact that different oxidation pathways of VOC precursor leading the HCHO production, which are numerous, might not be optimally implemented (especially very short-lived VOCs) or merely not considered in the model. In addition, large uncertainties remain concerning the various sources of precursor emissions, their geographical distribution and how these latter can influence the air masses over remote sites such as the ISSJ. Finally, the CTMs dilute local enhancements in HCHO due to their relatively coarse spatial resolution ($2^\circ \times 2.5^\circ$ here), which also affects the comparison with observations.

For this reason, we compare in this section HCHO total columns simulated by GEOS-Chem and obtained from the 9 a.m. model outputs, to the daily-averaged FTIR total columns calculated on the basis of the 9 a.m.-scaled individual observations (see Sect. 3.2). This comparison is made over the May 2005–June 2015 time period, for the days with available FTIR observations only. In this study, some outliers, likely due to transport of air masses with high NMVOC precursor concentrations up to ISSJ, have been discarded from the FTIR data set. Indeed, the CTMs are generally unable to simulate such "polluting" events for the reasons evoked above. These outliers have

ACPD
15, 31287–31333, 2015

been identified as the daily-averaged HCHO total columns with relative anomalies to the curve fitted by the method of Gardiner et al. (2008, see Sect. 5.2 and Fig. 7 here below) higher than the 95th percentile value of all relative anomalies of the 2003–2015 data set.

Figure 4 presents the good agreement ($R = 0.72$) in terms of seasonal cycles of HCHO loadings above Jungfraujoch, obtained from the FTIR observations and such as simulated by the GEOS-Chem v9-02 standard run. A similar seasonal comparison over the mid-2010–2012 time range has been carried out by Franco et al. (2015b), but involving results from the GEOS-Chem v9-01-03 standard run (in dashed red line in Fig. 4). This comparison illustrates the higher HCHO columns simulated by the version 9-02 of GEOS-Chem compared to the version 9-01-03, due to the implementation of the new isoprene oxidation scheme (Paulot et al., 2009a, b) that enhances the HCHO formation under very low-NO_x concentrations. We refer to Franco et al. (2015b), Sect. 4.1, for the discussion regarding the mean seasonal bias of the GEOS-Chem results to the FTIR HCHO total columns, which is here of -4.7 ± 31.3 %. As the model does not reproduce the HCHO intra-day variations at the ISSJ, this bias increases to -21.3 ± 26.4 % for the comparison involving the 12 a.m. GEOS-Chem outputs and the 12 a.m.-scaled individual FTIR observations (with $R = 0.69$).

4.2 GEOS-Chem sensitivity tests

In this part of the study, we investigate the influence of the different categories of emission sources implemented in GEOS-Chem v9-02, on the HCHO abundance simulated by the model above Jungfraujoch. To this end, we compare the results from the standard run and from the three sensitivity runs performed without either anthropogenic, biomass burning or biogenic emissions of NMVOCs and NO. Figure 5a shows the monthly-averaged HCHO total columns at the ISSJ, derived from these simulations from July 2005 to May 2013. Figure 5b presents the HCHO total columns from the three sensitivity runs as relative to the amount from the standard run.

ACPD
15, 31287–31333, 2015

In Fig. 5a and b, it can be seen that none of the missing emission sources significantly impacts the simulated HCHO loadings in summer at the ISSJ, with the HCHO columns derived from either the non-anthropogenic or non-biogenic runs still accounting for ∼ 95 % of the total columns from the standard run (Fig. 5b). During this season, biogenic primary NMVOCs such as isoprene may constitute a significant source of HCHO, especially in the continental boundary layer. However, it is most likely that a large part of these very short-lived NMVOCs are already oxidized before being transported to the ISSJ. Hence these compounds do not contribute directly to the HCHO loadings above Jungfraujoch, although they release biogenic secondary products that can be transported to the upper troposphere and in turn can be oxidized, adding to the HCHO abundance in the upper tropospheric layers. During wintertime, the absence of anthropogenic emissions decreases the HCHO burden down to 75 % of the standard run (Fig. 5b), with a December–February average of 82 % over July 2005–May 2013. Due to their longer lifetimes and more intensive anthropogenic combustion during this season, more elevated concentrations in reactive anthropogenic compounds can be measured in winter at the ISSJ (Balzani Lööv et al., 2008; Legreid et al., 2008; Starokozhev et al., 2009), which contributes to the HCHO formation. Finally, the missing biomass burning emissions have almost no effect on the simulated HCHO loadings above Jungfraujoch (Fig. 5b). These tests suggest that the contribution of anthropogenic, biogenic and pyrogenic NMVOCs to the HCHO burden above Jungfraujoch is quite limited, and that the oxidation of CH_4 (not included in the emission sources shut off here) by OH dominates the HCHO production and constitutes the main driver of its seasonality.

It is worth noting that turning off the emission sources in the GEOS-Chem sensitivity tests investigated here, may eventually result in slightly enhanced HCHO amounts (by 2–3 %) produced by GEOS-Chem compared to the standard run, as shown in Fig. 5b for the non-biomass burning run and, in a lesser extent, for the non-biogenic run during winter. In these particular cases, with part of the emission sources missing globally, enhanced HCHO might be due to a lower concentration in associated NMVOCs for which

ACPD
15, 31287–31333, 2015

OH is the main sink, inducing enhanced OH loadings above Jungfraujoch available for oxidation of other VOC precursors of HCHO, such as CH_4. Indeed, Fig. 5c illustrating the monthly-averaged OH amounts simulated by the different sensitivity runs, as relative to the standard run, shows OH total columns from the non-biomass burning and non-biogenic runs increased by up to 10 %. However, it is hard to evaluate the impact of the excluded NO emissions, since this compound plays a key role in both HCHO formation (through the NMVOC oxidation pathways) and destruction (by contributing to the regeneration of OH). Investigating the balance between all these reactions would require a specific study that is beyond the scope of the present work.

According to the GEOS-Chem simulation performed without anthropogenic emissions, the wintertime contribution of anthropogenic NMVOC precursors to the HCHO total column above Jungfraujoch varies from year to year (from 15 to 25 %; Fig. 5b). However, the wintertime total carbon emissions of anthropogenic origin as implemented into GEOS-Chem from the inventories, are approximately constant throughout the entire July 2005–May 2013 time range ($\sim 2.7\,\mathrm{Tg\,C\,month^{-1}}$; Fig. 5d) when integrated over Europe (between 38–56° N and −15–55° E). Hence this suggests that the HCHO production from oxidized anthropogenic compounds and its inter-annual variability at the ISSJ are mainly driven in GEOS-Chem by the simulated OH burden and its year-to-year fluctuation (Fig. 5c).

5 Formaldehyde time series

5.1 Consistency between the FTIR data sets

We investigate hereafter the long-term evolution of the HCHO abundance at ISSJ, using both the LIEGE and BRUKER FTIR data sets. We first evaluate the consistency of the measurements derived from both instruments. To this end, we compare the HCHO total columns derived from solar spectra recorded on the same days, using the 1995–1997 overlap time period while accounting for the diurnal modulation of the HCHO

ACPD
15, 31287–31333, 2015

abundance. Figure 6 shows a scatter plot of the scaled (to 9 a.m.) BRUKER vs. LIEGE total column daily means, including the 25 days available over the 1995–1997 years. The comparison demonstrates a very good agreement between both data sets, with a high coefficient of determination (R^2 = 0.89), for both low and high HCHO columns (corresponding globally to measurements performed during winter and summer). Given the good consistency and absence of significant bias, the LIEGE and BRUKER data sets will be jointly used hereafter to investigate the long-term variation of the HCHO abundance above Jungfraujoch.

5.2 Formaldehyde multi-decadal trend

Combined together, the LIEGE and BRUKER data sets constitute a unique database covering more than twenty-seven years (from January 1988 to June 2015), providing to our best knowledge the longest consistent time series of remote ground-based observations of HCHO worldwide. In this part of the study, we employ the HCHO total columns derived from all individual FTIR observations made over the 1988–2015 time period, scaled at 9 a.m. according to the method described previously, and eventually combined as daily means. The entire daily mean total column time series is illustrated in Fig. 7. We have applied to the whole data set a running mean characterized by a 3 year integration length and a 6-month time step, in order to minimize the influence of the large intra-annual variability of HCHO. This has revealed a significant maximum of HCHO columns between end 1995 and early 1996, as well as a minimum around the beginning of 2003. The trend and associated uncertainty affecting each subset (i.e. the daily mean total column subsets spanning the 1988–1995, 1996–2002 and 2003–2015 periods, respectively) have been determined using a statistical bootstrap resampling tool (Gardiner et al., 2008) combining a linear function and a third-order Fourier series that accounts for the strong seasonal modulation of HCHO (in blue curve in Fig. 7).

Analysis of the whole time series indicates statistically-significant rate of change (at the 2σ confidence level) of the HCHO abundance over each time period: 4.35 ± 2.98, -7.22 ± 1.97 and $1.20 \pm 0.92 \times 10^{13}$ molec cm^{-2} yr^{-1} for 1988–1995, 1996–2002

ACPD
15, 31287–31333, 2015

and 2003–2015, respectively. Using the 1988.0, 1996.0 and 2003.0 columns modelled by the bootstrap tool as references, we obtain the following relative annual trends: $2.94 \pm 2.02\,\%\,yr^{-1}$ up to 1995, $-3.68 \pm 1.00\,\%\,yr^{-1}$ between 1996 and 2002, and $0.81 \pm 0.62\,\%\,yr^{-1}$ from 2003 onwards. It is worth noting that the choice of the reference hour for scaling the individual HCHO columns has no significant impact on the calculated rates of change. For example, the relative annual trends obtained from HCHO total columns scaled at 12 p.m., i.e. when the difference between the 12 monthly intra-day regimes is near its maximum, are $2.55 \pm 1.75\,\%\,yr^{-1}$ (1988–1995), $-3.26 \pm 0.90\,\%\,yr^{-1}$ (1996–2002) and $0.70 \pm 0.54\,\%\,yr^{-1}$ (2003–2015). However, these trends may differ when calculated over specific seasons only. The corresponding results are summarized in Table 2.

The HCHO increase observed above Jungfraujoch between 1988 and 1995 may be related to the sharp rise of the atmospheric CH_4 growth rate from the 1980s to the beginning of the 1990s (Nisbet et al., 2014), which is its main precursor in the background troposphere (see Sect. 4.2). Above the ISSJ, Zander et al. (2008) calculated discrete annual changes of CH_4 total column derived from FTIR observations equal to 0.72 and $0.31\,\%\,yr^{-1}$ for 1987–1988 and 1995–1996, respectively. In addition, all seasons also present a significant positive rate of change of HCHO loadings at the 2σ confidence level over this time period, excepting fall (see Table 2). Nonetheless, the data set covering this time range is mainly constituted of FTIR measurements recorded with the LIEGE instrument, which are sparser than those obtained with the BRUKER spectrometer from 1995 onwards (as obvious in Fig. 7). This may explain the relatively large 2σ confidence levels associated with the trends determined over this period. Conversely, the decreased HCHO loadings from 1996 to 2002 may be due to the global stabilization of the CH_4 concentrations during most of this period (Dlugokencky, 2003), which was also observed at the ISSJ (Zander et al., 2008), combined to reduced emissions mainly from fossil fuel sources in the Northern Hemisphere (Aydin et al., 2011; Simpson et al., 2012) and short-term variations of the atmospheric OH burden (Montzka et al., 2011).

ACPD
15, 31287–31333, 2015

However, it should be noted that the wintertime minimum of HCHO is not affected by this decrease (see Table 2).

The observed rise of the HCHO total columns at the ISSJ during the last decade (over 2003–mid-2015), which mainly occurs during spring (see Table 2), may be explained by the highly-studied global renewed increase of atmospheric CH_4, starting in the mid-2000s (Kirschke et al., 2013; Nisbet et al., 2014). Indeed, this enhanced growth rate of CH_4 total columns have already been highlighted at the ISSJ from 2005 onwards, using ground-based FTIR measurements and a GEOS-Chem tagged simulation (Bader et al., 2015). It is also worth noting that the decrease of many anthropogenic precursors of HCHO as a result of pollution abatements in the Northern Hemisphere has no apparent influence on the HCHO evolution during the last decade, probably due to the fact that the HCHO formation coming from these oxidized anthropogenic compounds is dominated by the methane-originated production, as pointed out in Sect. 4.2. Globally over the 1996–mid-2015 time period, the high-rate depletion of the HCHO loadings at the ISSJ over 1996–2002 still dominates the slow renew from 2003 onwards: the rate of change of the HCHO burden is $-0.61 \pm 0.26\,\%\,yr^{-1}$ from January 1996 to June 2015.

6 Summary and conclusions

In this study, we use the strategy developed by Franco et al. (2015b) to retrieve HCHO total columns from high-resolution ground-based FTIR solar spectra recorded at the high-altitude station of Jungfraujoch. Because of its localization, this site allows for the study of the continental background conditions in the remote troposphere at mid-latitude of the Northern Hemisphere. Using the large statistics that represents the January 1995–June 2015 data set of solar spectra recorded with a Bruker instrument, we first investigate the HCHO diurnal variations above the station. These variations, resulting in a.m. increases and p.m. decreases peaking around mid-day and in the early afternoon, are mainly driven by the atmospheric photochemistry, the intra-day inso-

ACPD
15, 31287–31333, 2015

lation modulation and the CH_4 oxidation. Then, we characterize quantitatively these monthly diurnal variations by adjusting a parametric model to the observations, consisting in a re-parametrization of the standard statistical form of the Weibull continuous probability distribution of a random variable. The equation of the model and its parameters determined on the basis of the observations are provided. As this model is fully parameterized and links the daytime to the HCHO columns, it is eventually used to scale all the individual FTIR measurements on 9 a.m. (i.e. when the difference between the monthly intra-day regimes is minimal) in order to remove the effect of the intra-day modulation.

In the next part of the study, we perform a GEOS-Chem v9-02 simulation of the HCHO loadings above Jungfraujoch over the July 2005–May 2013 time period. As the analysis of the model outputs revealed that GEOS-Chem does not reproduce the observed diurnal variations of the HCHO columns, we use the daily-mean 9 a.m.-scaled FTIR measurements to compare with the simulated 9 a.m. total columns, accounting for the vertical resolution and sensitivity of the FTIR retrievals. Over this period, the enhanced HCHO burden simulated by GEOS-Chem v9-02 compared to the version 9-01-03 reduces the mean bias with the observations, due to the implementation of the new isoprene oxidation scheme in version 9-02. Results from GEOS-Chem sensitivity runs (turning off successively either the anthropogenic, biogenic or biomass burning emissions of NMVOCs and NO implemented in the model) are also investigated and suggest that the HCHO loadings above Jungfraujoch, as well as its seasonal and inter-annual variations, are predominantly led by the atmospheric CH_4 oxidation. The anthropogenic precursors of HCHO are estimated to contribute up to 25 % to the wintertime HCHO total columns, while the impact of each of the other emission sources is limited to 5 %.

Finally, we exploit the large database of FTIR solar spectra recorded at the Jungfraujoch station by two high-resolution spectrometers spanning the 1988–1997 and 1995–2015/06 time periods, respectively. After checking the consistency between both subsets in terms of retrieved HCHO columns, we combine them in order to produce

ACPD
15, 31287–31333, 2015

a 27 year time series of HCHO total columns, which is to our best knowledge the longest time series of remote HCHO observations worldwide. Employing the parametric model, the intra-day variation is removed by scaling all the individual measurements of the data set to 9 a.m. We eventually use the so-scaled entire time series to study the long-term evolution of the HCHO columns in the background troposphere. Trend analysis reveals an increasing HCHO burden between 1988 and 1995 ($2.9\,\%\,yr^{-1}$), followed by a sharp depletion over 1996–2002 ($-3.7\,\%\,yr^{-1}$) and a slow renew of the growth rate from 2003 onwards ($0.8\,\%\,yr^{-1}$). This long-term evolution above Jungfraujoch is likely to be related with the fluctuations of the atmospheric CH_4 as well as with the short-term variability of the OH concentrations.

Regional decadal trends at the global scale of mid-morning and early-afternoon HCHO columns have been recently derived from combined SCIAMACHY–GOME-2A, B and OMI measurements, respectively, over the 2004–2014 time period (De Smedt et al., 2015). Over Western Europe, these trends show an overall significant decrease of the HCHO abundance (between -1.5 and $-3.0\,\%\,yr^{-1}$, mainly attributed to effective pollution regulation measures (De Smedt et al., 2010). According to the ground-based FTIR observations, we observe on the contrary a weak significant increase (less than $1\,\%\,yr^{-1}$) of the HCHO total columns above the ISSJ, over approximately the same time period (2003–2015). These opposite trends may be explained by the fact that the space borne measurements cover entire regions (more specifically Germany, France and Spain) that are largely under influence of anthropogenic emissions of NMVOC precursors, while the Jungfraujoch HCHO columns are generally characteristic of the remote troposphere and mainly originate from the CH_4 oxidation (see results in Sect. 4.2).

Due to its very short lifetime, the abundance and spatial distribution of HCHO in the atmosphere can be closely related to the emissions of its NMVOC precursors and resemble their distribution in the atmosphere if the NMVOC lifetime is short enough to avoid the spatial relationship being smeared by atmospheric transport. Conversely, emissions of long-lived VOCs (such as CH_4) will produce a global HCHO background with no detectable localized signal. As the HCHO loading above the ISSJ is predomi-

ACPD
15, 31287–31333, 2015

nantly originating from the photochemical oxidation regimes of CH_4, such inverse modelling studies will be difficult to carry out on the basis of the ground-based FTIR measurements of HCHO. Nevertheless, identifying in the Jungfraujoch time series the large HCHO columns that are due to the injection of "polluted" air masses from the planetary boundary layer (e.g., from the nearby industrialized valleys), by the use of backward trajectories models, can help in the determination of significant trends of HCHO according to the origin of the air masses.

As HCHO is a key component in the global catalytic cycle responsible for generating or destroying tropospheric O_3 (depending on the NO_x levels), monitoring and understanding of the HCHO evolution for background conditions are of primary importance. Indeed, many questions arise as regards to the renewed increase of atmospheric CH_4, the main precursor of HCHO in the remote troposphere. According to Stickler et al. (2006) and Fried et al. (2008), oxidized CH_4 still represents an important source to HCHO production in the uppermost tropospheric layers, with contributions that vary from 40 to more than 50 %, depending on the air masses. More particularly, a sharp increase of the ethane (C_2H_6) burden close to 5 % yr^{-1} since 2009, attributed to the massive growth of shale gas exploitation in North America, has recently been highlighted above Jungfraujoch (Franco et al., 2015a). Therefore, as C_2H_6 is a HCHO precursor and shares most of its sources with CH_4, there are some concerns as to the impact on the evolution of the HCHO loadings. Ground-based FTIR measurements combined to model simulations can undoubtedly help on these issues.

The parametric model implemented in this study and the quantitative characterization of the monthly intra-day variations of HCHO may be a very useful tool in future works dedicated to the comparison between ground-based FTIR and space borne HCHO measurements. Indeed, long-term consistent data sets of regular HCHO observations are increasingly required for calibration/validation efforts of present satellite instruments, such as OMI and GOME-2. Furthermore, from 2017 onwards, the space borne monitoring observations are planned to continue with TROPOMI (TROPOspheric Monitoring Instrument) and a third GOME-2 instrument. By scaling the FTIR

ACPD
15, 31287–31333, 2015

HCHO columns to the respective overpass times of the satellite sensors, this parametric model applied to the Jungfraujoch long-term time series may be of high value for future validation/calibration tasks in remote conditions at mid-latitude of the Northern Hemisphere. The parameters are made available as Table S1 in the Supplement.

The Supplement related to this article is available online at doi:10.5194/acpd-15-31287-2015-supplement.

Acknowledgements. The University of Liège contribution has been primarily supported by the PRODEX project ACROSAT funded by the Belgian Science Policy Office (BELSPO). The F.R.S.-FNRS and the Fédération Wallonie Bruxelles contributed to observational activities support. The Swiss GAW-CH program is further acknowledged. E. Mahieu is research associate with F.R.S.-FNRS. We are grateful to the International Foundation High Altitude Research Stations Jungfraujoch and Gornergrat (HFSJG, Bern) for supporting the facilities needed to perform the observations. We further acknowledge the vital contribution from all the Belgian colleagues in performing the Jungfraujoch FTIR observations, among which Philippe Demoulin for recording all the homemade spectra used here. This research was also financially supported at ULg by the EU 7th Framework Programme projects NORS (contract 284421) and AGACC-II (BELSPO, Brussels).

References

Anderson, L. G., Lanning, J. A., Barrell, R., Miyagishima, J., Jones, R. H., and Wolfe, P.: Sources and sinks of formaldehyde and acetaldehyde: An analysis of Denver's ambient concentration data, Atmos. Environ., 30, 12, 2113–2123, doi:10.1016/1352-2310(95)00175-1, 1996. 31289

Atkinson, R.: Atmospheric chemistry of VOCs and NO_x, Atmos. Environ., 34, 2063–2101, doi:10.1016/S1352-2310(99)00460-4, 2000. 31289

Aydin, M., Verhulst, K. R., Saltzman, E. S., Battle, M. O., Montzka, S. A., Blake, D. R., Tang, Q., and Prather, M. J.: Recent decreases in fossil-fuel emissions of ethane and methane derived from firn air, Nature, 476, 198–201, doi:10.1038/nature10352, 2011. 31307

ACPD
15, 31287–31333, 2015

Bader, W., Bovy, B., Conway, S., Strong, K., Smale, D., Turner, A. J., Bernath, P. F., Blumenstock, T., Coulon, A., Franco, B., Garcia, O., Griffith, D., Hase, F., Hausmann, P., Jones, N., Lejeune, B., Murata, I., Morino, I., Nakajima, H., Paton-Walsh, C., Robinson, J., Schneider, M., Servais, C., Sussmann, R., and Mahieu, E.: Changes of atmospheric methane (CH_4) since 2005 from NDACC FTIR measurements and GEOS-Chem tagged simulation, J. Geophys. Res.-Atmos., in review, 2015. 31297, 31308

Balzani Lööv, J. M., Henne, S., Legreid, G., Staehelin, J., Reimann, S., Prévôt, A. S. H., Steinbacher, M., and Vollmer, M. K.: Estimation of background concentrations of trace gases at the Swiss Alpine site Jungfraujoch (3580 m a.s.l.), J. Geophys. Res., 113, D22305, doi:10.1029/2007JD009751, 2008. 31304

Bey, I., Jacob, D. J., Yantosca, R. M., Logan, J. A., Field, B. D., Fiore, A. M., Li, Q., Liu, H. Y., Mickley, L. J., and Schultz, M. G.: Global modeling of tropospheric chemistry with assimilated meteorology: model description and evaluation, J. Geophys. Res.-Atmos., 106, 23073–23095, doi:10.1029/2001JD000807, 2001. 31292, 31295

Calvert, J. G., Atkinson, R., Kerr, J. A., Madronich, S., Moortgat, G. K., Wallington, T. J., and Yarwood, G. (Eds.): The mechanisms of atmospheric oxidation of the alkenes, Oxford University Press, New York, 552 p., 2000. 31289

Cantrell, C. A., Davidson, J. A., McDaniel, A. H., Shetter, R. E., and Calvert, J. G.: Temperature-dependent formaldehyde cross sections in the near-ultraviolet spectral region. J. Phys. Chem., 94, 3902–3908, doi:10.1021/j100373a008, 1990. 31289

Carlier, P., Hannachi, H., and Mouvier, G.: The chemistry of carbonyl compounds in the atmosphere: A review, Atmos. Environ., 20, 2079–2099, doi:10.1016/0004-6981(86)90304-5, 1986. 31290

Chance, K., Palmer, P. I., Spurr, R. J. D., Martin, R. V., Kurosu, T. P., and Jacob, D. J.: Satellite observations of formaldehyde over North America from GOME, Geophys. Res. Lett., 27, 3461–3464, doi:10.1029/2000GL011857, 2000. 31290

Choi, W., Faloona, I. C., Bouvier-Brown, N. C., McKay, M., Goldstein, A. H., Mao, J., Brune, W. H., LaFranchi, B. W., Cohen, R. C., Wolfe, G. M., Thornton, J. A., Sonnenfroh, D. M., and Millet, D. B.: Observations of elevated formaldehyde over a forest canopy suggest missing sources from rapid oxidation of arboreal hydrocarbons, Atmos. Chem. Phys., 10, 8761–8781, doi:10.5194/acp-10-8761-2010, 2010. 31291

de Serves, C.: Gas phase formaldehyde and peroxide measurements in the Arctic atmosphere, J. Geophys. Res., 99, 25391–25398, doi:10.1029/94JD00547, 1994. 31290

ACPD
15, 31287–31333, 2015

De Smedt, I., Stavrakou, T., Müller, J.-F., van der A. R. J., and Van Roozendael, M.: Trend detection in satellite observations of formaldehyde tropospheric columns, Geophys. Res. Lett., 37, L18808, doi:10.1029/2010GL044245, 2010. 31290, 31291, 31310

De Smedt, I., Van Roozendael, M., Stavrakou, T., Müller, J.-F., Lerot, C., Theys, N., Valks, P., Hao, N., and van der A, R.: Improved retrieval of global tropospheric formaldehyde columns from GOME-2/MetOp-A addressing noise reduction and instrumental degradation issues, Atmos. Meas. Tech., 5, 2933–2949, doi:10.5194/amt-5-2933-2012, 2012.

De Smedt, I., Stavrakou, T., Hendrick, F., Danckaert, T., Vlemmix, T., Pinardi, G., Theys, N., Lerot, C., Gielen, C., Vigouroux, C., Hermans, C., Fayt, C., Veefkind, P., Müller, J.-F., and Van Roozendael, M.: Diurnal, seasonal and long-term variations of global formaldehyde columns inferred from combined OMI and GOME-2 observations, Atmos. Chem. Phys. Discuss., 15, 12241–12300, doi:10.5194/acpd-15-12241-2015, 2015. 31290, 31291, 31310

DiGangi, J. P., Boyle, E. S., Karl, T., Harley, P., Turnipseed, A., Kim, S., Cantrell, C., Maudlin III, R. L., Zheng, W., Flocke, F., Hall, S. R., Ullmann, K., Nakashima, Y., Paul, J. B., Wolfe, G. M., Desai, A. R., Kajii, Y., Guenther, A., and Keutsch, F. N.: First direct measurements of formaldehyde flux via eddy covariance: implications for missing in-canopy formaldehyde sources, Atmos. Chem. Phys., 11, 10565–10578, doi:10.5194/acp-11-10565-2011, 2011. 31290

DiGangi, J. P., Henry, S. B., Kammrath, A., Boyle, E. S., Kaser, L., Schnitzhofer, R., Graus, M., Turnipseed, A., Park, J-H., Weber, R. J., Hornbrook, R. S., Cantrell, C. A., Maudlin III, R. L., Kim, S., Nakashima, Y., Wolfe, G. M., Kajii, Y., Apel, E.C., Goldstein, A. H., Guenther, A., Karl, T., Hansel, A., and Keutsch, F. N.: Observations of glyoxal and formaldehyde as metrics for the anthropogenic impact on rural photochemistry, Atmos. Chem. Phys., 12, 9529–9543, doi:10.5194/acp-12-9529-2012, 2012. 31290

Dufour, G., Szopa, S., Barkley, M. P., Boone, C. D., Perrin, A., Palmer, P. I., and Bernath, P. F.: Global upper-tropospheric formaldehyde: seasonal cycles observed by the ACE-FTS satellite instrument, Atmos. Chem. Phys., 9, 3893–3910, doi:10.5194/acp-9-3893-2009, 2009a. 31290

Dufour, G., Wittrock, F., Camredon, M., Beekmann, M., Richter, A., Aumont, B., and Burrows, J. P.: SCIAMACHY formaldehyde observations: constraint for isoprene emission estimates over Europe?, Atmos. Chem. Phys., 9, 1647–1664, doi:10.5194/acp-9-1647-2009, 2009b. 31290

ACPD
15, 31287–31333, 2015

Dlugokencky, E. J.: Atmospheric methane levels off: temporary pause or a new steady-state?, Geophys. Res. Lett., 30, 1992, doi:10.1029/2003GL018126, 2003. 31307

Franco, B., Bader, W., Toon, G. C., Bray, C., Perrin, A., Fischer, E. V., Sudo, K., Boone, C. D., Bovy, B., Lejeune, B., Servais, C., and Mahieu, E.: Retrieval of ethane from ground-based FTIR solar spectra using improved spectroscopy: recent burden increase above Jungfraujoch, J. Quant. Spectrosc. Ra., 160, 36–49, doi:10.1016/j.jqsrt.2015.03.017, 2015a. 31311

Franco, B., Hendrick, F., Van Roozendael, M., Müller, J.-F., Stavrakou, T., Marais, E. A., Bovy, B., Bader, W., Fayt, C., Hermans, C., Lejeune, B., Pinardi, G., Servais, C., and Mahieu, E.: Retrievals of formaldehyde from ground-based FTIR and MAX-DOAS observations at the Jungfraujoch station and comparisons with GEOS-Chem and IMAGES model simulations, Atmos. Meas. Tech., 8, 1733–1756, doi:10.5194/amt-8-1733-2015, 2015b. 31290, 31292, 31294, 31295, 31303, 31308, 31325

Fried, A., Lee, Y.-N., Frost, G., Wert, B., Henry, B., Drummond, J. R., Hübler, G., and Jobson, T.: Airborne CH_2O measurements over the North Atlantic during the 1997 NARE campaign: instrument comparisons and distributions, J. Geophys. Res.-Atmos., 107, 4039, doi:10.1029/2000JD000260, 2002. 31289, 31290

Fried, A., Olson, J. R., Walega, J. G., Crawford, J. H., Chen, G., Weibring, P., Richter, D., Roller, C., Tittel, F., Porter, M., Fuelberg, H., Halland, J., Bertram, T. H., Cohen, R. C., Pickering, K., Heikes, B. G., Snow, J. A., Shen, H., O'Sullivan, D. W., Brune, W. H., Ren, X., Blake, D. R., Blake, N., Sachse, G., Diskin, G. S., Podolske, J., Vay, S. A., Shetter, R. E., Hall, S. R., Anderson, B. E., Thornhill, L., Clark, A. D., McNaughton, C. S., Singh, H. B., Avery, M. A., Huey, G., Kim, S., and Millet, D. B.: Role of convection in redistributing formaldehyde to the Upper Troposphere over North America and the North Atlantic during the Summer 2004 INTEX campaign, J. Geophys. Res., 113, D17306, doi:10.1029/2007JD009760, 2008. 31290, 31311

Fried, A., Cantrell, C., Olson, J., Crawford, J. H., Weibring, P., Walega, J., Richter, D., Junkermann, W., Volkamer, R., Sinreich, R., Heikes, B. G., O'Sullivan, D., Blake, D. R., Blake, N., Meinardi, S., Apel, E., Weinheimer, A., Knapp, D., Perring, A., Cohen, R. C., Fuelberg, H., Shetter, R. E., Hall, S. R., Ullmann, K., Brune, W. H., Mao, J., Ren, X., Huey, L. G., Singh, H. B., Hair, J. W., Riemer, D., Diskin, G., and Sachse, G.: Detailed comparisons of airborne formaldehyde measurements with box models during the 2006 INTEX-B and MILAGRO campaigns: potential evidence for significant impacts of unmeasured and multi-

ACPD
15, 31287–31333, 2015

generation volatile organic carbon compounds, Atmos. Chem. Phys., 11, 11867–11894, doi:10.5194/acp-11-11867-2011, 2011. 31290

Frost, G. J., Fried, A., Lee, Y.-N., Wert, B., Henry, B., Drummond, J. R., Evans, M. J., Fehsenfeld, F. C., Goldan, P. D., Holloway, J. S., Hübler, G., Jakoubek, R., Jobson, B. T., Knapp, K., Kuster, W. C., Roberts, J., Rudolph, J., Ryerson, T. B., Stohl, A., Stroud, C., Sueper, D. T., Trainer, M., and Williams, J.: Comparisons of box model calculations and measurements of formaldehyde from the 1997 North Atlantic Regional Experiment, J. Geophys. Res., 107, 4060, doi:10.1029/2001JD000896, 2002. 31290

Fu, T.-M., Jacob, D. J., Palmer, P. I., Chance, K., Wang, Y. X., Barletta, B., Blake, D. R., Stanton, J. C., and Pilling, M. J.: Space-based formaldehyde measurements as constraints on volatile organic compound emissions in east and south Asia and implications for ozone, J. Geophys. Res., 112, D06312, doi:10.1029/2006JD007853, 2007. 31290

Gardiner, T., Forbes, A., de Mazière, M., Vigouroux, C., Mahieu, E., Demoulin, P., Velazco, V., Notholt, J., Blumenstock, T., Hase, F., Kramer, I., Sussmann, R., Stremme, W., Mellqvist, J., Strandberg, A., Ellingsen, K., and Gauss, M.: Trend analysis of greenhouse gases over Europe measured by a network of ground-based remote FTIR instruments, Atmos. Chem. Phys., 8, 6719–6727, doi:10.5194/acp-8-6719-2008, 2008. 31303, 31306, 31330, 31333

Guenther, A., Karl, T., Harley, P., Wiedinmyer, C., Palmer, P. I., and Geron, C.: Estimates of global terrestrial isoprene emissions using MEGAN (Model of Emissions of Gases and Aerosols from Nature), Atmos. Chem. Phys., 6, 3181–3210, doi:10.5194/acp-6-3181-2006, 2006. 31296

Guenther, A. B., Jiang, X., Heald, C. L., Sakulyanontvittaya, T., Duhl, T., Emmons, L. K., and Wang, X.: The Model of Emissions of Gases and Aerosols from Nature version 2.1 (MEGAN2.1): an extended and updated framework for modeling biogenic emissions, Geosci. Model Dev., 5, 1471–1492, doi:10.5194/gmd-5-1471-2012, 2012. 31296

Hak, C., Pundt, I., Trick, S., Kern, C., Platt, U., Dommen, J., Ordóñez, C., Prévôt, A. S. H., Junkermann, W., Astorga-Lloréns, C., Larsen, B. R., Mellqvist, J., Strandberg, A., Yu, Y., Galle, B., Kleffmann, J., Lörzer, J. C., Braathen, G. O., and Volkamer, R.: Intercomparison of four different in-situ techniques for ambient formaldehyde measurements in urban air, Atmos. Chem. Phys., 5, 2881–2900, doi:10.5194/acp-5-2881-2005, 2005. 31289, 31290

Heckel, A., Richter, A., Tarsu, T., Wittrock, F., Hak, C., Pundt, I., Junkermann, W., and Burrows, J. P.: MAX-DOAS measurements of formaldehyde in the Po-Valley, Atmos. Chem. Phys., 5, 909–918, doi:10.5194/acp-5-909-2005, 2005. 31290

ACPD
15, 31287–31333, 2015

Herndon, S. C., Jayne, J. T., Zahniser, M. S., Worsnop, D. R., Knighton, B., Alwine, E., Lamb, B. K., Zavala, M., Nelson, D. D., McManus, J. B., Shorter, J. H., Canagaratnam, M. R., Onasch, T. B., and Kolb, C. E.: Characterization of urban pollutant emission fluxes and ambient concentration distributions using a mobile laboratory with rapid response instrumentation, Faraday Discuss., 130, 327–339, doi:10.1039/B500411J, 2005. 31290

Houweling, S., Dentener, F., and Lelieveld, J.: The impact of nonmethane hydrocarbon compounds on tropospheric photochemistry, J. Geophys. Res.-Atmos., 103, 10673–10696, doi:10.1029/97JD03582, 1998. 31289

Inomata, S., Tanimoto, H., Kameyama, S., Tsunogai, U., Irie, H., Kanaya, Y., and Wang, Z.: Technical Note: Determination of formaldehyde mixing ratios in air with PTR-MS: laboratory experiments and field measurements, Atmos. Chem. Phys., 8, 273–284, doi:10.5194/acp-8-273-2008, 2008. 31290

Irie, H., Takashima, H., Kanaya, Y., Boersma, K. F., Gast, L., Wittrock, F., Brunner, D., Zhou, Y., and Van Roozendael, M.: Eight-component retrievals from ground-based MAX-DOAS observations, Atmos. Meas. Tech., 4, 1027–1044, doi:10.5194/amt-4-1027-2011, 2011. 31290

Jones, N. B., Riedel, K., Allan, W., Wood, S., Palmer, P. I., Chance, K., and Notholt, J.: Long-term tropospheric formaldehyde concentrations deduced from ground-based fourier transform solar infrared measurements, Atmos. Chem. Phys., 9, 7131–7142, doi:10.5194/acp-9-7131-2009, 2009. 31290

Junkermann, W.: On the distribution of formaldehyde in the western Po-Valley, Italy, during FORMAT 2002/2003, Atmos. Chem. Phys., 9, 9187–9196, doi:10.5194/acp-9-9187-2009, 2009. 31291

Kanakidou, M., Seinfeld, J. H., Pandis, S. N., Barnes, I., Dentener, F. J., Facchini, M. C., Van Dingenen, R., Ervens, B., Nenes, A., Nielsen, C. J., Swietlicki, E., Putaud, J. P., Balkanski, Y., Fuzzi, S., Horth, J., Moortgat, G. K., Winterhalter, R., Myhre, C. E. L., Tsigaridis, K., Vignati, E., Stephanou, E. G., and Wilson, J.: Organic aerosol and global climate modelling: a review, Atmos. Chem. Phys., 5, 1053–1123, doi:10.5194/acp-5-1053-2005, 2005. 31289

Kirschke, S., Bousquet, P., Ciais, P., Saunois, M., Canadell, J. G., Dlugokencky, E. J., Bergamaschi, P., Bergmann, D., Blake, D. R., Bruhwiler, L., Cameron-Smith, P., Castaldi, S., Chevallier, F., Feng, L., Fraser, A., Heimann, M., Hodson, E. L., Houweling, S., Josse, B., Fraser, P. J., Krummel, P. B., Lamarque, J.-F., Langenfelds, R. L., Le Quéré, C., Naik, V., O'Doherty, S., Palmer, P. I., Pison, I., Plummer, D., Poulter, B., Prinn, R. G., Rigby, M., Ringeval, B., Santini, M., Schmidt, M., Shindell, D. T., Simpson, I. J., Spahni, R., Steele, L. P.,

ACPD
15, 31287–31333, 2015

Strode, S. A., Sudo, K., Szopa, S., van der Werf, G. R., Voulgarakis, A., van Weele, M., Weiss, R. F., Williams, J. E., and Zeng, G.: Three decades of global methane sources and sinks, Nat. Geosci., 6, 813–823, doi:10.1038/ngeo1955, 2013. 31308

Lee, M., Heikes, B. G., Jacob, D. J., Sachse, G., and Anderson, B.: Hydrogen peroxide, organic hydroperoxide, and formaldehyde as primary pollutants from biomass burning, J. Geophys. Res., 102, 1301–1309, doi:10.1029/96JD01709, 1997. 31290

Legreid, G., Folini, D., Staehelin, J., Balzani Lööv, J., Steinbacher, M., and Reimann, S.: Measurements of organic trace gases including oxygenated volatile organic compounds at the high alpine site Jungfraujoch (Switzerland): seasonal variation and source allocations, J. Geophys. Res., 113, D05307, doi:10.1029/2007JD008653, 2008. 31304

Logan, J. A., Prather, M. J., Wofsy, S. C., and McElroy, M. B.: Tropospheric chemistry: a global perspective, J. Geophys. Res., 86, 7210–7254, doi:10.1029/JC086iC08p07210, 1981. 31289

Luecken, D. J., Hutzell, W. T., Strum, M. L., and Pouliot, G. A.: Regional sources of atmospheric formaldehyde and acetaldehyde, and implications for atmospheric modeling, Atmos. Environ., 47, 477–490, doi:10.1016/j.atmosenv.2011.10.005, 2012. 31289

MacDonald, S. M., Oetjen, H., Mahajan, A. S., Whalley, L. K., Edwards, P. M., Heard, D. E., Jones, C. E., and Plane, J. M. C.: DOAS measurements of formaldehyde and glyoxal above a south-east Asian tropical rainforest, Atmos. Chem. Phys., 12, 5949–5962, doi:10.5194/acp-12-5949-2012, 2012. 31291

Mahieu, E., Zander, R., Delbouille, L., Demoulin, P., Roland, G., and Servais, C.: Observed trends in total vertical column abundances of atmospheric gases from IR solar spectra recorded at the Jungfraujoch, J. Atmos. Chem., 28, 227–243, doi:10.1023/A:1005854926740, 1997. 31290

Mao, J., Jacob, D. J., Evans, M. J., Olson, J. R., Ren, X., Brune, W. H., Clair, J. M. St., Crounse, J. D., Spencer, K. M., Beaver, M. R., Wennberg, P. O., Cubison, M. J., Jimenez, J. L., Fried, A., Weibring, P., Walega, J. G., Hall, S. R., Weinheimer, A. J., Cohen, R. C., Chen, G., Crawford, J. H., McNaughton, C., Clarke, A. D., Jaeglé, L., Fisher, J. A., Yantosca, R. M., Le Sager, P., and Carouge, C.: Chemistry of hydrogen oxide radicals (HO_x) in the Arctic troposphere in spring, Atmos. Chem. Phys., 10, 5823–5838, doi:10.5194/acp-10-5823-2010, 2010. 31295

Mao, J., Paulot, F., Jacob, D. J., Cohen, R. C., Crounse, J. D., Wennberg, P. O., Keller, C. A., Hudman, R. C., Barkley, M. P., and Horowitz, L. W.: Ozone and organic nitrates over the

ACPD
15, 31287–31333, 2015

eastern United States: Sensitivity to isoprene chemistry, J. Geophys. Res.-Atmos., 118, 11, 256–268, doi:10.1002/jgrd.50817, 2013. 31296

Marais, E. A., Jacob, D. J., Kurosu, T. P., Chance, K., Murphy, J. G., Reeves, C., Mills, G., Casadio, S., Millet, D. B., Barkley, M. P., Paulot, F., and Mao, J.: Isoprene emissions in Africa inferred from OMI observations of formaldehyde columns, Atmos. Chem. Phys., 12, 6219–6235, doi:10.5194/acp-12-6219-2012, 2012. 31290, 31295

Marais, E. A., Jacob, D. J., Guenther, A., Chance, K., Kurosu, T. P., Murphy, J. G., Reeves, C. E., and Pye, H. O. T.: Improved model of isoprene emissions in Africa using Ozone Monitoring Instrument (OMI) satellite observations of formaldehyde: implications for oxidants and particulate matter, Atmos. Chem. Phys., 14, 7693–7703, doi:10.5194/acp-14-7693-2014, 2014. 31290

Marquardt, D. W.: An Algorithm for Least-Squares Estimation of Nonlinear Parameters, J. Soc. Indust. Appl. Math., 11, 431–441, doi:10.1137/0111030, 1963. 31300

Millet, D. B., Jacob, D. J., Boersma, K. F., Fu, T. M., Kurosu, T. P., Chance, K., Heald, C. L., and Guenther, A.: Spatial distribution of isoprene emissions from North America derived from formaldehyde column measurements by the OMI satellite sensor, J. Geophys. Res., 113, D02307, doi:10.1029/2007JD008950, 2008. 31290

Montzka, S. A., Krol, M., Dlugokencky, E., Hall, B., Jockel, P., and Lelieveld, J.: Small interannual variability of global atmospheric hydroxyl, Science, 331, 67–69, doi:10.1126/science.1197640, 2011. 31307

Nisbet, E. G., Dlugokencky, E. J., and Bousquet, P.: Atmospheric science. Methane on the rise-again, Science, 343, 493–495, doi:10.1126/science.1247828, 2014. 31307, 31308

Notholt, J., Toon, G., Stordal, F., Solberg, S., Schmidbauer, N., Becker, E., Meier, A., and Sen, B.: Seasonal variations of atmospheric trace gases in the high Arctic at 79 °N, J. Geophys. Res., 102, 12855–12861, doi:10.1029/97JD00337, 1997. 31290

Palmer, P. I., Jacob, D. J., Fiore, A. M., Martin, R. V., Chance, K., and Kurosu, T. P.: Mapping isoprene emissions over North America using formaldehyde column observations from space, J. Geophys. Res., 108, 4180, doi:10.1029/2002JD002153, 2003. 31290

Palmer, P. I., Abbot, D. S., Fu, T.-M., Jacob, D. J., Chance, K., Kurosu, T. P., Guenther, A., Wiedinmyer, C., Stanton, J. C., Pilling, M. J., Pressley, S. N., Lamb, B., and Sumner, A. L.: Quantifying the seasonal and interannual variability of North American isoprene emissions using satellite observations of the formaldehyde column, J. Geophys. Res., 111, D12315, doi:10.1029/2005JD006689, 2006. 31290

ACPD
15, 31287–31333, 2015

Park, R. J., Jacob, D. J., Field, B. D., Yantosca, R. M., and Chin, M.: Natural and transboundary pollution influences on sulfate-nitrate-ammonium aerosols in the United States: implications for policy, J. Geophys. Res., 109, D15204, doi:10.1029/2003JD004473, 2004. 31295

Paton-Walsh, C., Deutscher, N. M., Griffith, D. W. T., Forgan, B. W., Wilson, S. R., Jones, N. B., and Edwards, D. P.: Trace gas emissions from savanna fires in Northern Australia, J. Geophys. Res., 115, D16314, doi:10.1029/2009JD013309, 2010. 31290

Paulot, F., Crounse, J. D., Kjaergaard, H. G., Kroll, J. H., Seinfeld, J. H., and Wennberg, P. O.: Isoprene photooxidation: new insights into the production of acids and organic nitrates, Atmos. Chem. Phys., 9, 1479–1501, doi:10.5194/acp-9-1479-2009, 2009a. 31295, 31303

Paulot, F., Crounse, J. D., Kjaergaard, H. G., Kürten, A., St Clair, J. M., Seinfeld, J. H., and Wennberg, P. O.: Unexpected epoxide formation in the gas-phase photo-oxidation of isoprene, Science, 325, 730–733, doi:10.1126/science.1172910, 2009b. 31295, 31303

Peters, E., Wittrock, F., Großmann, K., Frieß, U., Richter, A., and Burrows, J. P.: Formaldehyde and nitrogen dioxide over the remote western Pacific Ocean: SCIAMACHY and GOME-2 validation using ship-based MAX-DOAS observations, Atmos. Chem. Phys., 12, 11179–11197, doi:10.5194/acp-12-11179-2012, 2012. 31298

Pfister, G. G., Emmons, L. K., Hess, P. G., Lamarque, J.-F., Orlando, J. J., Walters, S., Guenther, A., Palmer, P. I., and Lawrence, P. J.: Contribution of isoprene to chemical budgets: A model tracer study with the NCAR CTM MOZART-4, J. Geophys. Res., 113, D05308, doi:10.1029/2007JD008948, 2008. 31290

Pikelnaya, O., Hurlock, S. C., Trick, S., and Stutz, J.: Intercomparison of multiaxis and long-path optical absorption spectroscopy measurements in the marine boundary layer, J. Geophys. Res., 112, D10S01, doi:10.1029/2006JD007727, 2007. 31290

Pinardi, G., Van Roozendael, M., Abuhassan, N., Adams, C., Cede, A., Clémer, K., Fayt, C., Frieß, U., Gil, M., Herman, J., Hermans, C., Hendrick, F., Irie, H., Merlaud, A., Navarro Comas, M., Peters, E., Piters, A. J. M., Puentedura, O., Richter, A., Schönhardt, A., Shaiganfar, R., Spinei, E., Strong, K., Takashima, H., Vrekoussis, M., Wagner, T., Wittrock, F., and Yilmaz, S.: MAX-DOAS formaldehyde slant column measurements during CINDI: intercomparison and analysis improvement, Atmos. Meas. Tech., 6, 167–185, doi:10.5194/amt-6-167-2013, 2013. 31290

Possanzini, M., Di Palo, V., and Ceccinato, A.: Sources and photodecomposition of formaldehyde and acetaldehyde in Rome ambient air, Atmos. Environ., 36, 3195–3201, doi:10.1016/S1352-2310(02)00192-9, 2002. 31289

ACPD
15, 31287–31333, 2015

Rinsland, C. P., Jones, N. B., Connor, B. J., Logan, J. A., Pougatchev, N. S., Goldman, A., Murcray, F. J., Stephen, T. M., Pine, A. S., Zander, R., Mahieu, E., and Demoulin, P.: Northern and Southern Hemisphere ground-based infrared spectroscopic measurements of tropospheric carbon monoxide and ethane, J. Geophys. Res., 103, 28197–28217, doi:10.1029/98JD02515, 1998. 31325

Rodgers, C. D.: Inverse Methods for Atmospheric Sounding: Theory and Practice, Series on Atmospheric, Oceanic and Planetary Physics, Vol. 2, World Scientific Publishing Co., Singapore, 2000. 31325

Rodgers, C. D. and Connor, B. J.: Intercomparison of remote sounding instruments, J. Geophys. Res., 108, 4116–4129, doi:10.1029/2002JD002299, 2003. 31297

Rothman, L. S., Gordon, I. E., Barbe, A., Benner, D. C., Bernath, P. F., Birk, M., Boudon, V., Brown, L. R., Campargue, A., Champion, J.-P., Chance, K., Coudert, L. H., Danaj, V., Devi, V. M., Fally, S., Flaud, J.-M., Gamache, R. R., Goldmanm, A., Jacquemart, D., Kleiner, I., Lacome, N., Lafferty, W. J., Mandin, J.-Y., Massie, S. T., Mikhailenko, S. N., Miller, C. E., Moazzen-Ahmadi, N., Naumenko, O. V., Nikitin, A. V., Orphal, J., Perevalov, V. I., Perrin, A., Predoi-Cross, A., Rinsland, C. P., Rotger, M., Simeckova, M., Smith, M. A. H., Sung, K., Tashkun, S. A., Tennyson, J., Toth, R. A., Vandaele, A. C., and Vander Auwera, J.: The Hitran 2008 molecular spectroscopic database, J. Quant. Spectrosc. Ra., 110, 533–572, doi:10.1016/j.jqsrt.2009.02.013, 2009. 31325

Simpson, D., Michael Gauss, S. T., and Valdebenito, A.: Model Updates Transboundary Acidification, Eutrophication and Ground Level Ozone in Europe EMEP Status Report 1/2010, The Norwegian Meteorological Institute, Oslo, Norway, 2010. 31296

Simpson, I. J., Sulbaek Andersen, M. P., Meinardi, S., Bruhwiler, L., Blake, N. J., Helmig, D., Rowland, F. S., and Blake, D. R.: Long-term decline of global atmospheric ethane concentrations and implications for methane, Nature, 488, 490–494, doi:10.1038/nature11342, 2012. 31307

Staffelbach, T., Neftel, A., Stauffer, B., and Jacob, D. J.: A record of the atmospheric methane sink from formaldehyde in polar ice cores, Nature, 349, 603–605, doi:10.1038/349603a0, 1991. 31289

Starokozhev, E., Fries, E., Cycura, A., and Püttmann, W.: Distribution of VOCs between air and snow at the Jungfraujoch high alpine research station, Switzerland, during CLACE 5 (winter 2006), Atmos. Chem. Phys., 9, 3197–3207, doi:10.5194/acp-9-3197-2009, 2009. 31304

ACPD
15, 31287–31333, 2015

Stavrakou, T., Müller, J.-F., De Smedt, I., Van Roozendael, M., van der Werf, G. R., Giglio, L., and Guenther, A.: Global emissions of non-methane hydrocarbons deduced from SCIAMACHY formaldehyde columns through 2003–2006, Atmos. Chem. Phys., 9, 3663–3679, doi:10.5194/acp-9-3663-2009, 2009a. 31290

Stavrakou, T., Müller, J.-F., De Smedt, I., Van Roozendael, M., van der Werf, G. R., Giglio, L., and Guenther, A.: Evaluating the performance of pyrogenic and biogenic emission inventories against one decade of space-based formaldehyde columns, Atmos. Chem. Phys., 9, 1037–1060, doi:10.5194/acp-9-1037-2009, 2009b. 31290

Stavrakou, T., Müller, J.-F., Boersma, K. F., van der A, R. J., Kurokawa, J., Ohara, T., and Zhang, Q.: Key chemical NO_x sink uncertainties and how they influence top-down emissions of nitrogen oxides, Atmos. Chem. Phys., 13, 9057–9082, doi:10.5194/acp-13-9057-2013, 2013. 31292

Stavrakou, T., Müller, J.-F., Bauwens, M., De Smedt, I., Van Roozendael, M., De Mazière, M., Vigouroux, C., Hendrick, F., George, M., Clerbaux, C., Coheur, P.-F., and Guenther, A.: How consistent are top-down hydrocarbon emissions based on formaldehyde observations from GOME-2 and OMI?, Atmos. Chem. Phys. Discuss., 15, 12007–12067, doi:10.5194/acpd-15-12007-2015, 2015. 31290, 31291, 31298, 31302

Stickler, A., Fischer, H., Williams, J., de Reus, M., Sander, R., Lawrence, M. G., Crowley, J. N., and Lelieveld, J.: Influence of summertime deep convection on formaldehyde in the middle and upper troposphere over Europe, J. Geophys. Res., 111, D14308, doi:10.1029/2005JD007001, 2006. 31311

van der Werf, G. R., Randerson, J. T., Giglio, L., Collatz, G. J., Mu, M., Kasibhatla, P. S., Morton, D. C., DeFries, R. S., Jin, Y., and van Leeuwen, T. T.: Global fire emissions and the contribution of deforestation, savanna, forest, agricultural, and peat fires (1997–2009), Atmos. Chem. Phys., 10, 11707–11735, doi:10.5194/acp-10-11707-2010, 2010. 31296

van Donkelaar, A., Martin, R. V., Leaitch, W. R., Macdonald, A. M., Walker, T. W., Streets, D. G., Zhang, Q., Dunlea, E. J., Jimenez, J. L., Dibb, J. E., Huey, L. G., Weber, R., and Andreae, M. O.: Analysis of aircraft and satellite measurements from the Intercontinental Chemical Transport Experiment (INTEX-B) to quantify long-range transport of East Asian sulfur to Canada, Atmos. Chem. Phys., 8, 2999–3014, doi:10.5194/acp-8-2999-2008, 2008. 31296

Van het Bolscher, M., Pereira, J., Spessa, A., Dalsoren, S., van Nojie, T., and Szopa, S.: REanalysis of the TROpospheric Chemical Composition Over the Past 40 years, Hamburg, Germany, Max Plank Institute for Meteorology, 2008. 31296

ACPD
15, 31287–31333, 2015

Viatte, C., Strong, K., Walker, K. A., and Drummond, J. R.: Five years of CO, HCN, C_2H_6, C_2H_2, CH_3OH, HCOOH and H_2CO total columns measured in the Canadian high Arctic, Atmos. Meas. Tech., 7, 1547–1570, doi:10.5194/amt-7-1547-2014, 2014. 31290

Vigouroux, C., Hendrick, F., Stavrakou, T., Dils, B., De Smedt, I., Hermans, C., Merlaud, A., Scolas, F., Senten, C., Vanhaelewyn, G., Fally, S., Carleer, M., Metzger, J.-M., Müller, J.-F., Van Roozendael, M., and De Mazière, M.: Ground-based FTIR and MAX-DOAS observations of formaldehyde at Réunion Island and comparisons with satellite and model data, Atmos. Chem. Phys., 9, 9523–9544, doi:10.5194/acp-9-9523-2009, 2009. 31290

Wagner, T., Beirle, S., Brauers, T., Deutschmann, T., Frieß, U., Hak, C., Halla, J. D., Heue, K. P., Junkermann, W., Li, X., Platt, U., and Pundt-Gruber, I.: Inversion of tropospheric profiles of aerosol extinction and HCHO and NO_2 mixing ratios from MAX-DOAS observations in Milano during the summer of 2003 and comparison with independent data sets, Atmos. Meas. Tech., 4, 2685–2715, doi:10.5194/amt-4-2685-2011, 2011. 31290

Wert, B. P., Trainer, M., Fried, A., Ryerson, T. B., Henry, B., Potter, W., Angevine, W. M., Atlas, E., Donnelly, S. G., Fehsenfeld, F. C., Frost, G. J., Goldan, P. D., Hansel, A., Holloway, J. S., Hubler, G., Kuster, W. C., Nicks Jr., D. K., Neuman, J. A., Parrish, D. D., Schauffler, S., Stutz, J., Sueper, D. T., Wiedinmyer, C., and Wisthaler, A.: Signatures of terminal alkene oxidation in airborne formaldehyde measurements during TexAQS 2000, J. Geophys. Res., 108, 4104, doi:10.1029/2002JD002502, 2003. 31290

Wittrock, F., Richter, A., Oetjen, H., Burrows, J. P., Kanakidou, M., Myriokefalitakis, S., Volkamer, R., Beirle, S., Platt, U., and Wagner, T.: Simultaneous global observations of glyoxal and formaldehyde from space, Geophys. Res. Lett., 33, L16804, doi:10.1029/2006GL026310, 2006. 31290

Xiao, Y., Logan, J. A., Jacob, D. J., Hudman, R. C., Yantosca, R., and Blake, D. R.: Global budget of ethane and regional constraints on U. S. sources, J. Geophys. Res., 113, D21306, doi:10.1029/2007JD009415, 2008. 31296

Zander, R., Mahieu, E., Demoulin, P., Duchatelet, P., Roland, G., Servais, C., Mazière, M. D., Reimann, S., and Rinsland, C. P.: Our changing atmosphere: evidence based on long-term infrared solar observations at the Jungfraujoch since 1950, Sci. Total Environ., 391, 184–195, doi:10.1016/j.scitotenv.2007.10.018, 2008. 31294, 31307

Zander, R., Duchatelet, P., Mahieu, E., Demoulin, P., Roland, G., Servais, C., Auwera, J. V., Perrin, A., Rinsland, C. P., and Crutzen, P. J.: Formic acid above the Jungfraujoch during

ACPD
15, 31287–31333, 2015

1985–2007: observed variability, seasonality, but no long-term background evolution, Atmos. Chem. Phys., 10, 10047–10065, doi:10.5194/acp-10-10047-2010, 2010. 31298

ACPD
15, 31287–31333, 2015

Table 1. Summary of the retrieval strategy for HCHO applied in this study above Jungfraujoch. A thorough description is given by Franco et al. (2015b).

Retrieval code	SFIT-2 v3.91 algorithm (Rinsland et al., 1998)
A priori profile	From WACCM v6 simulations
Regularization	Optimal estimation method (Rodgers, 2000)
Covariance profile	From WACCM v6 simulations (multiplied by 1.5)
Spectroscopic database	HITRAN 2008 (Rothman et al., 2009)
Microwindows (and interfering species)	2763.425–2763.600 cm^{-1} (HDO, CH_4, O_3, N_2O, CO_2)
	2765.725–2765.975 cm^{-1} (HDO, CH_4, O_3, N_2O, CO_2)
	2778.200–2778.590 cm^{-1} (HDO, CH_4, O_3, N_2O, CO_2)
	2855.650–2856.400 cm^{-1} (HDO, CH_4, O_3, N_2O, H_2O)

ACPD
15, 31287–31333, 2015

Table 2. Trends of daily-mean 9 a.m.-scaled HCHO total columns derived from the ground-based FTIR observations at the ISSJ, calculated over the 1988–1995, 1996–2002, 2003–2015 and 1996–2015 time periods by the bootstrap resampling tool. These trends are calculated using either year-round or seasonal (over DJF, MAM, JJA and SON, respectively) observations. They are expressed in annual rate of change (% yr^{-1}) relative to the 1988.0, 1996.0 and 2003.0 columns modelled by the bootstrap tool. The trends significant at the 2σ confidence level are in boldface.

Observations	1988–1995	1996–2002	2003–2015	1996–2015
Year-round	**2.94 ± 2.02**	**−3.68 ± 1.00**	**0.81 ± 0.62**	**−0.61 ± 0.26**
Winter	**5.66 ± 5.04**	0.31 ± 2.39	−0.08 ± 1.16	**−1.05 ± 0.54**
Spring	**4.92 ± 2.86**	**−3.79 ± 2.05**	**1.90 ± 1.22**	−0.3 ± 0.52
Summer	**4.19 ± 3.29**	**−3.91 ± 1.63**	0.29 ± 1.16	**−0.65 ± 0.47**
Fall	1.24 ± 3.19	**−2.96 ± 2.53**	0.70 ± 1.26	−0.41 ± 0.61

ACPD
15, 31287–31333, 2015

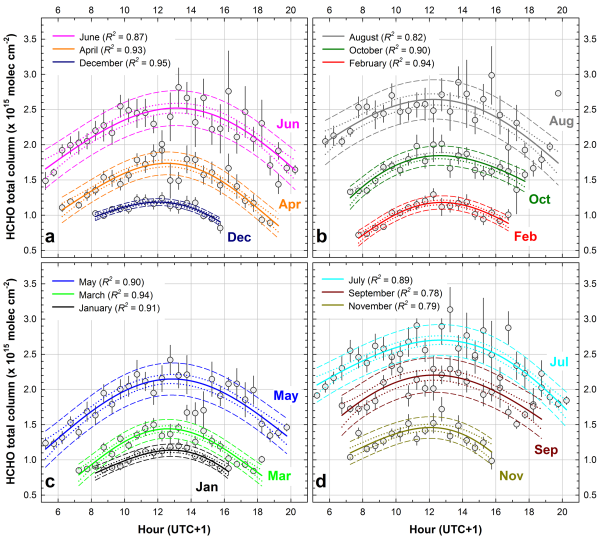

Figure 1. Intra-day variation of the HCHO abundance, represented by the 0.5 h-time step average (as grey circles) and corresponding standard error of the mean (as error bars) of the HCHO total columns (in molec cm^{-2}) derived from all individual observations made by the Bruker instrument between January 1995 and June 2015 at the ISSJ. It is expressed according to the hour of the day (UTC+1) and for each month of the year. No smoothing has been applied here. The solid color curves are the fits of the monthly running averages of the individual observations by the parametric model (Eq. 1), associated with the 95 % confidence and prediction intervals delimited by the dotted and dashed color curves, respectively. The running average used here corresponds to a 0.5 h time step and a 1.5 h-wide integration length. The coefficient of determination (R^2) of the model fit is provided for each month in legend. All the monthly fits by the parametric model are displayed on the same graph in Fig. 3a, Sect. 4.1. A global view of the observed intra-day cycles is available as Fig. S1 in the Supplement.

ACPD
15, 31287–31333, 2015

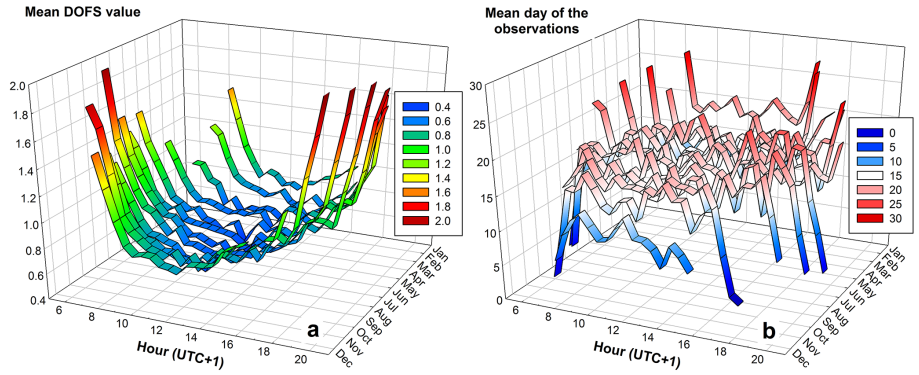

Figure 2. Average of the mean DOFS values and the mean observational day of the month (**a** and **b**, respectively) of all individual observations made by the Bruker instrument between January 1995 and June 2015 at the ISSJ, according to the hour of the day and for each month of the year. The average has been calculated with a time step and an integration length of 0.5 h (no smoothing has been applied here).

ACPD
15, 31287–31333, 2015

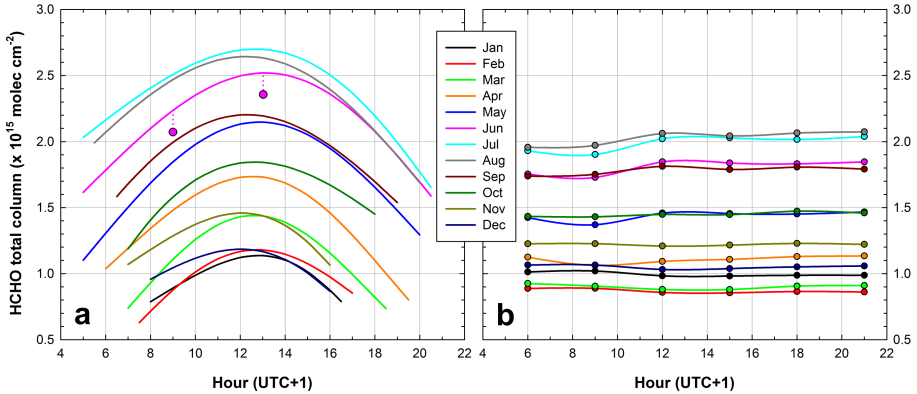

Figure 3. Monthly diurnal cycles of HCHO total columns above Jungfraujoch adjusted by the parametric model (Eq. 1) to the 1995–2015 BRUKER FTIR observations **(a)** and simulated by the standard run of GEOS-Chem over the July 2005–May 2013 time period **(b)**. The red circles in frame **(a)** illustrates an example of HCHO column derived from an individual observation made in June at 13.025 a.m. and scaled to 9 a.m. using the parametric model of HCHO intra-day variation (see explanation in Sect. 3.2).

ACPD
15, 31287–31333, 2015

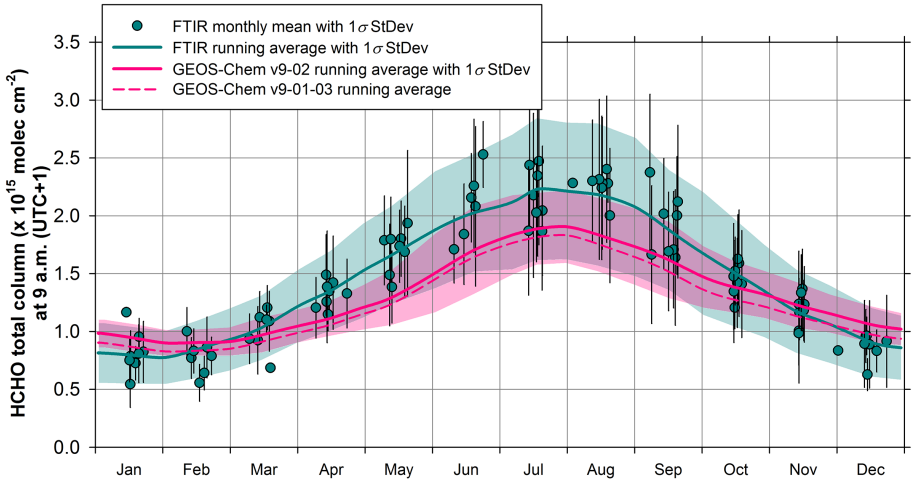

Figure 4. Monthly-averaged total columns of HCHO and associated 1σ standard deviation bars displayed on a 1 year time base, from the individual 9 a.m. (UTC + 1)-scaled FTIR measurements performed above the ISSJ between July 2005 and May 2013. Note that the daily observation values with relative anomalies to the curve fit calculated by Gardiner et al. (2008, see Sect. 5.2), higher than the 95th percentile value of all relative anomalies of the data set, have been excluded from the present data set. The green curve and shaded area show on a 1 year time base the running mean fit to the daily-averaged columns (with a 2-month wide integration time and a 15 day time step) and the associated 1σ standard deviation, respectively. The solid red line and shaded area represent corresponding information, but deduced from the smoothed outputs of the GEOS-Chem v9-02 standard run. The dashed red line corresponds to the same 1 year time base running mean, but obtained from the smoothed outputs of the GEOS-Chem v9-01-03 standard run. Note that the 1σ standard deviations around the running mean are calculated on the basis of the daily-averaged columns and hence include inter-annual fluctuations as well as variability of the monthly mean.

ACPD
15, 31287–31333, 2015

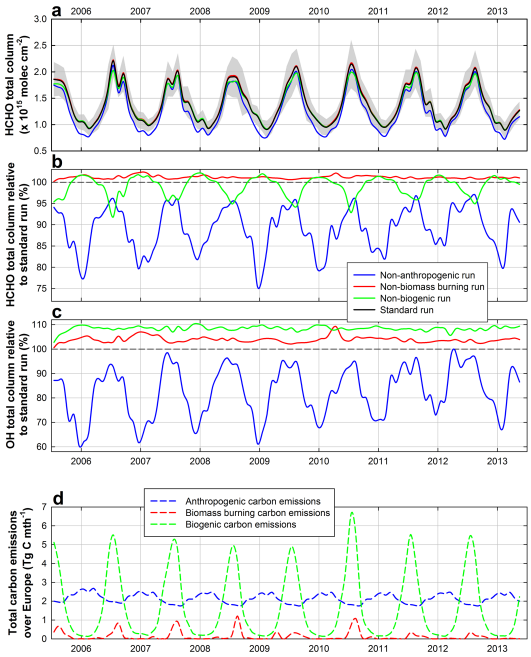

Figure 5. (a) Monthly mean of the daily-averaged HCHO total column (in molec cm^{-2}) above Jungfraujoch simulated by GEOS-Chem v9-02 over the July 2005–May 2013 time period, according to the standard and sensitivity (i.e. non-anthropogenic, non-biomass burning and non-biogenic) runs. In the sensitivity simulations, the anthropogenic, biomass burning and biogenic emissions of NMVOCs and NO have been shut off, while the CH_4 concentrations are still derived from NOAA measurements, as for the standard simulation. The grey shaded area corresponds to the 1σ standard deviation associated with the standard run. **(b)** HCHO total column from the sensitivity runs, as relative to the HCHO amount simulated by the standard run (in % of this latter). **(c)** The same as **(b)**, but for OH. **(d)** Monthly total carbon emissions (in Tg C month^{-1}) by category, integrated over Europe (between 38–86° N and −15–55° E).

ACPD
15, 31287–31333, 2015

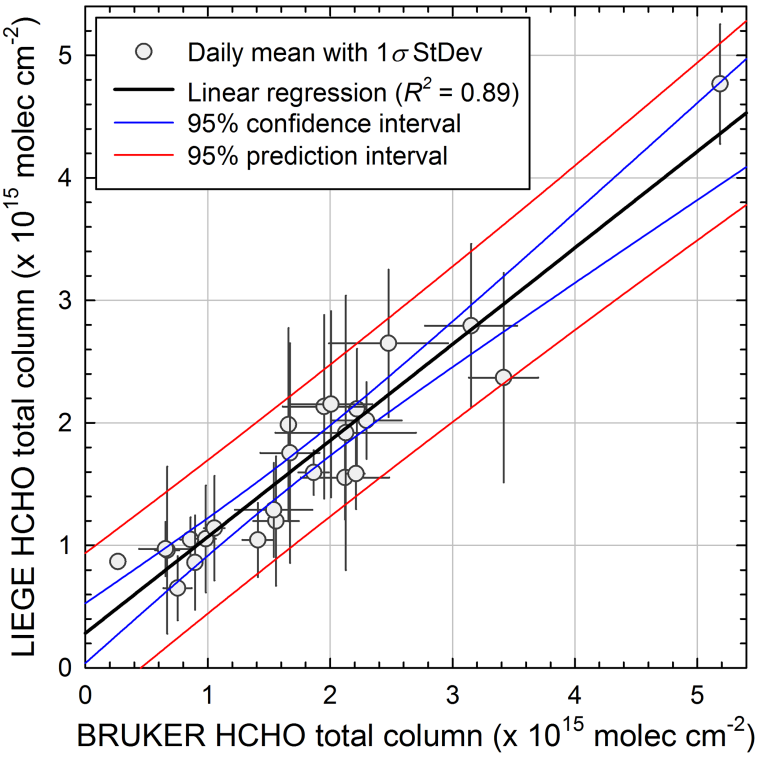

Figure 6. Scatter plot of the daily average (and the associated 1σ standard deviation as error bars) HCHO column measurements derived from FTIR observations made by the LIEGE and BRUKER instruments at the ISSJ, over the 1995–1997 time period. These daily means are compared for days with coincident observations, after scaling to 9 a.m. (see text). The solid black line is the linear regression between both data sets (R^2 = 0.89), along with the 95 % confidence and prediction intervals delimited by the blue and red lines, respectively.

ACPD
15, 31287–31333, 2015

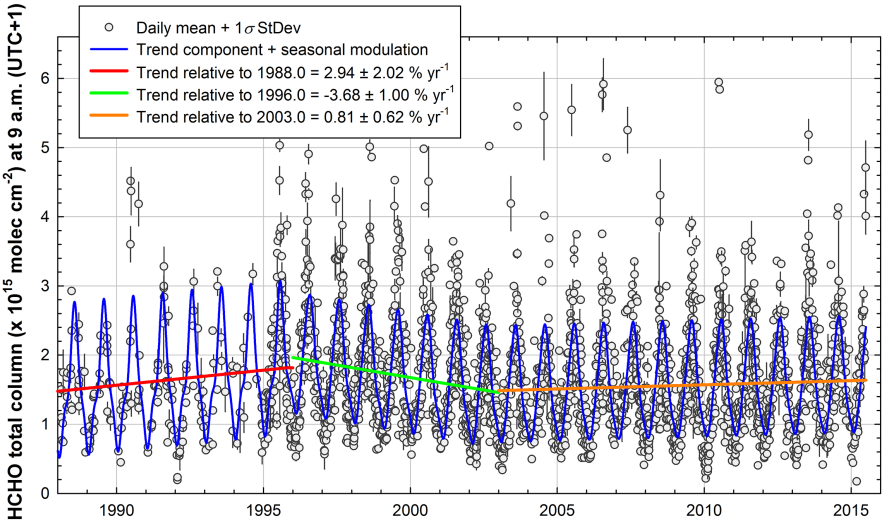

Figure 7. FTIR time series of daily mean HCHO total columns and associated 1σ standard deviation bars above Jungfraujoch, from January 1988 to June 2015. All individual measurements have been re-scaled to 9 a.m. (see text) and then averaged over the days. The blue curves correspond to the functions fitted to all daily means (including trend component and seasonal modulation) by the bootstrap method of Gardiner et al. (2008), over the 1988–1995, 1996–2002 and 2003–2015/06 time periods, inclusive.

ACPD
15, 31287–31333, 2015